Numerical study of InAs/GaAs quantum dot solar cells

ScuDo

Scuola di Dottorato ~ Doctoral School

WHAT YOU ARE, TAKES YOU FAR

Doctoral Dissertation

Doctoral Program in Electronics Engineering ($30^{th}$cycle)

# Numerical Study of InAs/GaAs Quantum-Dot Solar Cells

By


**Arastoo Khalili**

******


**Supervisor(s):**

Prof. Federica Cappelluti , Supervisor

Prof. Mariangela Gioannini , Co-Supervisor

**Doctoral Examination Committee:**

Prof. Stefano Sanguinetti, Referee, Universita' degli Studi di Milano-Bicocca

Prof. Matthias Auf der Maur, Referee, Universita' degli Studi di Roma "Tor Vergata"

Prof. Urs Aeberhard, IEK-5 Photovoltaik, Forschungszentrum Jülich

Prof. Michele Goano, Politecnico di Torino

Prof. Vittorianna Tasco, CNR NANOTEC-Institute of Nanotechnology


Politecnico di Torino

2018

*To my parents*

# Acknowledgements

I wish to thank the Department of Electronics and Telecommunications (DET), in Politecnico di Torino for providing a comfortable atmosphere for my research.
I would like to express my special appreciation and thanks to my supervisors Prof. Federica Cappelluti for leading me throughout my PhD program. I also would like to express my sincere gratitude to my co-supervisor Prof. Mariangela Gioannini for her constant support, availability and constructive suggestions in my time of need.

Finally, a special thanks to my family. Words cannot express my gratitude towards them.

# Abstract

Solar energy conversion is a promising way to provide future energy demand since it is a clean energy. Unfortunately, the photovoltaic (PV) conversion of the solar energy is expensive, therefore, making attempts to increase the efficiency of PV is essential. A conventional single junction solar cell presents an efficiency limit that is determined by the Shockley-Queisser detailed balance principle (i.e. 40.7% under full sun concentration). The limit comes from the fact that only photons with energy close to the energy bandgap are efficiently converted. Below energy gap, photons are not absorbed since the cell is transparent to them and high energy photons only contribute part of their energy that is equal to the energy bandgap. Many concepts have been developed in order to increase the efficiency limit of solar cells. Among them the intermediate band solar cell (IBSC) has gained considerable attention. In principle, IBSCs have the potential to overcome Shockley-Queisser (SQ) limit of single junction solar cells by providing high current while preserving large voltage. The theoretical limit calculated for an ideal IBSC under full sun concentration is 63.1%.

One of the most promising ways to realize the IBSC is to incorporate a QD superlattice in the active region of p-i-n single junction solar cells. The nano-size QDs behave like 3D potential well for the carriers and create discrete energy levels within the forbidden bandgap that allows sub-bandgap photon absorption. Stranski-Krastanov (S-K) growth mode (also called 'layer-plus-island growth') is one of the most common methods to fabricate QDs. This method has been used in many experimental studies for InAs/GaAs heteroepitaxial system which has lattice mismatch of 7.2%. Although InAs/GaAs is not an optimal material system for the IBSC performance, its properties and parameters are well reported in literature compared to other material systems.

The drift-diffusion model is the most widely used mathematical approach to describe semiconductor devices. However, in case of quantum dot solar cells, the physics

governing the device performance is not sufficiently covered and up to now, modeling of QDSCs has been treated as IBSC modeling through detailed balance principle and semi-analytical or numerical drift diffusion approaches.
In this dissertation, QDSCs are investigated in detail by numerical simulation using a QD-aware physics-based model. The influence of selective doping in QDSCs is investigated considering different scenarios in terms of crystal quality. Regarding high-quality crystal, close to radiative limit, large open circuit voltage recovery is predicted in doped cells, due to the suppression of radiative recombination through QD ground state. In case of defective crystal, significant photovoltage recovery is also attained owing to the suppression of both non-radiative and QD ground state radiative recombination. The interplay between non-radiative and QD radiative recombination channels, and their interplay with respect to doping are analyzed in detail. Moreover, a numerical study on the influence of wetting layer states on the photovoltage loss of InAs/GaAs quantum dot solar cells is presented. Almost full open circuit voltage recovery is predicted by combining wetting layer reduction and selective doping.
After investigating the inherent limitations of InAs/GaAs QD solar cells regarding realization of the IBSC, a brief description of QDs with type-II staggered band alignment based on GaSb/GaAs material systems (whose interband and intraband dynamics are more promising in view of attaining the IB operating regime) is given and a preliminary study of the competition between thermal and optical escape processes is presented.

# Contents

# Chapter 1

# Introduction

Nano scale semiconductor devices have been investigated intensively over the last two decades because of their potential to be the next generation technology. Semiconductor quantum dots (QDs) exhibit many unique electrical and optical properties due to their 3D quantum confinement. Unlike bulk semiconductors, the 0D QDs have quantized energy levels and localized carrier states. The carriers may be captured into or escape from the confined states via scattering and the net effect is the relaxation of carriers into quasi-equilibrium distribution [1]. QDs have high tunability and sensitivity with respect to their size and morphology that allow for engineering their electrical and optical properties [2]. Until early 1990s, the study of QDs was mainly theoretical due to the lack of feasible fabrication process. Thanks to the significance advancement in epitaxial growth techniques [3–5], QDs attracted attention from the experimental prospect and are successfully fabricated in lasers, photodetectors and solar cells.

In QD lasers, the benefit of QDs comes from the ability to focus the injected carriers in a narrow energy range that induces larger dependence of the optical gain on the injection current while the transparency current is reduced [6]. In quantum dot infrared photodetectors (QDIP), the tunability of the detection wavelength range via QD parameter engineering [7] and higher radiation tolerance due to localization of carriers [8] gain interest. Moreover, the 3D confinement of carriers provides low dark current and higher operating temperature because of the weak thermionic emission of carriers from the QDs [9, 10].

Quantum dot solar cells (QDSC) have been studied in order to improve the conversion efficiency by extending the spectral photoresponse of the cell. The QD system

with discrete density of states, can potentially be used to form three quasi-Fermi levels as required by the intermediate band solar cell (IBSC) theory [11]. Although, the energy gaps of InAs/GaAs material system are far from the optimum ones requested by an ideal IBSC, most of the investigations were based on this material system due to their well-known growth process and parameters with respect to other systems. The schematic diagram in figure 1.1 represents the theoretical (detailed balance) efficiency of a single junction solar cell and the IBSC with ideal and InAs/GaAs like band gaps. The experimental records of single junction cell and InAs/GaAs QDSC are also reported in the figure.

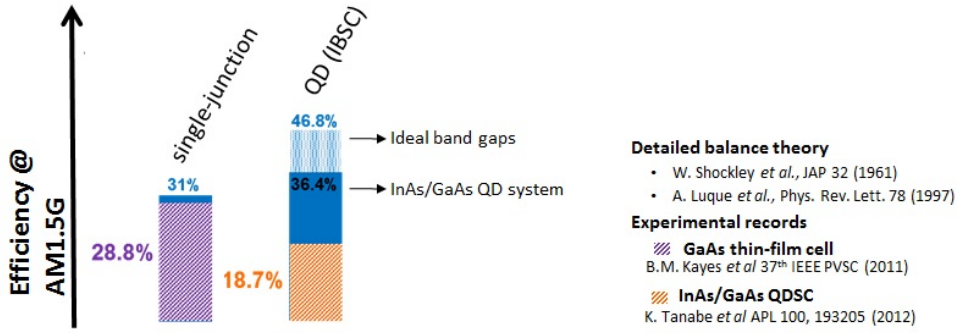


Fig. 1.1 Theoretical efficiency of bulk and QDSC along with the experimental records under one sun illumination.

Theoretically, the IBSC with InAs/GaAs bandgaps has the potential to overcome the GaAs bulk cell efficiency, however, there are few studies that report improved performance of QDSC with respect to their bulk counterparts [12, 13]. Most of the studies, even though demonstrated subband gap absorption, they could not reveal any improvement in terms of conversion efficiency. The frequent obstacle they encounter was that the weak short circuit current enhancement was accompanied by severe open circuit voltage drop.

The first chapter provides a background on the physics of IBSCs and an overview of the IBSCs models available in the literature. The second chapter is dedicated to the description of the model used in this thesis followed by a case study of one of the best QDSC reported in [14, 13] with the aim of studying the influence of geometrical and technological parameters on the open circuit voltage ($V_{oc}$). The third chapter is devoted to the investigation of charged QDSC since selective doping has been proposed to mitigate open circuit voltage reduction [15–17]. We will show how

doping can influence the cell performance at open circuit and how it can provide improvement in terms of efficiency with respect to the undoped QDSC. In chapter 4, the influence of the wetting layer (WL) on the electronic structure and open circuit voltage is investigated. Finally, in chapter 5 a brief description of type-II GaSb/GaAs material system, whose interband and intraband dynamics are more promising in view of attaining the IB operating regime, is given and a preliminary study of the competition between thermal and optical escape processes in GaSb/GaAs quantum dot solar cells is presented [18].

## 1.1 Intermediate band solar cell thermodynamics

The story of improving the efficiency of solar cells via multiple absorption transitions in a single material goes back to 1960 when sequential absorption via defect levels was proposed [19]. However, the topic attracted attention when Luque and Martí [11] have proposed intermediate band solar cell (IBSC) concept in 1997. The difference between the two approaches is that unlike impurity band, the IB should reduce non radiative transition rates that are likely to be promoted in impurity band solar cells [20, 21].

In principle, IBSCs have the potential to overcome Shockley-Queisser (SQ) limit of single junction solar cells. SQ limit determines the upper bound of the conversion efficiency of a single junction solar cell by assuming all the transitions to be radiative, full absorption of above bandgap photons, and infinite mobility of carriers so that they are all collected by the contacts. The maximum value of SQ conversion efficiency is reported to be around 31% for material with energy bandgap of around 1.3 eV [22]. The best realized single junction solar cell close to this limit is a thin-film GaAs solar cell with efficiency record of 28.8% [23]. The fundamental loss in SQ detailed balance limit comes from the trade-off between carrier thermalization and optical transparency which will be translated to the trade-off between current and voltage in terms of photovoltaic parameters [24]. The current voltage curves of three SQ solar cell are presented in figure 1.2, showing that the cell with small bandgap material promotes high current but low voltage while the cell with large bandgap yields low current but high voltage. In principle, the JV curve of an IBSC, as shown in the figure, has to provide high current while preserving large voltage. The schematic diagram of an IBSC is presented in figure 1.3. The current promotion with respect to

the SQ cell with the same optical bandgap is due to the additional sequential optical transitions via IB denoted by $G_{IC}$ and $G_{VI}$. Voltage preservation is due to the fact that the contacts are made to CB and VB. Note that thermal equilibrium does not exist between the bands because of their electrochemical potential difference. The marginally voltage reduction in IBSC is due to the transitions occurring through the IB denoted by $R_{IC}$ and $R_{VI}$.

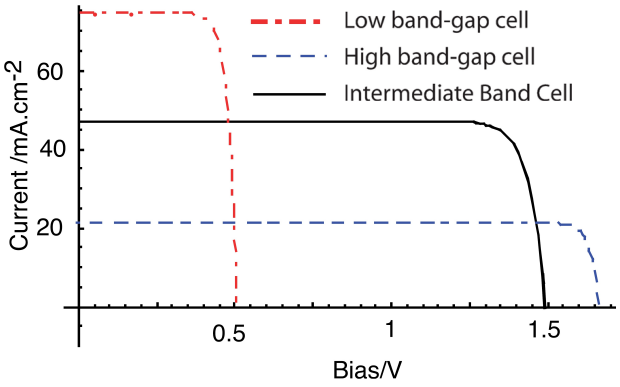


Fig. 1.2 Taken from [24]. Current-voltage curves of an IBSC and two SQ solar cells with absorption thresholds corresponding to the lowest and highest energy gaps in the IBSC.

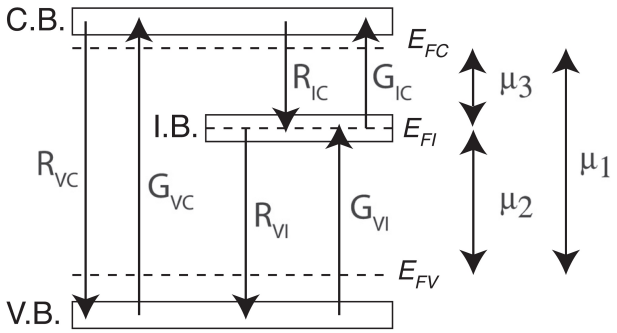


Fig. 1.3 IBSC schematic diagram and the theoretical transitions involved.

Figure 1.4 represents the efficiency of the IBSC with respect to the IB energy position $E_l$. The figure highlights the potential of the IBSC with respect to single junction solar cell in terms of conversion efficiency. The corresponding values of energy bandgap are also reported in the graph. The maximum theoretical efficiency of an IBSC having ideal bandgaps of $E_l = 0.71$ eV, $E_h = 1.24$ eV and $E_g = 1.96eV$

has been demonstrated to be 63.1% under full sun concentration [11].

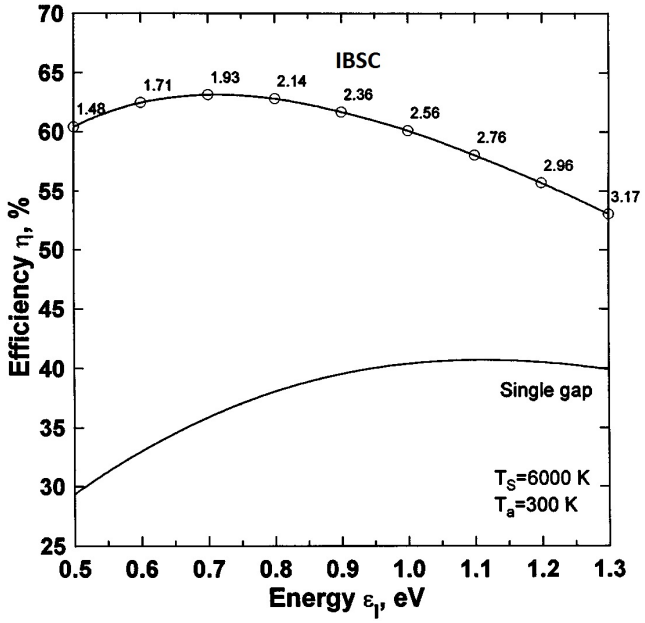


Fig. 1.4 Taken from [11]. Efficiency of the IBSC as a function of lowest gap $E_l$ under full sun concentration. The values above each node is the corresponding energy bandgap $E_g$ of the host material. The efficiency of a single gap solar cell is also shown.

## 1.2 Interband optical absorption

Following the formulation presented in [24], under illumination the net optical absorption rate $W_{\mathrm{VC}}$ is the difference between absorption $r_a(\hbar\omega)$ and emission rates $r_e(\hbar\omega)$ with units in $\mathrm{cm}^{-3}\mathrm{s}^{-1}$.

$$W_{\mathrm{VC}} = r_a(\hbar\omega) - r_e(\hbar\omega) \tag{1.1}$$

Where $\omega$ is the angular frequency, and $\hbar$ is the reduced Plank constant. Since optical transitions in semiconductor result in negligible change in k space and there is a unique correspondence between photon energy and location in k-space the absorption and emission rates can be written as follows.

$$r_a(\hbar\omega) = n_\gamma(\hbar\omega)\, M\left(\varepsilon', \hbar\omega\right) n_o\left(\varepsilon'\right) n_u\left(\varepsilon' + \hbar\omega\right) \tag{1.2}$$

$$r_e(\hbar\omega) = n_\gamma(\hbar\omega) M\left(\varepsilon^{'}, \hbar\omega\right) n_u\left(\varepsilon^{'}\right) n_o\left(\varepsilon^{'} + \hbar\omega\right) \tag{1.3}$$

Where $n_\gamma$ is the photon density, $\varepsilon^{'}$ is the energy state, and $n_o$ and $n_u$ are the occupied and unoccupied carriers population, respectively. $M$ is the interband momentum matrix in order to ensure the conservation of momentum. In fact, each element of the matrix $M$ represents a combination of states which is non-zero only for the transitions which preserve momentum. In above equations, $\varepsilon^{'} + \hbar\omega$ is the final energy state after the transition. Carrier population is a function of carrier density of states $g_{\mathrm{v}}$ and $g_{\mathrm{c}}$ and their Fermi-Dirac occupancy functions $f_{\mathrm{v}}(\varepsilon)$ and $f_{\mathrm{c}}(\varepsilon)$ respectively. Thus the net absorption can be rewritten as

$$W_{\mathrm{VC}} = n_\gamma(\hbar\omega) M\left(\varepsilon^{'}, \hbar\omega\right) g_{\mathrm{v}}\left(\varepsilon^{'}\right) g_{\mathrm{c}}\left(\varepsilon^{'} + \hbar\omega\right) \times \left(f_{\mathrm{v}}\left(\varepsilon^{'}\right) - f_{\mathrm{c}}\left(\varepsilon^{'} + \hbar\omega\right)\right) \tag{1.4}$$

Strong absorption requires the lower states to be full and the higher states to be empty. However, the IB has to support two sequential transition both in-to and out-of the same state. Since the two transitions are series conducted, the expression $f_v\left(\varepsilon^{'}\right) - f_c\left(\varepsilon^{'} + \hbar\omega\right)$ has to be carefully taken into account and the requirement for matching the two currents corresponding to these transitions is to design the IB to be half filled so that the corresponding currents obtained from the two in-to and out-of the IB processes match.

## 1.3 Photo filling

Poisson equation is used to determine the electrostatic potential of a solar cell in steady-state.

$$\nabla \cdot (\varepsilon \nabla \psi) = -\rho \tag{1.5}$$

Where, $\varepsilon$ is the dielectric constant and $\rho$ is the total charge density. In order to assess an accurate potential profile, one has to take IB charges into account since the IB introduce additional states within the forbidden gap that may become charged. To this aim, the process of capturing and escaping of charges from this level and their influence on the potential profile have to be considered.
In the drift-diffusion method, the continuity equations are solved to compute the

current.

$$\nabla \cdot J_e = qR \tag{1.6}$$

$$\nabla \cdot J_h = -qR \tag{1.7}$$

Where, $J_e$ and $J_h$ are the electron and hole current density (A $cm^{-2}$), $q$ is the elementary charge (C) and $R$ is the recombination rate ($cm^{-3}s^{-1}$). Doping also plays a significant role due to the modification of IB charges and extraction efficiency. To illustrate the influence of doping on the potential profile and cell performance the drift-diffusion simulation results from [25] is presented in figures 1.5,1.6 and 1.7. Figure 1.5 and 1.6 represent the IBSC potential profile at short circuit for undoped and doped cell, respectively. The potential profiles are reported in three conditions: (a) equilibrium, (b) one sun illumination and (c) 1000 suns concentration. The undoped cell in equilibrium has a profile similar to a p-i-n junction since the depletion region spreads over the IB region. The doped cell on the other hand behaves like p-$n^-$-n junction due to the increase of charges in the active region (IB region). Moreover, in both figures the change in potential profile is significant when the cell is illuminated which is a consequence of IB photogeneration. At high concentration the IB quasi-fermi level reaches the IB band edge ($E_\mathrm{I}$) showing that at high concentration the difference between $E_\mathrm{I}$ and $E_\mathrm{FI}$ does not depend on doping. The behavior of the solar cell performance parameters (short circuit current $J_{sc}$, open circuit voltage $V_{oc}$ and efficiency $\eta$) with respect to the sun concentration from [25] are shown in figure 1.7. In addition to the large enhancement of IBSC performance with respect to single junction cells, the study also confirms that at high concentration the performance parameters have no dependence on doping.

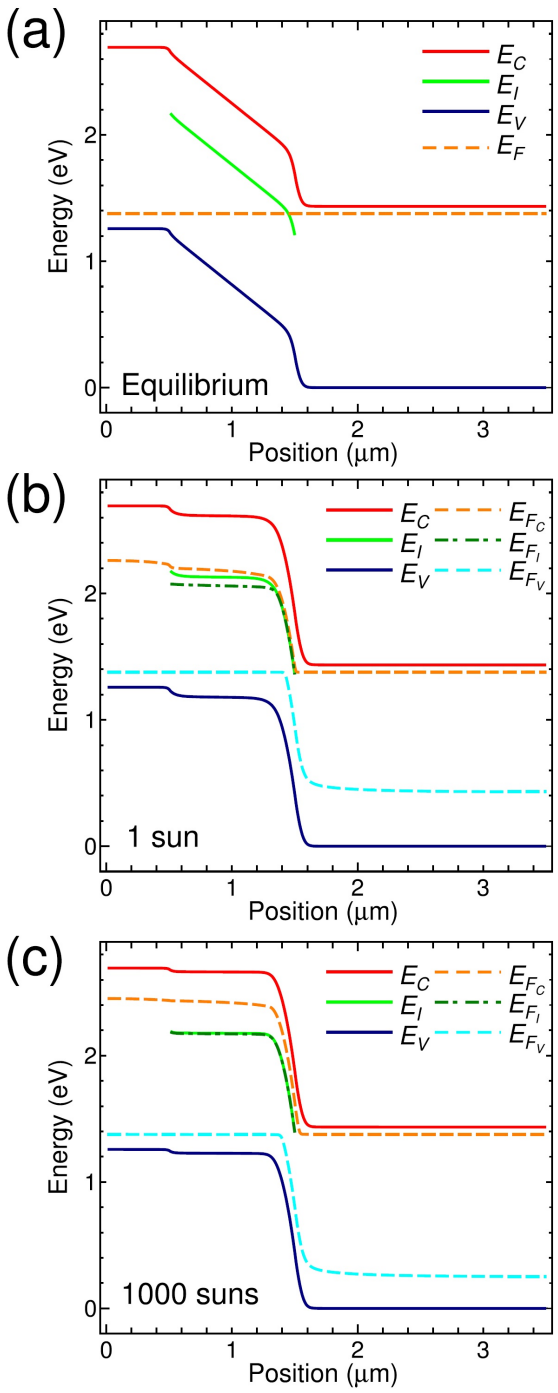


Fig. 1.5 Taken from [25]. Band profile of an IBSC in short-circuit condition along x-direction with undoped IB in three conditions: (a) in equilibrium, (b) under 1 sun illumination, and (c) under 1000 suns illumination. $E_C$ and $E_V$ represent the band edge of CB and VB, respectively, and $E_I$ is that of IB. $E_{FC}$ ; $E_{FI}$ ; and $E_{FV}$ are the quasi-Fermi levels of electrons in CB, IB and of holes in VB, respectively.

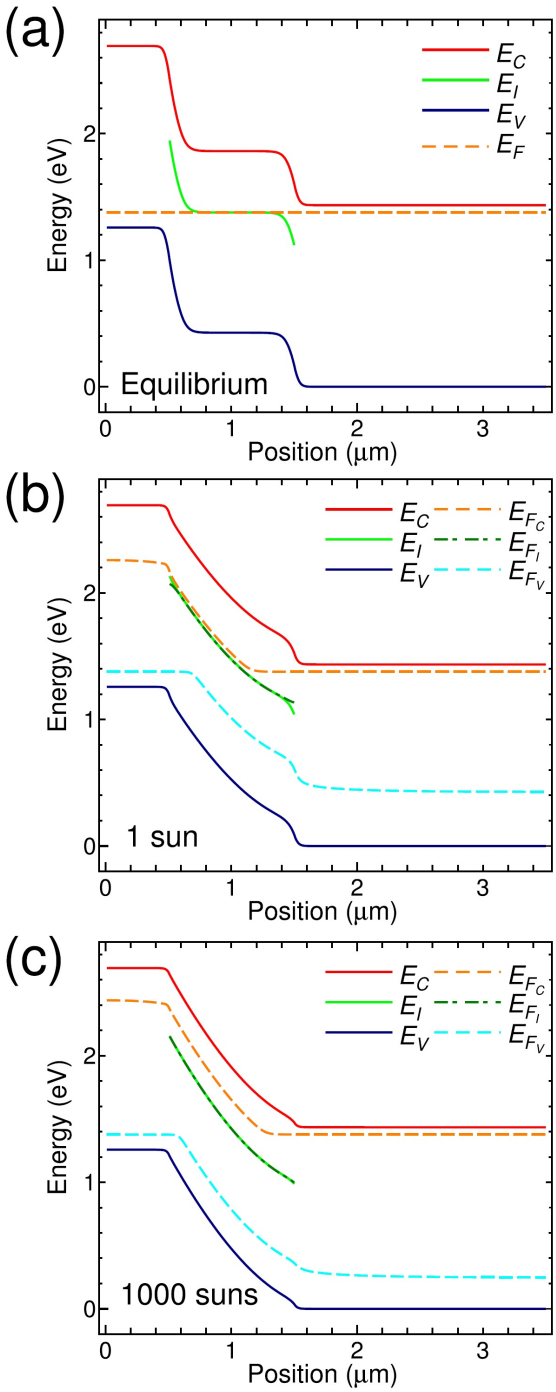


Fig. 1.6 Taken from [25]. Band profile of an IBSC in short-circuit condition along x-direction with doped IB in three conditions: (a) in equilibrium, (b) under 1 sun illumination, and (c) under 1000 suns illumination. $E_C$ and $E_V$ represent the band edge of CB and VB, respectively, and $E_I$ is that of IB. $E_{FC}$ ; $E_{FI}$ ; and $E_{FV}$ are the quasi-Fermi levels of electrons in CB, IB and of holes in VB, respectively.

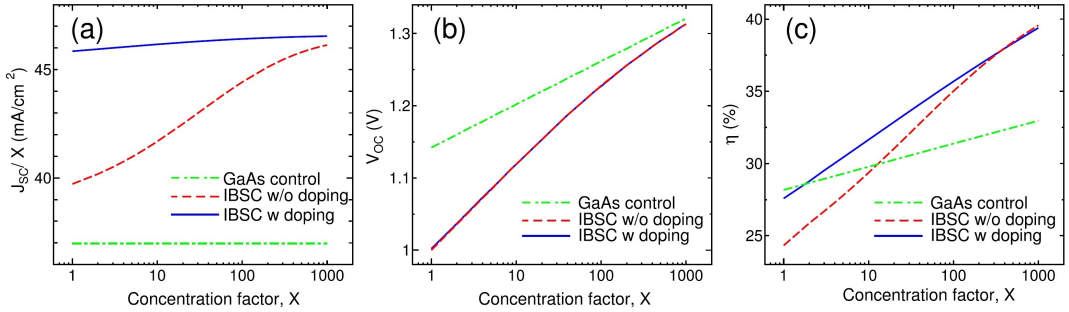


Fig. 1.7 Taken from [25]. (a) $J_{sc}$, (b) $V_{oc}$, and (c) conversion efficiency $\eta$ for IBSCs with undoped and doped IB and for GaAs control cell as a function of the light concentration factor X. $J_{sc}$ is normalized by the light concentration factor X.

## 1.4 Interband recombination

Intraband recombination is another important aspect of the IBSC since fast interband recombination limits the efficiency of the cell by reducing the population of carriers in the IB [24]. Assuming the cell to be at radiative limit (without non-radiative recombination), the intraband recombination can be presented as the spontaneous emission rate ($r_{sp}$) that is proportional to the density of photon states ($g_\gamma$) and the integration over carriers that can participate in transitions that would conserve energy and momentum. The conservation of energy can be ensured by evaluating the final state at energy $\varepsilon' + \hbar\omega$. Assuming negligible change in k-space in optical transitions, the spontaneous emission rate can be written as

$$r_{sp}(\hbar\omega) = g_\gamma(\hbar\omega)\, M\left(\varepsilon', \hbar\omega\right) n_u\left(\varepsilon'\right) n_o\left(\varepsilon' + \hbar\omega\right) \tag{1.8}$$

Where $n_o$ and $n_u$ being the occupied and unoccupied carrier population, respectively. $M$ being interband momentum matrix in order to ensure the conservation of momentum. The total recombination can be derived by integrating over the all possible energies.

$$R_{sp}(\hbar\omega) = \int_0^\infty r_{sp}(\hbar\omega)\, d(\hbar\omega) \tag{1.9}$$

The most commonly used model for integrated recombination rate is the bimolecular recombination equation.

$$R_{sp}(\hbar\omega) = B(n_0 + \Delta n)(p_0 + \Delta p) \tag{1.10}$$

Where $B$ is the spontaneous emission coefficient ($cm^{-6}s^{-1}$). $n_0$ and $p_0$ are the equilibrium carrier concentrations ($cm^{-3}$), $\Delta n$ and $\Delta p$ are the excess carriers ($cm^{-3}$) with respect to the equilibrium condition. In the low injection limit, carrier lifetime can be derived from the rate equation for the excess carriers.

$$\tau_{rad} = \frac{1}{B(n_0 + p_0)} \tag{1.11}$$

Equation 1.11 draws special attention to the dependency of radiative lifetime on equilibrium concentration in a degenerate semiconductor. Accordingly, doping significantly affect the radiative recombination lifetime. In addition to equilibrium carrier concentration, the radiative lifetime also depends on the absorption coefficient through the $B$ coefficient. In general, semiconductor with high absorption coefficient also yields fast radiative recombination. From the application of the detailed balance, assuming that in equilibrium the photon emission rate is the same as the absorption rate, the $B$ coefficient can be calculated from the absorption coefficient spectrum according to [26]

$$B = \frac{8\pi}{h^3 c^2} \int_{E_g}^{\infty} \alpha(E) E^2 \frac{1}{exp\left(\frac{E}{k_B T}\right) - 1} \tag{1.12}$$

## 1.5 Review of literature models

Modeling of QDSCs has been treated as IBSC modeling through detailed balance principle [27–29] and semi analytical or numerical drift diffusion approaches [25, 30, 31, 29, 32, 33]. While all these studies treated the QDs as a single discrete energy level corresponding to the QD ground state, Strandberg and Reenaas [34] modeled the IBSC through detailed balance principle and took the transitions among multiple states into account. Martí et al. [33] modeled the IBSC adopting quasi-drift diffusion model that holds under quasi-charge neutrality assumption. In that study the total current was assumed to be prevailed by the diffusion component and the

equations were solved by applying the low-injection approximation. Lin and Phillips [32] numerically investigated the IBSC through the drift-diffusion approach and clarified the behavior of the potential profile with respect to the IB filling at short circuit. However, the dependence of the optical generation on IB occupancy was neglected in their model. Yoshida et al. [31] included the dependency of carrier generation and recombination on the IB occupancy in a drift-diffusion simulation. The study highlighted the role of IB occupancy and demonstrated the modification of the potential profile when accounting for IB occupancy. Strandberg and Reenaas [29] studied the comparison between prefilled (doping) and photofilled intermediate level in an IBSC at radiative limit with a similar approach to the one in [33]. Tobías et al. [30] developed an IBSC drift diffusion simulator accounting for non radiative recombination and illustrated the essence of having partially filled IB in order to limit the thermal coupling between IB and host bands.

Models of IBSCs usually neglect thermally activated transitions and thus have limited application to the analysis and design of practical devices. To fill this gap, we use a drift-diffusion based model of QD solar cells [35] which includes a proper treatment of quantum carrier capture and escape and proven its ability to explain inherent limitations and experimental results of InAs/GaAs QD solar cells.

# Chapter 2

# The Model

The drift-diffusion model is the most widely used mathematical approach to describe semiconductor devices. However, in some cases, for instance quantum dot devices, the physics governing the device performance are not sufficiently covered in this model. In this chapter, first, the model proposed by Gioannini et al. [35] is described. Then, it is applied to a real case study that was investigated in experimental works by Bailey et al. [14, 13] and Hubbard et al. [36] in order to validate the model and also to analyze the influence of few technological parameters.

## 2.1 Quantum dot solar cell physics-based model

QD based solar cells usually exploit a p-n or p-i-n structure with a region including a periodic stack of QD layers with certain (typically $10^{10} - 10^{11}\text{cm}^{-2}$) in-plane density. QDs are assumed as single nodes with local capture range that is empirically related to the physical thickness of the wetting layer (WL) as will be discussed later. The model does not account for the in-plane coupling since a QD solar cell may work as an IBSC regardless of formation of a miniband [37]. In figure 2.1 the energy band diagram of a quantum dot p-i-n device along with the energy states and the involved interband and intersubband transitions is shown. Growing quantum dots embedded in a semiconductor barrier introduces sub-bandgap discrete energy levels for electrons and holes due to the 3D carrier confinement. These energy states are 0-D bound states, namely ground state (GS), excited states (ES), and a quasi 2-D wetting layer (WL). The relative energy separation of these states depends on the size,

materials involved, the growth process and the lattice strain caused by QD assembling. This energy discretization and its influence cannot be investigated through the drift-diffusion model alone unless solving Schrodinger's equation self-consistently with the drift-diffusion model which does not have a reasonable computation cost.

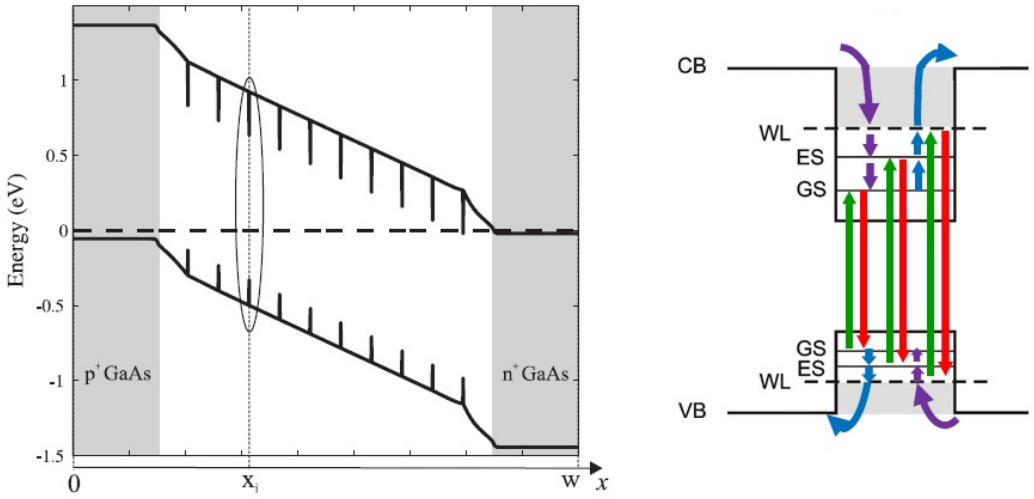


Fig. 2.1 A sketch of the energy band diagram of a p-i-n QDSC along with the energy states of a quantum dot

In order to carry out a detailed study of quantum dot solar cells, the QD physics-based model proposed in [35] is used. In the model, the classical drift-diffusion equations for transport of bulk carriers are coupled with a set of rate equations describing the quantum dot carrier dynamics. The model accounts for band to band charge transfer for photogeneration and recombination whereas, the charge transfer between subband energy states happens through cascaded intersubband capture and relaxation. Intersubband optical processes have been neglected for InAs/GaAs material system since their contribution are negligible at room temperature [38]. The intersubband optical transitions become important when considering other material systems with relatively higher energy band separations in which the thermal transitions are suppressed [18]. The carrier transport within the device is modeled by drift-diffusion equations that relate 3D bulk carrier volume densities $n$ and $p$, 2D sublevel carrier surface densities $n_k$ and $p_k$ ($k$ being GS, ES or WL) in each dot and the electrostatic potential $\phi$. The WL state is treated as 0-D state with high degeneracy factor accounting for the quasi 2-D density of states of the WL and QD weakly confined states. The coupling between the QD layers is neglected

and assumed to be suppressed by the barrier between the two layers. Under such hypothesis, the QDSC operates as follows: electron and holes are photogenerated in the barrier and QD states by above and below energy gap photons, respectively. Charge transfer between continuum and bound states is characterized by capture and escape processes through the WL. In the barrier carriers move by drift-diffusion and when they reach within the interaction range of the QD region (a few nm), they can be either emitted through the QD layer or captured in QD states. Dually, confined carriers may escape from QD states through thermal emission to the WL and from the WL to the barrier. Electric field assisted mechanisms is also neglected because, in case of InAs/GaAs QD material system, thermal emission is so efficient that the inclusion of electric field assisted mechanism does not have any significant influence on the results.

1. Current equations

$$J_n = -qn(x)\,\mu_n \frac{\partial \phi}{\partial x} + qD_n \frac{dn}{dx}$$

$$J_p = -qp(x)\,\mu_p \frac{\partial \phi}{\partial x} - qD_p \frac{dp}{dx}$$

2. Continuity equations

$$\frac{\partial n}{\partial t} = \frac{1}{q}\frac{\partial J_n}{\partial x} - U_n^{\mathrm{B}} + G_{\mathrm{ph}}^{\mathrm{B}} - \sum_i \left(R_{n,\mathrm{cap}}^{\mathrm{B}\to\mathrm{WL},i} - R_{n,\mathrm{esc}}^{\mathrm{WL},i\to\mathrm{B}}\right)\delta(x-x_i)$$

$$\frac{\partial p}{\partial t} = -\frac{1}{q}\frac{\partial J_p}{\partial x} - U_p^{\mathrm{B}} + G_{\mathrm{ph}}^{\mathrm{B}} - \sum_i \left(R_{p,\mathrm{cap}}^{\mathrm{B}\to\mathrm{WL},i} - R_{p,\mathrm{esc}}^{\mathrm{WL},i\to\mathrm{B}}\right)\delta(x-x_i)$$

3. Poisson's equation

$$\frac{\partial^2 \phi}{\partial x^2} = -\frac{q}{\varepsilon}\left(p - n + N + \sum_{i,k}\left(p_{k,i} - n_{k,i}\right)\delta(x-x_i)\right)$$

Where $U_n^{\mathrm{B}}$ is the net band to band recombination rate ($\mathrm{cm}^{-3}\mathrm{s}^{-1}$), $G_{\mathrm{ph}}^{\mathrm{B}}$ is the band to band photogeneration rate ($\mathrm{cm}^{-3}\mathrm{s}^{-1}$), $N$ is the net doping and index $i$ identifies the QD $i$th layer. Charge transfer processes involving 3D bulk states and QD states take place at QD layer position $x_i$ and described by per-unit-area ($\mathrm{cm}^{-2}\mathrm{s}^{-1}$) electron capture rate $R_{n,\mathrm{cap}}^{\mathrm{B}\to\mathrm{WL},i}$ and escape rate $R_{n,\mathrm{esc}}^{\mathrm{WL},i\to\mathrm{B}}$. The continuity equations describe the change in carrier densities over time resulting from the difference between the incoming and outgoing charges plus the net generation-recombination contributions plus the net escape rate from QD into barrier.
In the current equations the current density $J$ consists of two terms. One is related to the motion of charged carriers under the effect of electric field, which is called drift current component and it is proportional to the applied electric field $E$ ($\mathrm{Vcm}^{-1}$), the mobility of carriers $\mu$ ($\mathrm{cm}^2\mathrm{V}^{-1}\mathrm{s}^{-1}$) and the charge volume density $n$ or $p$ ($\mathrm{cm}^{-3}$). The second term which is called diffusion current component is related to the motion of carriers due to the thermal energy, $kT$, which causes carriers to spread out or redistributed even when no field is applied. The net diffusion current is zero unless a carrier gradient is present that leads to flow of carriers from region of higher concentration to lower one. Therefore, this term is proportional to carrier gradient $\frac{dn}{dx}$ and diffusivity $D$ ($\mathrm{cm}^2\mathrm{s}^{-1}$). Diffusivity $D$ and mobility $\mu$ are related through Einstein's relation

$$D = \mu \frac{kT}{q} \tag{2.1}$$

$U_n^{\mathrm{B}}$ includes both radiative and non-radiative recombination. Radiative recombination is modeled as:

$$U_{\mathrm{B,r}} = B\left(np - n_i^2\right) \tag{2.2}$$

Where $B$ is the spontaneous emission coefficient ($\mathrm{cm}^{-6}\mathrm{s}^{-1}$) and $n_i$ is the thermal equilibrium carrier density ($\mathrm{cm}^{-3}$).
Non-radiative recombination follows Shockley-Read-Hall theory:

$$U_{\mathrm{B,nr}} = \frac{\left(np - n_i^2\right)}{\tau_p\left(n + n_1\right) + \tau_n\left(p + p_1\right)} \tag{2.3}$$

Where $\tau_{n(p)}$ is the SRH recombination lifetime, $n$ and $p$ are the carrier densities and $n_1$, $p_1$ are the electron and hole densities when Fermi level corresponds to the trap

energy level:

$$n_1 = n_{i,\text{eff}}\, exp\left(\frac{E_{\text{trap}}}{kT}\right) \tag{2.4}$$

and:

$$p_1 = n_{i,\text{eff}}\, exp\left(\frac{-E_{\text{trap}}}{kT}\right) \tag{2.5}$$

The rate equations governing the subband populations in the $ith$ quantum dot layer are described as following forms:

$$\frac{\partial n_{\text{WL},i}}{\partial t} = R_{n,\text{cap}}^{\text{B}\rightarrow\text{WL},i} - R_{n,\text{esc}}^{\text{WL},i\rightarrow\text{B}} - R_{n,\text{cap}}^{\text{WL},i\rightarrow\text{ES},i} + R_{n,\text{esc}}^{\text{ES},i\rightarrow\text{WL},i} - U^{\text{WL},i} + G_{\text{ph}}^{\text{WL},i} \tag{2.6}$$

$$\frac{\partial n_{\text{ES},i}}{\partial t} = R_{n,\text{cap}}^{\text{WL},i\rightarrow\text{ES},i} - R_{n,\text{esc}}^{\text{ES},i\rightarrow\text{WL},i} - R_{n,\text{cap}}^{\text{ES},i\rightarrow\text{GS},i} + R_{n,\text{esc}}^{\text{GS},i\rightarrow\text{ES},i} - U^{\text{ES},i} + G_{\text{ph}}^{\text{ES},i} \tag{2.7}$$

$$\frac{\partial n_{\text{GS},i}}{\partial t} = R_{n,\text{cap}}^{\text{ES},i\rightarrow\text{GS},i} - R_{n,\text{esc}}^{\text{GS},i\rightarrow\text{ES},i} - U^{\text{GS},i} + G_{\text{ph}}^{\text{GS},i} \tag{2.8}$$

Where $n_{\text{GS},i}$, $n_{\text{ES},i}$ and $n_{\text{WL},i}$ are the electron sheet densities in the GS, ES and WL. $U^{k,i}$ and $G_{\text{ph}}^{k,i}$ are net band to band recombination and photogeneration rates in $k$th state ($k$ being B, GS, ES and WL). We assume Boltzmann statistics for the occupation of WL and bulk states, while for the QD confined states (GS and ES), Fermi-Dirac statistics was exploited. Capture and relaxation processes $R_{n,\text{cap}}^{\gamma,i\rightarrow\gamma-1,i}$ and $R_{n,\text{esc}}^{\gamma-1,i\rightarrow\gamma,i}$ of an electron between $\gamma$ and $\gamma-1$ states are formulated as:

$$R_{n,\text{cap}}^{\gamma,i\rightarrow\gamma-1,i} = \frac{N_\gamma}{\tau_{n,\text{cap}}^{\gamma,i}} f_{n,\gamma}\left(1 - f_{n,\gamma-1}\right) \tag{2.9}$$

$$R_{n,\text{esc}}^{\gamma-1,i\rightarrow\gamma,i} = \frac{N_{\gamma-1}}{\tau_{n,\text{esc}}^{\gamma-1,i}} f_{n,\gamma-1}\left(1 - f_{n,\gamma}\right) \tag{2.10}$$

With $\gamma$ being B, WL, ES and $f_{n,\gamma(\gamma-1)} = n_{\gamma(\gamma-1)}/N_{\gamma(\gamma-1)}$ being the occupation probability of the state $\gamma$ with effective density of states $N_\gamma$. $\tau_{n,\text{cap}}^{\gamma}\left(\tau_{n,\text{esc}}^{\gamma-1}\right)$ is the time constant for capture (escape) of electrons into (from) $\gamma(\gamma-1)$ state. The capture and escape time constants are generally position dependent through the dependence

on local carrier density and electric field. Moreover, carrier escape and capture processes between the 3D continuum state and 2D WL involves the evaluation of the equivalent sheet carrier density in the barrier states scattering with the WL states. This evaluation is done by introducing an effective bulk surface density given as $N_{\mathrm{B}} = N_{\mathrm{c}}\, t_{\mathrm{QD}}$ , where $N_{\mathrm{c}}$ is the conduction band density of states and $t_{\mathrm{QD}}$ is QD capture range which is empirically related to the physical thickness of the WL layer [39].
Respecting the detailed equilibrium principle, under thermal equilibrium the capture and escape rates between two states are equal

$$R_{n,\mathrm{cap}}^{\gamma,i\rightarrow\gamma-1,i} = R_{n,\mathrm{esc}}^{\gamma-1,i\rightarrow\gamma,i} \tag{2.11}$$

Therefore, the capture and escape time are related by:

$$\tau_{n,\mathrm{esc}}^{\gamma-1,i} = \frac{N_{\gamma-1}}{\gamma}\tau_{n,\mathrm{cap}}^{\gamma-1,i} exp\left(\frac{E_{\gamma}-E_{\gamma-1}}{kT}\right) \tag{2.12}$$

Finally, band to band recombination rate for the confined states is modeled as:

$$U^{\gamma,i} = \frac{N_{\gamma}}{\tau_{r,\gamma}}\left(f_{n,\gamma}f_{p,\gamma} - f_{n,\gamma}^{0}f_{p,\gamma}^{0}\right) \tag{2.13}$$

Where $f_{n,\gamma}^{0}$ and $f_{p,\gamma}^{0}$ are the thermal equilibrium occupation probability, $N_{\gamma}$ is the effective density of states and $\tau_{r,\gamma}$ is the radiative lifetime of the $\gamma$ state. Optical photogeneration is assumed to be an exponential decay of the optical intensity through the barrier which is characterized by the bulk optical absorption $\alpha_{\mathrm{B}}(\lambda)$, and a finite transmittance of the dot layer induced by intraband transitions between the discrete levels. The QD transmittance is described as:

$$T_{\mathrm{QD}}(\lambda) = 1 - \sigma_{\mathrm{QD}}(\lambda)N_{\mathrm{QD}}(\lambda) = [1 - \sum \sigma_{\gamma,i}(\lambda)]N_{\mathrm{QD}} \tag{2.14}$$

Where $N_{\mathrm{QD}}$ is the QD areal density ($\mathrm{cm}^{-2}$) and $\sigma_{\gamma,i}$ is the per-dot cross-section which is calculated as a function of wavelength and occupation probability as follows:

$$\sigma_{\gamma,i}(\lambda) = \sigma_{0}[1 - f_{n,\gamma}^{i}f_{p,\gamma}^{i}] \tag{2.15}$$

Then optical generation rates are evaluated as:

$$G_{\mathrm{ph}}^{\mathrm{B}} = \int_{\lambda} \eta_{ill}(\lambda)\,\alpha_{\mathrm{B}}(\lambda)\,\Phi(\lambda,x)\,d\lambda \tag{2.16}$$

$$G_{\mathrm{ph}}^{\gamma,i} = \int_{\lambda} \eta_{ill}(\lambda)\,\sigma_{\gamma,i}(\lambda)\,N_{\mathrm{QD}}\Phi(\lambda,x)\,d\lambda \tag{2.17}$$

Where $\eta_{ill}(\lambda)$ accounts for the reflection loss at the input facet, $\Phi(\lambda,x)$ is the spectral photon flux density ($\mathrm{cm}^{-2}\ \mathrm{s}^{-1}\mu^{-1}$) between two consecutive QD layer is given as:

$$\Phi(\lambda,x) = \Phi(\lambda,x=0)\exp(-\alpha_{\mathrm{B}}(\lambda)\,x)\prod T_{\mathrm{QD},i}(\lambda) \tag{2.18}$$

Where the product accounts for the attenuation of the QD layers before the $x$ section. A finite element model [40] has been adopted to implement the above formulation. The drift-diffusion model is discretized along the whole device, whereas a single mesh point is associated with each QD layer. The resulting system of discretized equations is then solved self-consistently using Newton-Raphson method.

## 2.2 Simulation of an undoped InAs/GaAs quantum dot solar cell

In this section the analysis of an undoped InAs/GaAs QDSC is presented. The goal is to validate the model and also analyzing the influence of few technological and geometrical parameters such as QD areal density, number of QD stacks and intrinsic region (embedding QDs) thickness. The geometry of the investigated device is summarized in figure 2.2. The structure is similar to the one investigated in a number of experimental studies [14, 13, 36]: a p-i-n GaAs solar cell embedding 10 stacks of strained balance InAs QDs with high uniformity and areal density of $3.6\times10^{10}$ $\mathrm{cm}^{-2}$ in the intrinsic region. The 100 nm intrinsic region is sandwiched between 2 $\mu$m n-doped ($1\times10^{17}$ $\mathrm{cm}^{-3}$) and 500 nm p-doped ($1\times10^{18}$ $\mathrm{cm}^{-3}$) GaAs. The cell also features two thin (50 nm) highly doped ($5\times10^{18}$ $\mathrm{cm}^{-3}$) InGaP front and back surface layer and illuminated from the p-side. Wide bandgap materials are generally used for surface passivation to make potential barrier for minority carriers so that they are deflected away from the contacts [41].


Fig. 2.2 The GaAs p-i-n structure.

In the model the transitions among QD subbands and continuum states are described by time constants $\tau^k_{\text{cap}}$ and $\tau^k_{\text{esc}}$. The electron capture and relaxation time constants are taken from [35] in which the QD subband capture time were estimated from fitting the measured data of an InAs/GaAs QD sample in [42] with time-domain solution of QD rate equations in [43]. The thermal-assisted escape time is then calculated according to equation 2.12. Concerning holes, due to the closely separated QD valence band states, their capture and relaxation are assumed to be fast processes with time constant on the order of 100 fs [35]. The energy position of the QD confined states and the wetting layer with respect to the continuum are extracted from the subband EQE peaks reported in [14]. Optical generation is computed by photon absorption using Beers law assuming exponential decay of the optical intensity through the barrier. The absorption coefficient of the QD states are shown in figure 2.3. Electron and hole low field mobility for GaAs are assumed to be $\mu_n = 8500\ \text{cm}^2\text{V}^{-1}\text{s}^{-1}$ and $\mu_p = 400\ \text{cm}^2\text{V}^{-1}\text{s}^{-1}$ respectively and high field velocity saturation is taken into account according to Caughey-Thomas model [44] with saturated velocity of $v_{n,\text{sat}} = 1 \times 10^7\ \text{cm}^{-1}$ and $v_{p,sat} = 8.37 \times 10^6\ \text{cm}^{-1}$. Photon recycling is neglected in the simulation and the band-to-band recombination rate

is calculated using equation 2.2 with the radiative recombination constant B = $7.2 \times 10^{-10}$cm$^3$s$^{-1}$ computed from the GaAs absorption spectrum according to "Van Roosbroeck-Shockley" relation [26].

Figures 2.4 and 2.5 show the current density-voltage (J-V) and external quantum efficiency (EQE) of the QDSC and reference bulk cell (without QDs) at room temperature. The measurements are taken from [14] in which ten-layer InAs/GaAs QDSC with optimized InAs coverage value (1.8 ML) as well as a 3D-modified strain balancing technique was reported to maintain open circuit voltage (at 994 mV) comparable to a control GaAs p-i-n solar cell. The simulation results are qualitatively in good agreement with the experimental one and, consistently with literature experimental data, the QDSC has slight improvement in terms of short circuit current ($J_{sc}$) and reduced open circuit voltage ($V_{oc}$) with respect to the bulk cell.

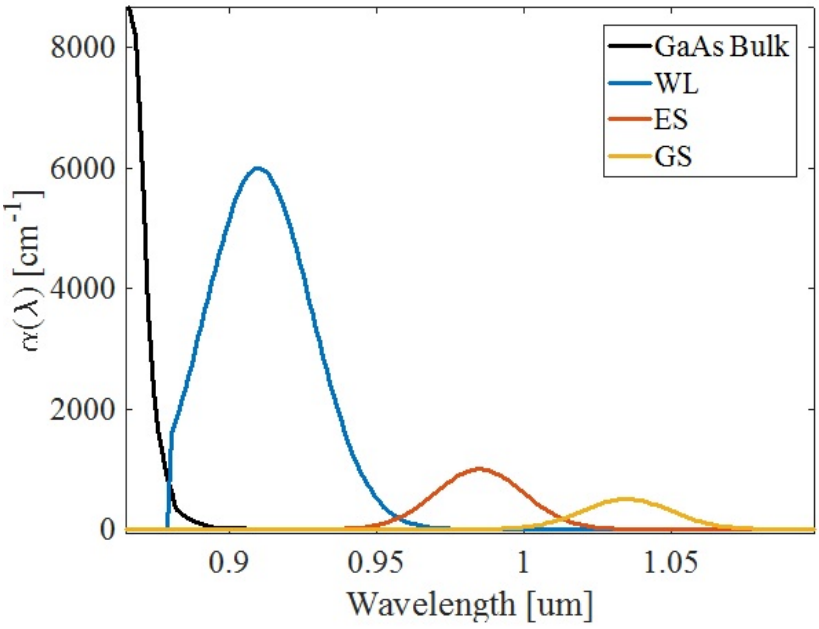


Fig. 2.3 Wavelength dependence of the absorption coefficient of GS, ES and WL states with wavelength peaks at 1035, 980 and 910 nm respectively. The absorption coefficient tail of the bulk GaAs is also presented.

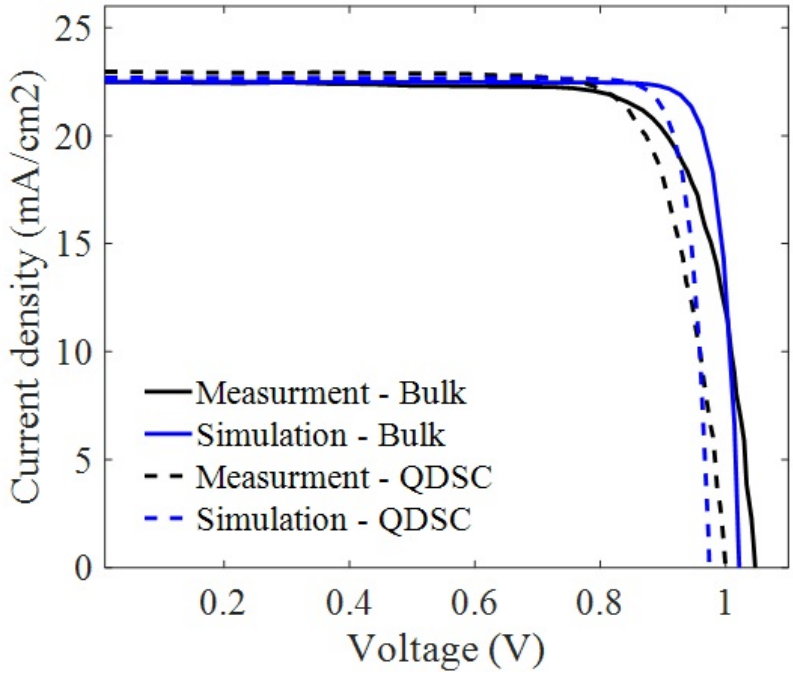


Fig. 2.4 Current density- voltage characteristic of the cell with and without QDs under AM0 solar illumination. The measurements are taken from [14]

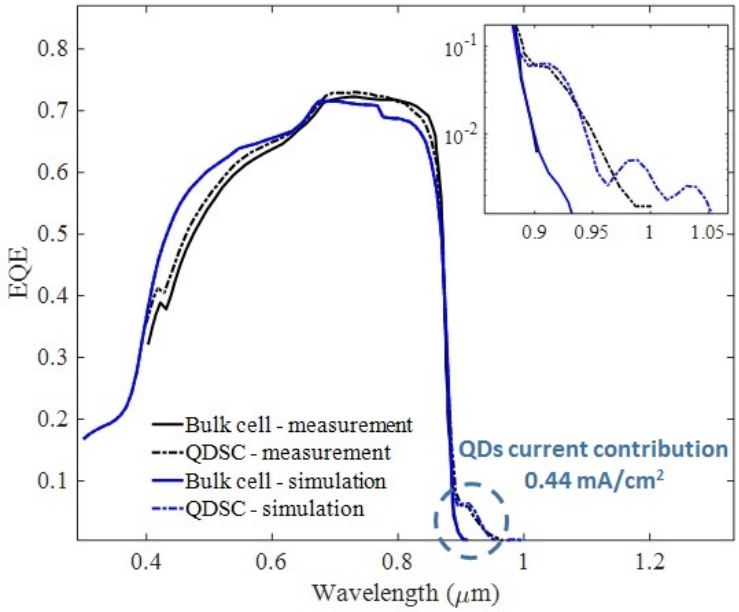


Fig. 2.5 External quantum efficiency (EQE) of the cell with and without QDs. The inset is the subband regime in logarithmic scale. The measurements are taken from [14]

The small improvement in short circuit current which is also highlighted in EQE spectra can be understood by looking at the spatial distribution of QDs net carrier escape rate at short circuit condition. In the model, since the charge transfer between subband energy states is assumed to occur through cascaded intersubband capture and relaxation processes, the QD net escape rate is equal to the net escape rate from WL to continuum state ($R_{esc}^{net} = R_{esc}^{WL \to B} - R_{cap}^{B \to WL}$). Figure 2.6 points out the positive electron net escape rate from QDs at short circuit condition meaning that the QDs are contributing to the current. Note that, since the QD layers are embedded in the intrinsic region which is characterized at short circuit by high electric field and almost unitary collection efficiency of photogenerated carriers, the positive carrier net escape rate allows QD photogenerated carriers to be collected in the bulk. Moreover, at short circuit recombination through the QD states is negligible and thermal escape almost equilibrates the QD photogeneration rate. This can be supported by looking at the QD states occupation probability at short circuit condition. Figure 2.7 shows almost two order of magnitude lower occupation probability of valence band states with respect to the conduction band states except for the QD layers near the p-emitter in which the occupation probability is higher because of hole injection from the p-side. The large difference between conduction band and valence band states is attributed to the faster hole dynamics with respect to the electrons due to the closely separated energy levels, meaning that once an e-h pair is generated the hole escapes out of the QD so fast so that it inhibits the band-to-band recombination and as a consequence, to balance with the generation, the electron also has to escape out [35].

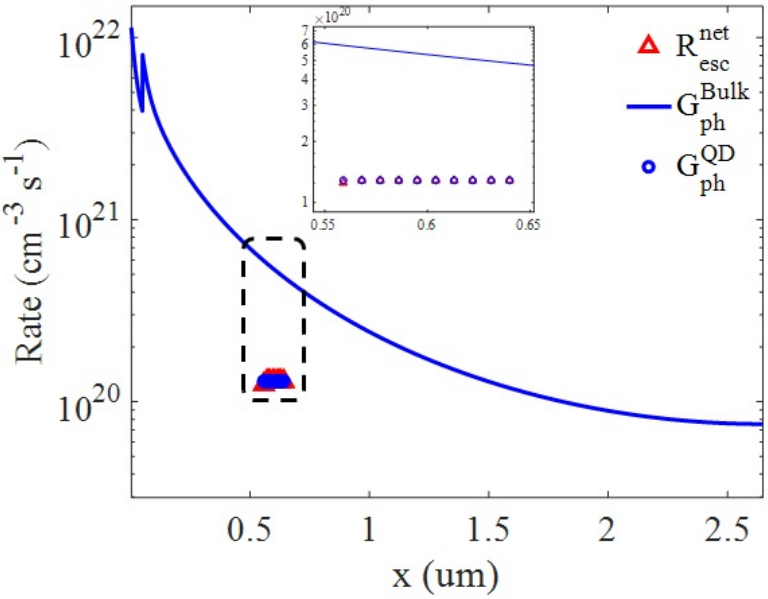


Fig. 2.6 Bulk and QD photogeneration rate together with the electron net-escape rate from WL to the conduction band at short circuit under one sun AM0 illumination.

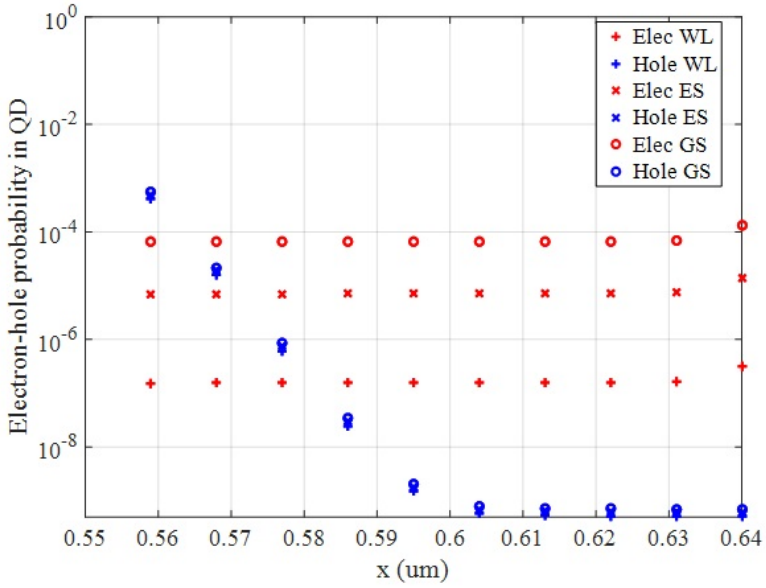


Fig. 2.7 Occupation probability of the electrons (red) and holes (blue) in the GS, ES and WL across the ten QD layers at short circuit condition under one sun AM0 illumination.

In contrast with the short circuit current improvement, figure 2.4 shows a reduction in open circuit voltage in the QDSC with respect to the reference bulk cell. The $V_{oc}$ penalty obtained from the simulation is in good agreement with the experimental one reported in [14]. In order to understand $V_{oc}$ degradation of the QDSC with respect to the reference cell, one can analyze the recombination mechanism at open circuit condition. The spatial distribution of net carrier capture and recombination rates at open circuit is plotted in figure 2.8. Recall that at short circuit, the effectiveness of carrier extraction out of the QDs was quantified by the net escape rate of electrons from WL to the bulk ($R_{\text{esc}}^{\text{net}} = R_{\text{esc}}^{\text{WL}\to\text{B}} - R_{\text{cap}}^{\text{B}\to\text{WL}}$). On the other hand, under forward bias the capture rate of carriers increases due to screening of the electric field and carrier injection from the doped regions that finally causes the carrier capture rate to dominate over the escape rate (see figure 2.9). In other words, at open circuit, QDs act as traps for carriers photogenerated in the bulk and reduce the total current. Concretely, at open circuit condition instead of negative net escape rate, the net capture rate can be defined as $R_{\text{cap}}^{\text{net}} = R_{\text{cap}}^{\text{B}\to\text{WL}} - R_{\text{esc}}^{\text{WL}\to\text{B}}$ as a positive value.

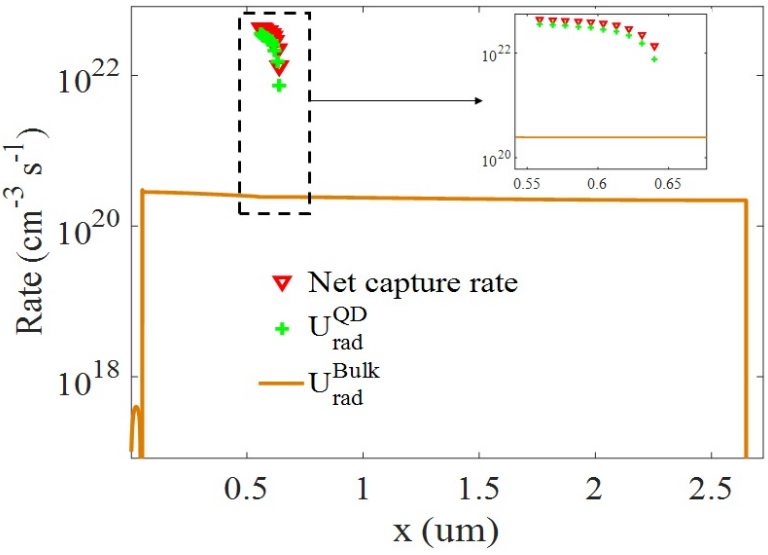


Fig. 2.8 Bulk radiative recombination rate along with the equivalent volume recombination and net capture rates of QD states at open circuit condition.

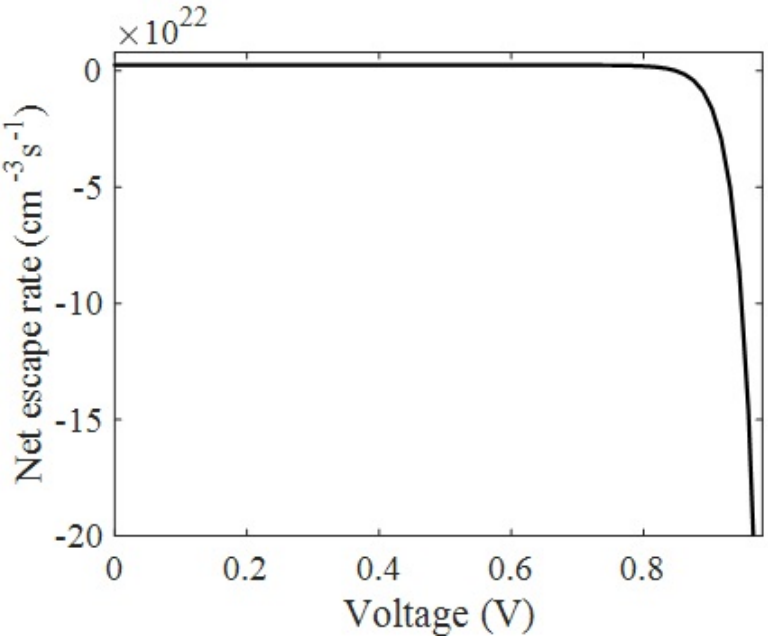


Fig. 2.9 Evolution of net escape rate from WL to the continuum state with respect to voltage.

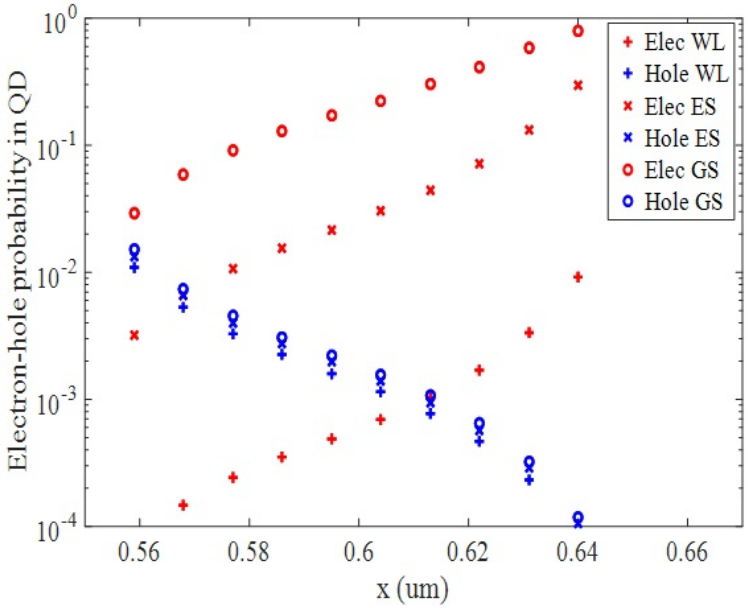


Fig. 2.10 Occupation probability of the electrons (red) and holes (blue) in the GS, ES and WL across the ten QD layers of QDSC at open circuit

Figure 2.8 points out the QD radiative recombination dominance in the intrinsic region. The increase of QD radiative recombination is the result of holes accumula-

tion at open circuit (see figure 2.10). Since holes have lower mobility with respect to the electrons, they have larger probability to get captured by the QDs, therefore the enhancement of states occupation in the valence band with the voltage is more pronounced than in the conduction band. Finally, the open-circuit voltage condition is reached when all the carriers photogenerated in the GaAs are quickly captured into the WL states from where they relax down to the GS and recombine.
The evolution of equivalent QD radiative recombination current for each state with respect to the voltage is shown in Figure 2.11. The equivalent recombination currents are computed by integrating the recombination rates across the device as the voltage changes. The figure highlights the dominance of GS radiative recombination over other states (ES and WL).

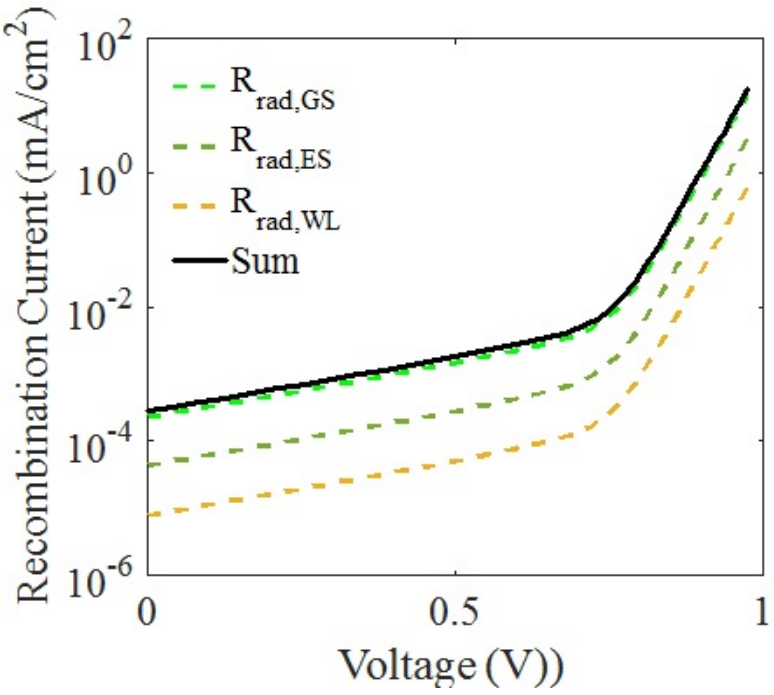


Fig. 2.11 Evolution of radiative recombination through each state of QDs with respect to the voltage.

### 2.2.1 Influence of bulk non-radiative recombination

In our model non-radiative recombination is taken into account by defining an equivalent SRH lifetime $\tau_{SRH}$ as a representative of the crystal quality (ideal cell at

radiative limit has $\tau_{SRH} = \infty$). Following Shockley-Read-Hall theory [45] we have:

$$U_{\mathrm{B,nr}} = \frac{\left(np - n_i^2\right)}{\left(n + n_1\right)\tau_p + \left(p + p_1\right)\tau_n} \tag{2.19}$$

with:

$$n_1 = n_{\mathrm{i,eff}} \exp\left(\frac{E_{\mathrm{trap}}}{kT}\right) \tag{2.20}$$

and:

$$p_1 = n_{\mathrm{i,eff}} \exp\left(\frac{-E_{\mathrm{trap}}}{kT}\right) \tag{2.21}$$

Where $E_{\mathrm{trap}}$ is the difference between the defect level and intrinsic level. $\tau_{n(p)}$ is the SRH recombination lifetime. This recombination mechanism compete with other recombination processes in determining $V_{oc}$. We consider $\tau_n = \tau_p = \tau_{\mathrm{SRH}} = 50$ ns assuming the cell to be defective. However, $V_{oc}$ is shown to be insensitive to the SRH recombination since this recombination process is effective in low doped regions and since the dimension of the intrinsic region is much smaller than that of the cell (100 nm intrinsic region in 2.6 $\mu$m p-i-n structure) $V_{oc}$ is still dominated by the QD radiative recombination. Figure 2.12 shows the calculated recombination current associated to each mechanism with respect to the voltage and shows the dominance of GS radiative recombination at open circuit.

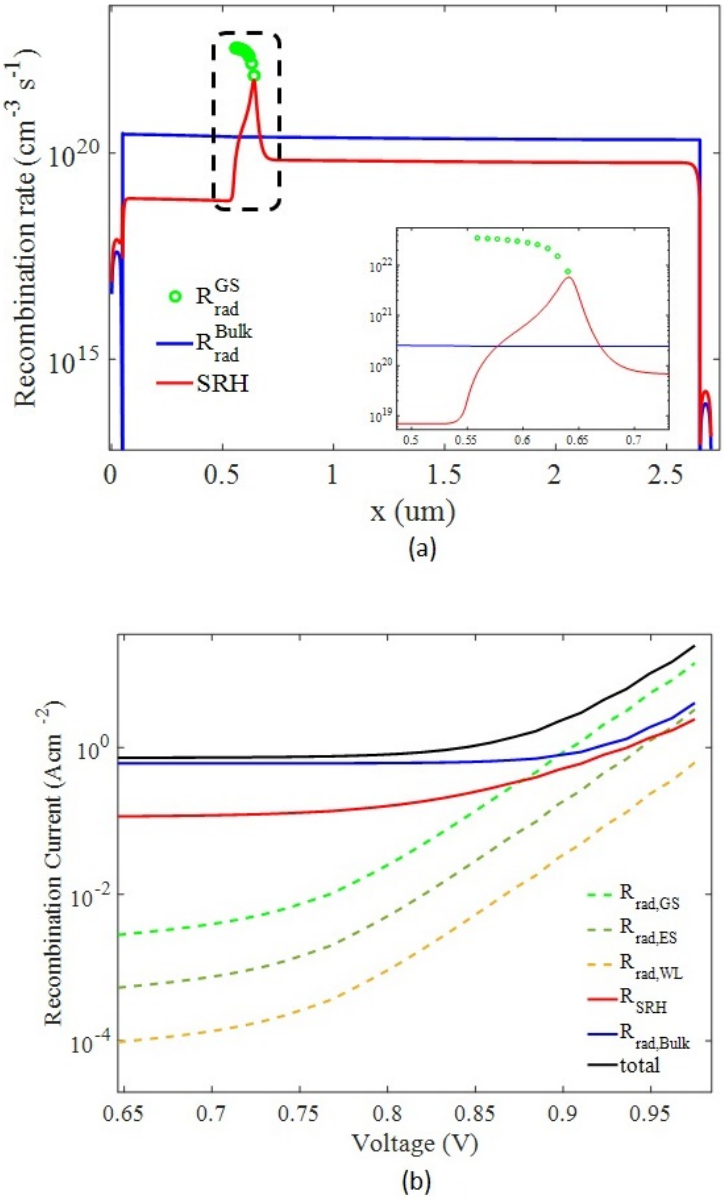


Fig. 2.12 Spatial distribution of recombination mechanisms across the device at $V_{oc} = 0.98\ V$ (a). Evolution of each recombination currents with respect to the voltage (b).

### 2.2.2 Influence of the intrinsic region thickness

The influence of the intrinsic region thickness is investigated considering both ideal and defective cells. The simulation is carried out by expanding intrinsic region over

the base region from 100 nm to 2000 nm. The sketched band diagram at short circuit and open circuit condition is presented in figure 2.13 for three cases: 100 nm, 1000 nm and 2000 nm.

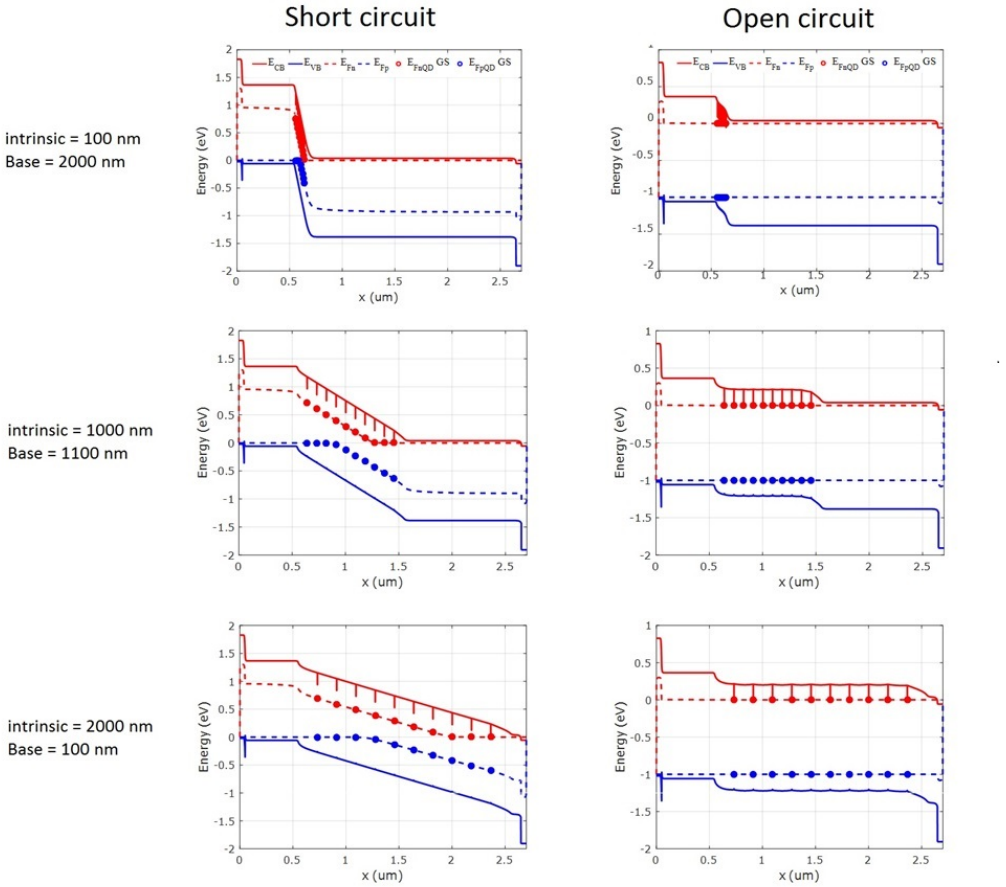


Fig. 2.13 Band diagram at short circuit and open circuit condition of the device with different intrinsic region thickness by maintaining the same total thickness

The behavior of bulk and QDSC open circuit voltage and the corresponding voltage penalty ($V_{oc}^{\text{penalty}} = V_{oc}^{\text{Ref}} - V_{oc}^{\text{QDSC}}$) is shown in figure 2.14.

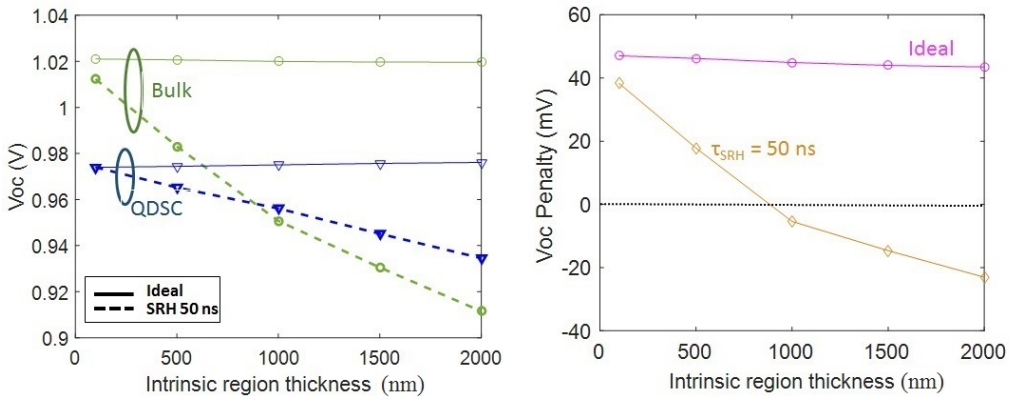


Fig. 2.14 Open circuit voltage of the device with respect to intrinsic region thickness for reference cell and QDSC assuming both ideal and defective ($\tau_{\mathrm{SRH}} = 50$ ns) crystal quality

The figure reveals that in ideal device, $V_{oc}$ is almost insensitive to intrinsic layer thickness while in defective cells, it monotonically decreases. The $V_{oc}$ degradation is associated to the enhancement of SRH recombination due to the intrinsic region enlargement. Furthermore, in defective case for enough thick intrinsic layer (>1000 nm), the $V_{oc}$ of the QDSC becomes larger than of the reference cell (the $V_{oc}$ penalty becomes negative). This voltage gain is associated to the reduced SRH recombination of QDSC with respect to the reference cell. To gain a better insight, the recombination currents at open circuit are plotted with respect to intrinsic region thickness in figure 2.15 for both bulk and QDSC. The figure highlights the interplay between SRH and QD radiative recombination in the QDSC. Moreover, the crossing point between the two overall recombination current $R_{\mathrm{tot}}$ represents the point in which the $V_{oc}$ penalty becomes negative.

Dark current - voltage analysis is commonly used to investigate the electrical characteristics of solar cells. The magnitude of the dark current and its behavior with respect to the voltage provide necessary information regarding the performance losses. The ideality factor $n$ can be extracted from the slope of the dark JV curve according to the diode equation. The ideality factor suggests the dominant recombination mechanism: $n = 2$ represents non radiative recombination in the space charge region and $n = 1$ indicates that the performance is limited by recombination in quasi-neutral regions. The dark JV characteristics of the QDSC with three different intrinsic region thicknesses are plotted in figure 2.16. All cells, at low voltages (<0.7 V) show ideality factor almost equal to 2 indicating that the cell is dominated by SRH recombination. At higher voltages (near $V_{oc}$), the 100 nm intrinsic region cell is

dominated by QD radiative recombination producing ideality factor approximately 1, while the cells with 1000 and 2000 nm intrinsic region have ideality factor 1.66 and 1.58, respectively, which result from the contribution of both SRH and QD radiative recombination. The change in the slope (ideality factor) for the 100 nm intrinsic region cell is consistent with the behavior of the recombination current with respect to the voltage reported in figure 2.12.

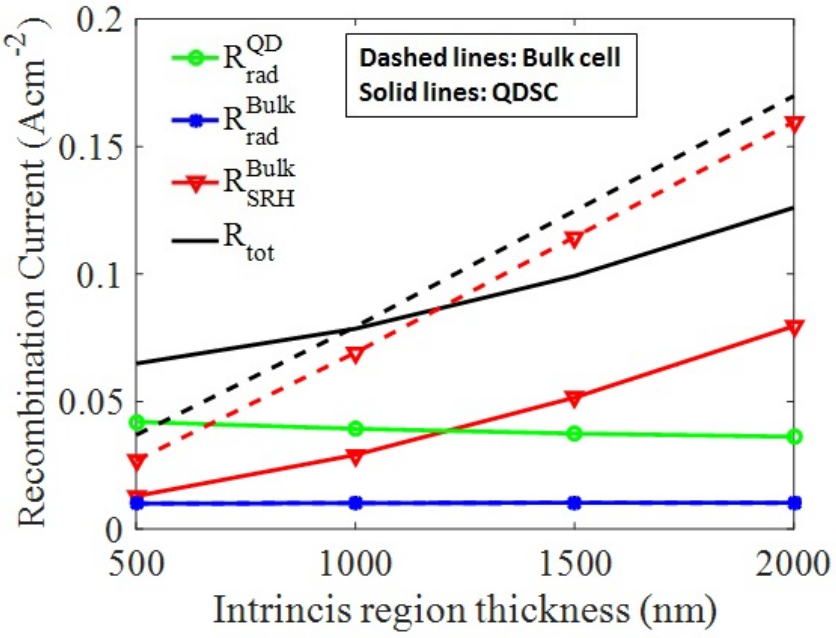


Fig. 2.15 Equivalent recombination currents in the QDSC (solid) and the bulk cell (dashed) with respect to the intrinsic region thickness.

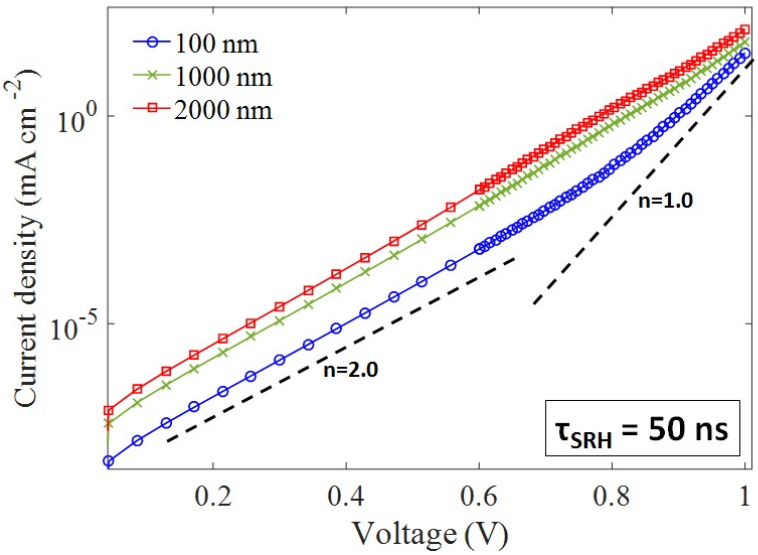


Fig. 2.16 Dark current - voltage characteristic of the QDSC considering three intrinsic region thicknesses. The cell is assumed to have non-radiative recombination with an equivalent $\tau_{\mathrm{SRH}} = 50$ ns. The slopes corresponds to ideality factor 1 and 2 are also plotted for the sake of comparison.

### 2.2.3 Influence of quantum dot in-plane density and number of stacks

Increasing the number of QDs in a solar cell by means of increasing QD in-plane density or number of QD stacks is expected to enhance $J_{sc}$ thanks to the increase in QDs effective absorption. Nonetheless, it also increases QD radiative recombination rate at open circuit which is the limiting factor for $V_{oc}$. Figure 2.17 illustrates the behavior of $V_{oc}$ with respect to the QD plane density considering 10 and 20 layers of QDs and non ideal material ($\tau_{\mathrm{SRH}}$ =50 ns) with different intrinsic region thickness.

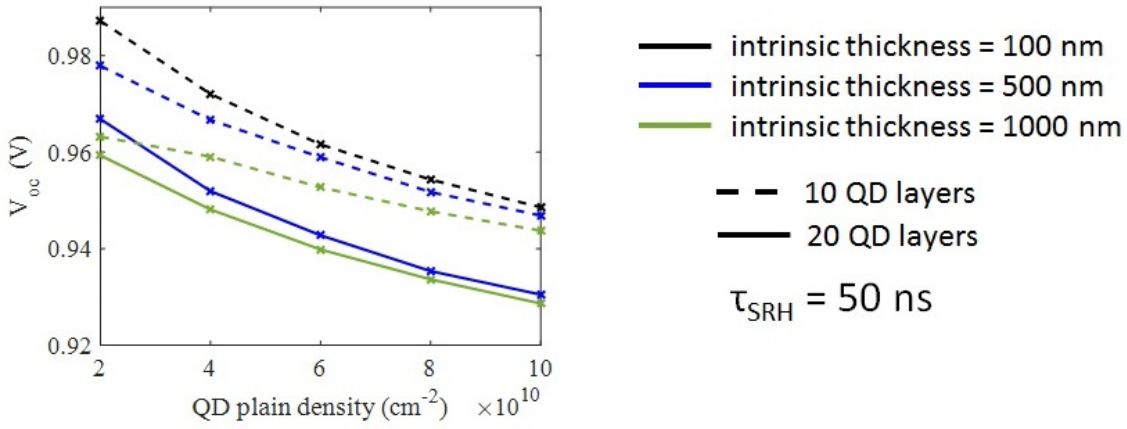


Fig. 2.17 Open circuit voltage of QDSC with respect to QD in-plane density, illuminated at 1 sun AM0 . Dashed line represents QDSC with 10 QD stacks and solid line represents QDSC with 20 QD stacks. The SRH lifetime is assumed to be 50 ns. Note: since its not possible to insert 20 layers of QD stacks with 5 nm barrier between each stacks in 100 nm intrinsic region, the simulation for 20 layers of QDs in 100 nm intrinsic region is omitted

The open circuit voltage degradation is the result of increased recombination current through the QDs. The reduction in $V_{oc}$ with respect to the number of layers is consistent with the experimental results observed in in [13].

# Chapter 3

# Impact of doping on quantum dot solar cells

This chapter is devoted to the detailed numerical study of the impact of doping in quantum dot solar cells by analyzing their behavior in terms of photovoltaic characteristic, external quantum efficiency and photoluminescence at room temperature. The study shows that doping can allow for optimizing the efficiency as shown in figure 3.3, as a result of larger improvement of Voc than decrease of Jsc. The results of our study are published in [46–48]. My specific contribution was to analyze the doping dependent behavior of a bulk cell and the influence of the WL reduction on QDSC which will be discussed in the next chapter. Two doping techniques within the intrinsic region of p-i-n GaAs solar cells embedding quantum dots are investigated. Moreover, the crystal quality is also taken into account by introducing different Shockley-Read-Hall recombination lifetime for the host material. The enhancement of non-radiative recombination induced by quantum dot growth is neglected in order to single out the role of quantum dot charging on recombination processes and charge transfer between bulk and confined states.

## 3.1 Experimental Results

Selective doping (modulation and direct) has been proposed to suppress QD-barrier thermal coupling and mitigate recombination loss [15–17]. Modulation doping is

realized by $\delta$ doping of barrier layers separating the QD stacks [15, 49] whereas, direct doping is obtained by incorporating dopant atoms directly into QDs during the growth [17, 50]. Even though improvement in terms of efficiency with respect to the bulk cell have not been obtained in high quality samples, many experimental studies demonstrated remarkable $V_{oc}$ recovery with respect to the undoped QDSCs. However, the underlying mechanisms and their quantitative impacts were not been assessed clearly.

Although in a bulk cell similar $V_{oc}$ recovery could be expected from p-type and n-type doping, it has been observed that the trend is not the same in quantum dot samples. Sablon et al. [15] compared the PL intensity of n- and p-type doped QDSCs and observed a strong asymmetry of the QDSC behavior with respect to the doping polarity. The PL intensity of p-doped sample was approximately 8 times larger and shown to substantially enhance capture and relaxation processes and increase the recombination loss. The asymmetric behavior of doped QDSCs with respect to the doping polarity was also confirmed by Polly et al. [49] but the explanation was not provided for the significant reduction in $J_{sc}$ . Moreover, the photovoltage recovery was explained by the suppression of SRH recombination in both n- and p-type samples. The same conclusion was also reported in Ref. [51] in terms of photovoltage recovery by analyzing the dark current characteristics of undoped and doped QDSCs. Even though the conclusions in [49, 51] on the suppression of the SRH recombination by doping were correct, these works have not fully addressed the implications of the substantial asymmetry of electron and hole dynamics in QDs.

Concerning n-type modulation doping, in a study by Martí et al. [16], reduced dark current and improved $V_{oc}$ over undoped QD sample is reported. In another study by Polly et al. [49], $\delta$ doped QDSCs were investigated in which substantial $V_{oc}$ recovery were obtained due to the reduction of dark recombination current. Besides, slight reduction in $J_{sc}$ due to the flattened band near the QDs and reduced collection efficiency was shown in doped QDSCs. Regarding n-type directly doped QD cells, uniform array of partially filled QD samples were investigated by Okada et al. [17] in which enhanced photoluminescence, reduced dark current and improved short circuit current were reported. The PL enhancement in doped samples was explained by efficient relaxation of carriers from continuum state into QD states due to the reduction of non-radiative recombination loss from conduction band to valence band. The increase in $J_{sc}$ was noted to be the result of two step photon absorption which was detected under filtered air-mass 1.5 solar spectrum at room

temperature. Emission properties of directly doped QDs were also investigated by Kita et al. [52] that reports a significant increase in PL intensity in doped cells. The improvement of PL was explained by the filling of non radiative electron traps with excess electron charges and from the analysis of time resolved PL measurement, non radiative recombination lifetime was shown to be improved by Si doping. In another experimental study by Yang et al. [53], strong improvement of PL intensity is recorded for directly doped QD sample. Moreover, the efficiency enhancement of around 6% was obtained for appropriate doping level over undoped sample by achieving $V_{oc}$ recovery without reduction in $J_{sc}$. Although subband photocurrent was shown to be diminished in doped sample, the large short circuit current is explained to be due to the lower device loss.
Somewhat In contrast with these results, InAs/GaAs quantum dot solar cell with direct Si doping was studied by Lam et al. [50]. Large $V_{oc}$ recovery in doped quantum dot cells was reported, however, non-radiative recombination was found to be increased with respect to the undoped samples based on $J_{sc}$ and spectral response degradation observation. The large $V_{oc}$ recovery despite having large non-radiative recombination was explained by reduced thermal coupling of QD states from WL and CB. The reduction in $J_{sc}$, based on supra-band reduction observation in EQE, was attributed to defect states induced by Silicon doping.

## 3.2 Device structure and geometrical parameters

The device under investigation is a p-i-n configuration illuminated from the p-side. The p-emitter consists of 50 nm $p^+$- and 100 nm p-GaAs with doping density of $5 \times 10^{18}$ and $1 \times 10^{18}$ $cm^{-3}$ respectively. 1000 nm intrinsic region contains 20 stacks of InAs QDs with QD plane density of $6 \times 10^{10}$ $cm^{-2}$ for each QD layer. The thick intrinsic region is grown with 50 nm intrinsic GaAs buffer layer on top of 300 nm $n^+$ GaAs with doping density of $1 \times 10^{18}$ $cm^{-3}$.
The optical transitions are calculated from the absorption spectrum and accounting for electron and hole occupation probability in the QD energy states. The QD GS and ES states absorption spectra have gaussian shape centered at 1.13 and 1.21 eV with FWHM linewidth of 70 and 50 meV respectively. The absorption spectra of WL is modeled in analogy with the one in quantum well layer [54]. The wavelength

dependent absorption of QD states is shown in figure 3.1. The barrier radiative recombination calculated according to 2.2 with GaAs radiative coefficient $2 \times 10^{-10}$ $cm^3s^{-1}$. Defect induced non radiative recombination is modeled according to SRH relation for non radiative recombination (eq. 2.3) with SRH recombination lifetime ranging from 500 ns (high quality) down to 1 ns (highly defective). $\delta$- doping layers are assumed to be 5 nm thick and are placed in the middle of GaAs spacer or at the QD layer depending on the method of doping (modulation or direct).

Capture and relaxation in InAs/GaAs QDs occur through complicated dynamics that involve emission of longitudinal optical (LO) phonon emission, electron-phonon coupling, defect mediated relaxation, carrier-carrier scattering, etc (see e.g. [55–57] and the reference therein). The capture time $\tau_{cap}$ is typically a function of carrier density in the WL and QD states therefore it depends on operational condition (injection/photogeneration) and doping. At low carrier density, electron-LO phonon interaction and Auger electron-hole are very effective and provide relaxation time on the scale between tenth of ps and tens of ps [55, 56, 58] while, carrier-carrier scattering becomes important at high carrier density, providing again the relaxation time of the order of ps [57]. These scales are also confirmed in experimental studies of undoped and doped samples. In [59] the relaxation time from WL to GS is reported to be 2, 3 and 6 ps for p-doped, n-doped and undoped samples respectively. Experimental and theoretical studies on InAs/GaAs QDs show that the net capture/relaxation are extremely fast with respect to band-to-band (1 ns) and intraband (100 ns) radiative lifetimes [58]. Using empirical data reported by Gioannini et al. [35], we assume very fast capture time from continuum state into WL which occur through LO-phonon interaction on a 0.1 ps time scale, followed by cascade relaxation process into ES and GS. The time constants of about 1 ps is estimated for electrons in [35] for WL-ES and ES-GS relaxation time by fitting time-resolved IR absorption of QD similar to this work. The holes, due to their large effective mass and closely separated energy levels, are characterized with fast phonon mediated capture and relaxation time constant on the order of 100 fs. The QD parameter is summarized in table 3.1.

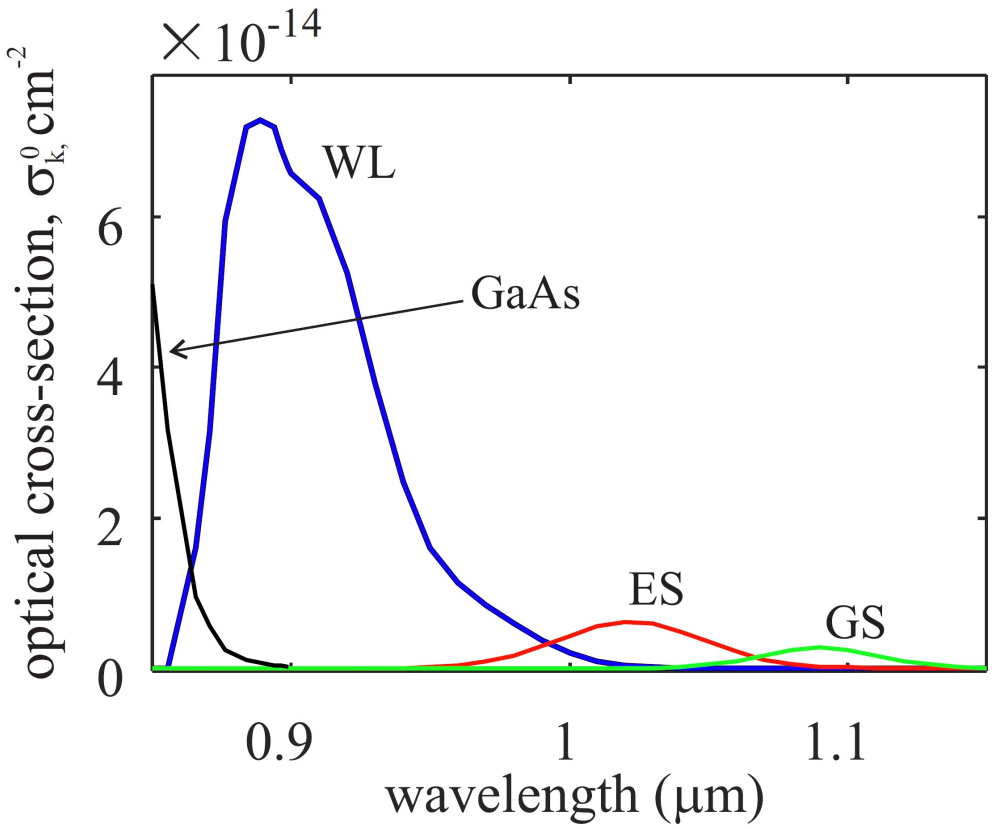


Fig. 3.1 Wavelength dependence of the optical cross-section, $\sigma_k^0$, relative to the WL, ES and GS states used in the simulations (solid lines). The corresponding optical absorption coefficient can be evaluated as $\alpha_k^0 = \sigma_k^0 N_{\mathrm{QD}}/t_{\mathrm{QD}}$, $N_{\mathrm{QD}}$ and $t_{\mathrm{QD}}$ being the QD areal density and thickness, respectively. For the sake of reference also the bulk optical absorption tail is quoted.

Table 3.1 QD Parameters

| | |
|---|---|
| QD plane density [$cm^{-2}$] | $6 \times 10^{10}$ |
| ES and GS degeneracy | 4, 2 |
| WL density of states [$cm^{-2}$] | $2.4 \times 10^{12}$ |
| $\Delta^e_{\text{B-WL}}$, $\Delta^e_{\text{WL-ES}}$, $\Delta^e_{\text{ES-GS}}$ [meV] | 140 62 70 |
| $\Delta^h_{\text{B-WL}}$, $\Delta^h_{\text{WL-ES}}$, $\Delta^h_{\text{ES-GS}}$ [meV] | 4 4 16 |
| $\tau^e_{\text{CAP,B-WL}}$, $\tau^e_{\text{CAP,WL-ES}}$, $\tau^e_{\text{CAP,ES-GS}}$ [ps] | 0.3, 1, 1 |
| $\tau^h_{\text{CAP,B-WL}}$, $\tau^h_{\text{CAP,WL-ES}}$, $\tau^h_{\text{CAP,ES-GS}}$ [ps] | 0.1, 0.1, 0.1 |
| $\tau_r^{\text{WL}}$, $\tau_r^{\text{ES}}$, $\tau_r^{\text{GS}}$ [ns] | 1, 1, 1 |
| QD thickness ($t_{\text{QD}}$) [nm] | 4 |

## 3.3 Simulation of a doped InAs/GaAs quantum dot solar cell

To have an overview of the influence of doping on QDSCs, we calculated the JV characteristics shown in figure 3.2 for the reference GaAs cell (with base residual doping of $1 \times 10^{13}$ $cm^{-3}$), the undoped QDSC and n- and p-type modulation doped cell assuming high quality bulk material with SRH lifetime of 500 ns.

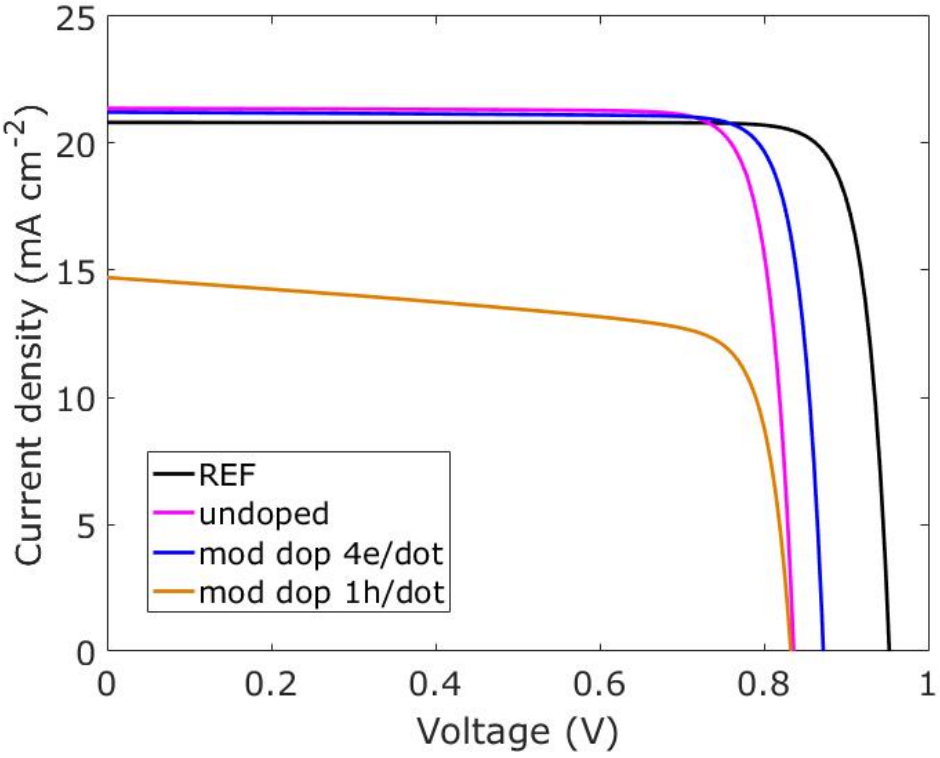


Fig. 3.2 JV curve of reference solar cell, undoped QD cell, n-type modulation doped QD cell with nominal density of 4 e/dot, p-type modulation doped QD cell with nominal density of 1 h/dot, under 1 sun AM1.5G illumination.

The n-type modulation doped cell ($\alpha = 4$ e/dot) achieves a $V_{oc}$ recovery about 20 mV with respect to undoped cell accompanied by a slight reduction of $J_{sc}$, whereas $\alpha = 1$ h/dot doping density causes a pronounced reduction of $J_{sc}$ and no recovery of $V_{oc}$. As discussed in Ref. [60], based on steady state and transient simulations, independent carrier dynamics (holes faster than electron owing to the closely spaced QD valence band states) and efficient barrier transport are prerequisites to prevent recombination loss across the QDs at open circuit and also allowing for high collection efficiency at short circuit condition. QD p-doping results in hole filling which impairs the fast hole dynamics and turns QDs into efficient traps yielding a substantial increase of QD capture and recombination loss. In fact, the accumulated holes in the QDs enhances the recombination of electrons photogenerated in the barrier and higher energy states through the GS (since they are rapidly relax into the GS). This leads to dramatic reduction in $J_{sc}$ and the main cause of $V_{oc}$ reduction at open circuit.

Restricting the analysis to the n-doping approach, it is worth to analyze how the cell behavior is affected by the per-dot doping density.

### 3.3.1 Effect of doping on photovoltaic conversion efficiency

An overall assessment of the cell photovoltaic performance dependence on doping profile and density is presented in figure 3.3 considering bulk SRH lifetimes of 500 ns and 10 ns representing high and low quality GaAs barrier respectively. The defective bulk cell shows significant improvement in terms of $V_{oc}$ owing to the shrinking of the depleted region and subsequent reduction of SRH recombination. This is a well-known benefit of base doping in defective bulk solar cells [61, 62]. In QDSCs, regardless of the quality of the host material, the undoped cells have similar $V_{oc}$ since at open circuit condition the limiting factor is GS radiative recombination which is the dominant loss process with respect to SRH recombination. In both ideal and defective QDSCs, the trends highlight the effectiveness of doping in terms of $V_{oc}$ recovery. Comparable $V_{oc}$ recovery is achieved by the different doping profiles with slight advantage of modulation doping which is more pronounced in defective cell since the dopants are placed in the barrier suppressing SRH recombination loss. While in the high-quality bulk material( $\tau_{\mathrm{SRH}} = 500$ ns ), $V_{oc}$ monotonically increases with the per-dot doping density, for the defective case( $\tau_{\mathrm{SRH}} = 10$ ns ) a slight dip of the $V_{oc}$ curve is observed at low doping levels ($\alpha = 1-2$ e/dot, corresponding to $1.2-2.4\times10^{16}\mathrm{cm}^{-3}$ in terms of equivalent background doping). The peculiar behavior of the QDSC at low doping levels arises from the modification of potential and carriers profiles across the cell which, whilst suppressing the radiative recombination through the QDs, enhance the SRH one across the neutral portion of the base. At high doping levels, the saturation of $V_{oc}$ recovery attained by the QDSCs, even in the case of ideal barrier material, suggests that the main limiting factor still is QD radiative recombination, due to the onset of significant recombination through the WL state. As discussed later, also on the basis of PL simulations, in the defective bulk cell ( $\tau = 10$ ns SRH ), the dominant recombination mechanism limiting $V_{oc}$ changes as the per-dot doping density increases: in the undoped or very low doping case( $\alpha < 1$ e/dot) the dominant recombination process is always radiative recombination through the GS while at $\alpha = 1-2$ e/dot, SRH recombination is the main one. At inter mediate doping levels ($\alpha = 3-8$ e/dot) SRH and QD radiative recombination contribute to a similar extent, and finally, at higher doping

levels ($\alpha > 8$ e/dot), QD recombination through the extended WL states turns to be the dominant recombination mechanism. Since the underlying mechanism is essentially a competition between different loss channels, the indicated values of the per-dot doping density for the onset of the different regimes of recombination, and the sensitivity to unintentional background doping as well, depend on the time constants characterizing the QD charge transfer processes, and thus on specific QD features such as size and shape. At the highest doping density the estimated recovery ranges between 70 and 90 mV depending on the crystal quality and doping method. The simulated trends are in good agreement with literature, where experimental data on $\delta$-doped cells range from a few mV in Ref. [15] up to 121 mV for the 8 e/dot modulation-doped cell in Ref. [49] (wherein simulations were also presented, showing an estimated recovery of about 15 mV for the 8 e/dot cell), and 105 mV for the 18 e/dot directly doped cell in Ref. [50].

Improvement in $V_{oc}$ is always accompanied by a reduction in $J_{sc}$. This is a common trend in all the investigated cells including the bulk cell. This reduction which is more pronounced in modulation doped cells is due to the reduction of the base drift region collection efficiency of carriers [49]. The amount of $J_{sc}$ reduction as the doping level increases is however strongly affected by the presence of QDs and by the specific doping profile.

$V_{oc}$ recovery and $J_{sc}$ degradation yield a trade-off in terms of achievable efficiency as a function of per-dot doping density. The maximum efficiency achieved at 4 e/dot doping density in the modulation doped cell and at 18 e/dot doping density in the directly doped cell with an absolute improvement with respect to the minimum observed efficiency (at $\alpha = 1$ - 2 e/dot) of 0.9% and 1.7% respectively.

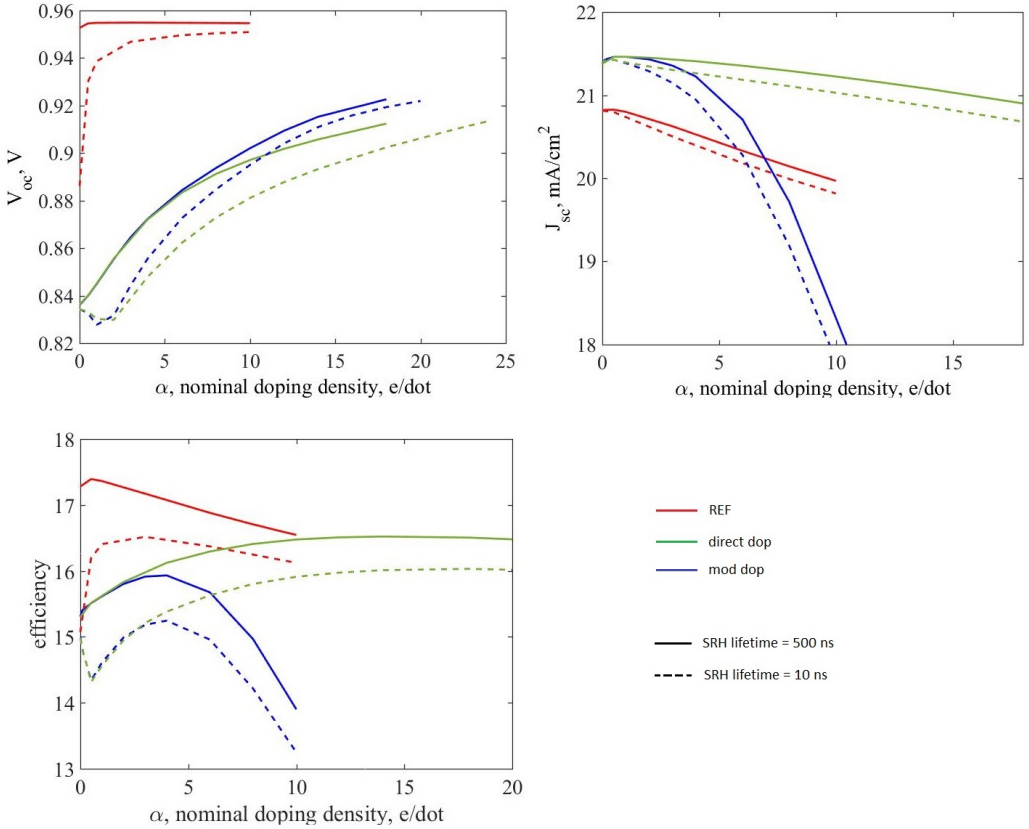


Fig. 3.3 Open circuit voltage, short circuit current density and efficiency as a function of the nominal per dot doping density for the n-type QDSCs exploiting modulation and direct doping, assuming high quality barrier ($\tau_{SRH}$ =500 ns, solid lines) and defective barrier ($\tau_{SRH}$ =10 ns, dashed lines), obtained under 1 sun AM1.5g illumination.

### 3.3.2 Analysis at short circuit

The observed $J_{sc}$ degradation is further substantiated by the EQE spectra reported in figure 3.4 showing how the reduction of photocurrent response in the above-gap region is affected by the doping method and nominal per-dot doping density. The saturating trend of the degradation in EQE at high doping densities (6 – 18 e/dot) in directly doped QDSCs is in good agreement with the experimental observations reported in [50] and the large diversion obtained for the modulation doping case is in qualitative agreement with Ref. [49]. It has to be noted that the reference cell, coherently with the $J_{sc}$ penalty observed in figure 3.3, shows a significant reduction in EQE between 600 and 800 nm (see figure 3.17 in Supplementary figures

section), causing a $J_{sc}$ penalty around 10% for 18 e/dot equivalent doping density. This suggests that the EQE degradation reported in Ref. [50] for the 18 e/dot bulk cell with respect to both undoped bulk and QD cells, could be largely attributed to the inherent behavior of the cell and marginally to the doping induced formation of defects. The general reduction between 600 and 800 nm in EQE indicates the increase of the recombination rate due to the degradation of carriers diffusion length due to the enhanced SRH recombination and QD radiative recombination rates.

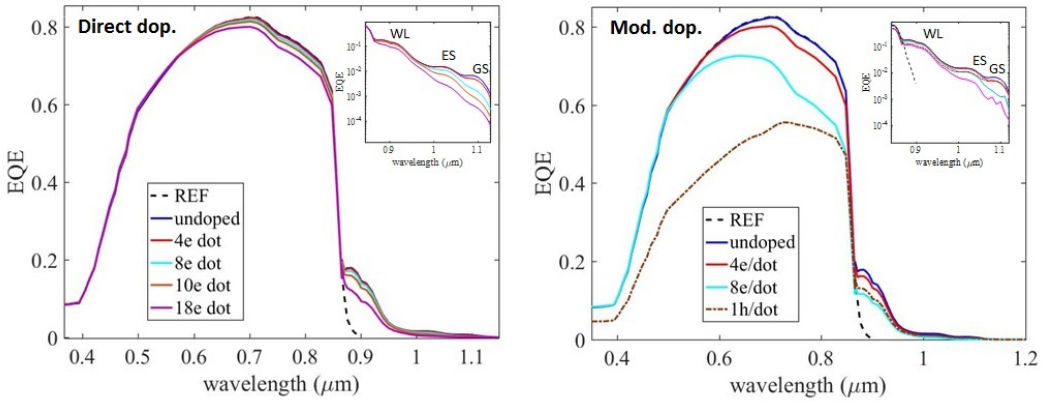


Fig. 3.4 External Quantum Efficiency (EQE) spectra for modulation and directly doped QDSCs. The inset in figures show a zoom of sub-bandgap region.

The reduction in the EQE at WL wavelength range is due to the decrease in the collection efficiency of minority carriers. The impact of doping on collection efficiency can be analyzed by comparing the band diagrams of undoped and doped QDSCs that are shown in figure 3.5. The energy banddiagram at short circuit of an undoped cell is characterized by high and almost constant electric field which helps the photogenerated carriers to be swept out of the base region and collected by their respective contacts resulting in high collection probability. On the contrary, the band diagram of a doped QDSC is characterized by two regions; one with large band bending towards the p emitter (in the case of n doped cells) corresponding to the depletion region and one with low electric field and flat bands in which the transport of the photogenerated carriers from the base into the contacts is less effective with respect to the undoped cell.

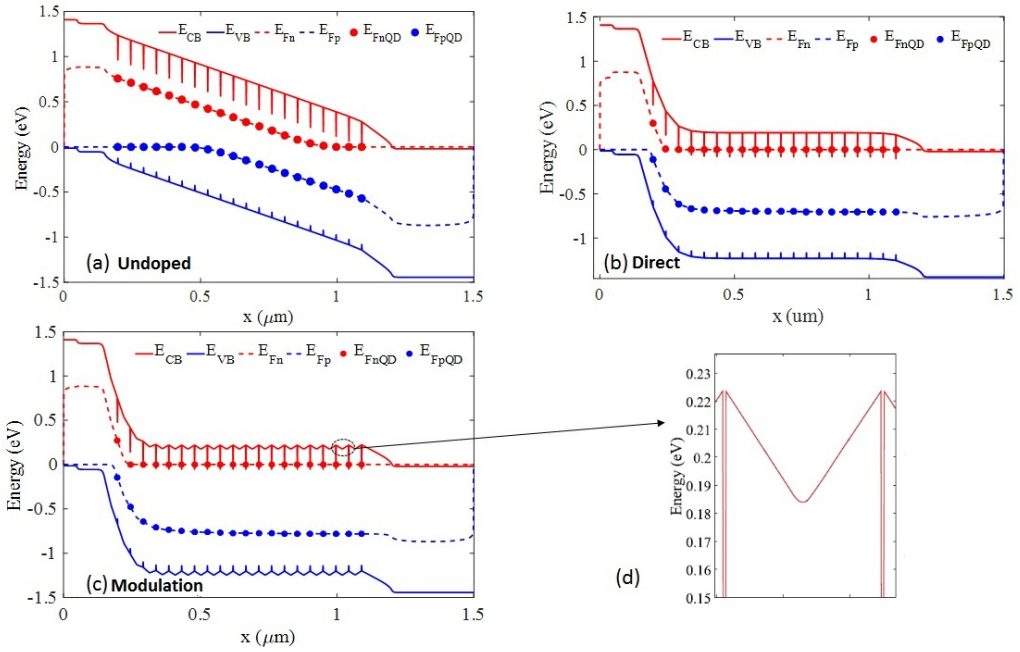


Fig. 3.5 Energy band diagram at short-circuit condition for the undoped (a), 4 e/dot directly doped (b) and the 4 e/dot modulation doped cell (c). Zoom of interdot layer of 4 e/dot modulation doped cell

At longer wavelength (correspond to GS and ES) the reduction in EQE is attributed to the state filling and subsequent suppression of optical transitions. The corresponding occupation probabilities of the states are shown in figure 3.6. It is worth noticing that the actual QD filling depends on the interplay between drift-diffusion of free carriers in the bulk and net capture rate in the QDs and is therefore generally found to be non-uniform across the QD layers and different from the nominal per-dot doping density. N-type doping increases the electron filling of all the QD layers. Hole filling decreases in the QD layers next to the junction while it increases by about two orders of magnitude in the QD layers placed in the flat band region.

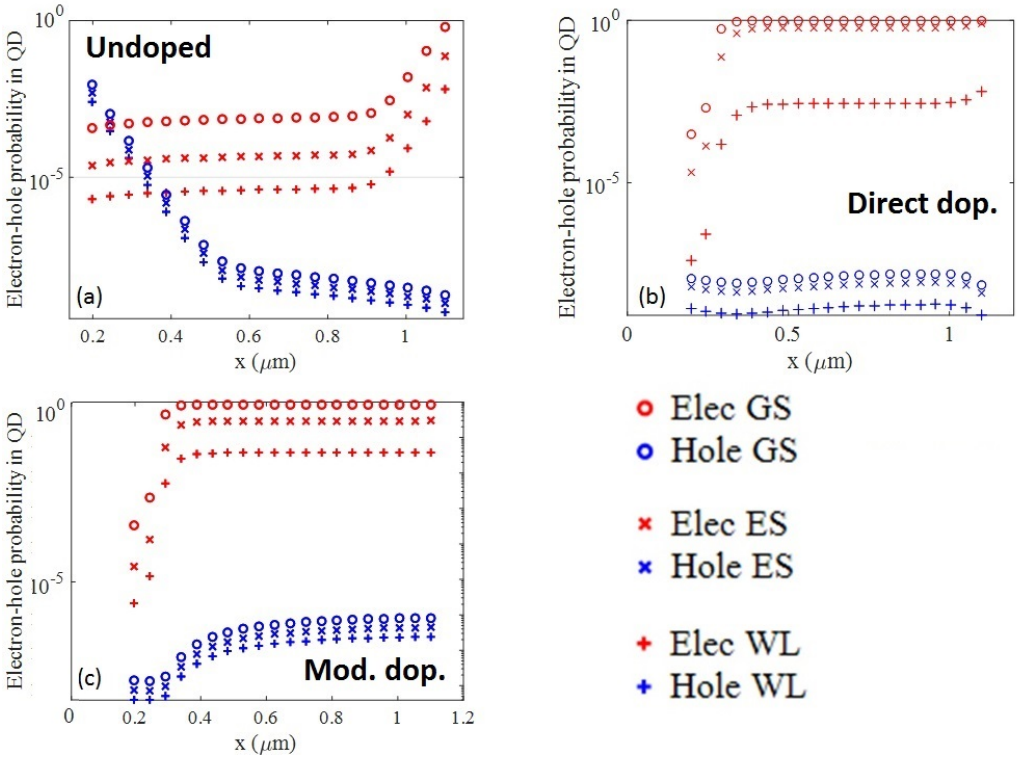


Fig. 3.6 Occupation probability of electrons (red) and holes (blue) in the QD states across the base at short-circuit for the undoped cell (a), the 4 e/dot directly doped cell (b) and the 4 e/dot modulation doped cell (c).

The increment of QD electron and hole density in the flat-band region also enhances radiative recombination rate that become competitive against the carrier escape rate out of the QDs as a consequence of the QD state occupation distribution. Figure 3.7 shows the corresponding spatial distribution of photogeneration, net escape rate ($R_{ESC}$-$R_{CAP}$) from the WL to the bulk, and recombination paths through the QD and bulk states. Positive net escape indicates that the QD carriers are extracted out of the QD layer, negative escape rate indicates that the QDs act as capture (or trap) centers. The comparison against the undoped cell points out that in the doped cell QD layers placed in the flat band region poorly contribute to the short circuit current, since net escape rate is much smaller than QD photogeneration. Also, due to the modification of free carriers and electric field, the SRH recombination profile tends to peak towards the n contact. Finally, the QD photogeneration and radiative recombination almost equilibrate each other, yielding the decrease in the subband photocurrent contribution seen in figure 3.4. Regardless of SRH recombination lifetime, further increase in doping density turns the QDs into effective recombination

centers for photogenerated carriers in the barrier regions and causes the radiative recombination through the QDs in the flat band region to become the dominant mechanism leading to a dramatic reduction in $J_{sc}$ current that has observed in figure 3.3 at high doping levels.

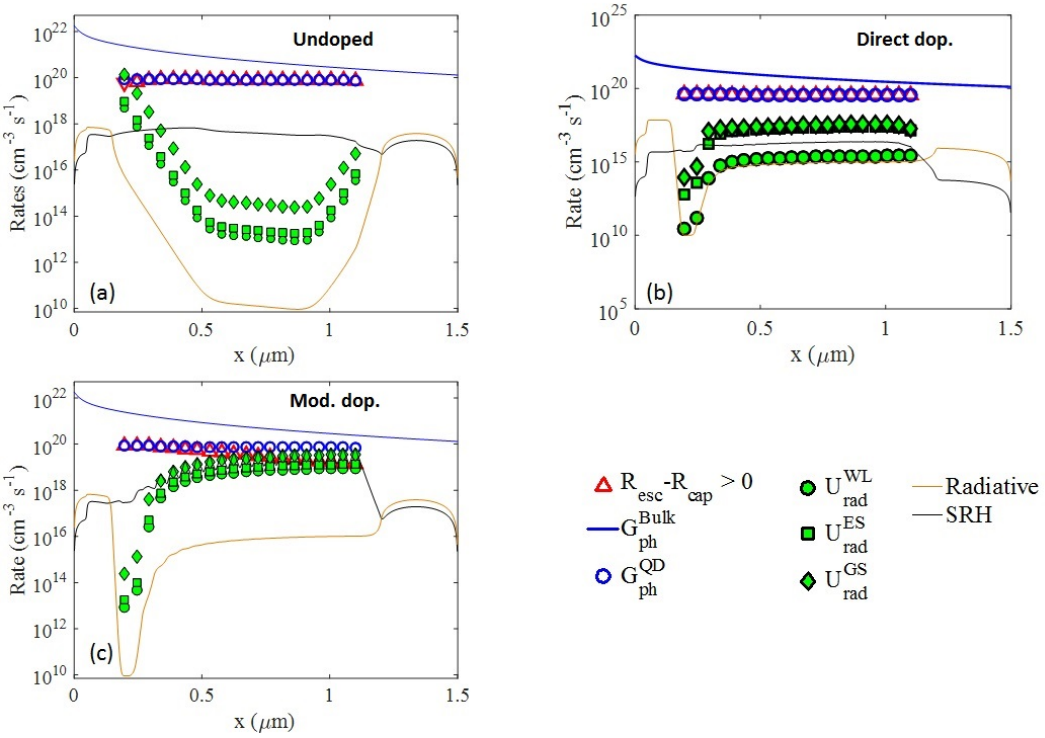


Fig. 3.7 Spatial distribution of photogeneration, net escape, and recombination rates at short-circuit for the undoped cell (a), the 4 e/dot directly doped (b) and the 4 e/dot modulation doped (c) cell. The equivalent volume rates for QD states are computed by normalizing the corresponding surface rates by the QD layer interspacing (47 nm).

The sensitivity of the $J_{sc}$ penalty with respect to doping method is the result of modulation of the potential within the inter-dot barrier regions. In the modulation doped QDSCs, the periodic potential barriers accross the base are due to the transfer of carriers from the $\delta$-doped regions in to the QDs [63] creating depletion regions that induce formation of barriers at QD side walls (see figure 3.5 (d)). These potential barriers limit the electron capture and at the same time promote hole capture into the QDs. In addition, they hinder the transport of the photogenerated carriers towards their respective contacts.

PL measurements at short-circuit can be used to quantify the overall impact of

carrier loss through the QD recombination channels [15]. The enhancement of QD recombination at high doping levels is revealed by the dependence of the short circuit integrated PL intensity on doping density, as shown in figure 3.8. The GaAs barrier is excited by a monochromatic light at 532 nm with excitation intensity of 1.1 $\mathrm{Wcm}^{-2}$. Sub-band gap integrated PL spectra is shown in figure 3.8.

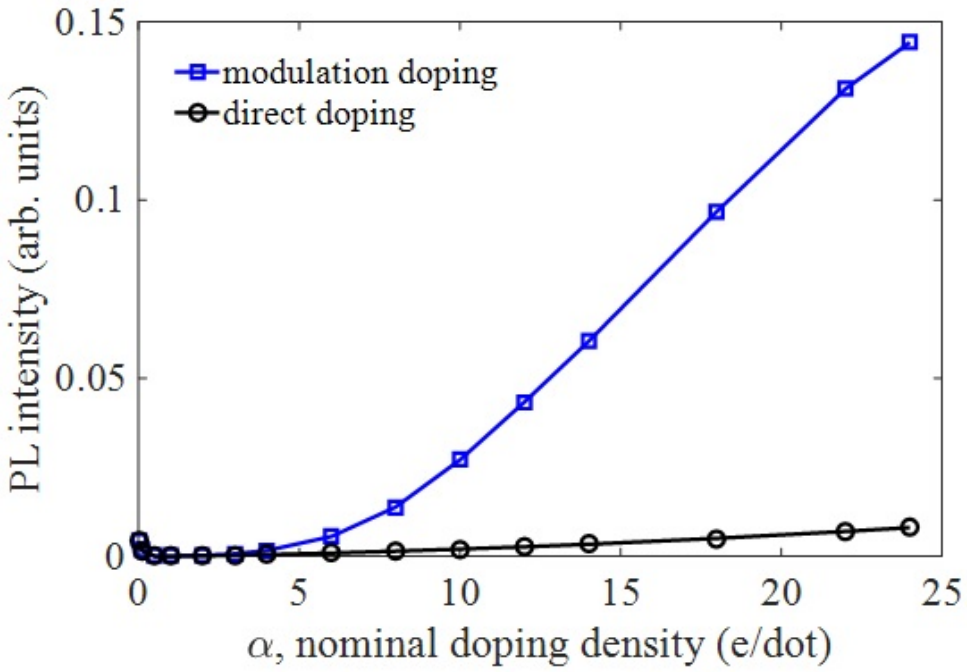


Fig. 3.8 Integrated PL intensity at short circuit condition as a function of the nominal per dot density for the directly and modulation doped QDSC.

At low doping levels, $\alpha < 5$, the PL is slightly quenched due to the dominant SRH recombination in the neutral base, as previously discussed. At higher doping levels, a large enhancement is observed for the modulation doping, whereas this enhancement remains quite limited for the direct doping case. Limited luminescence by the QDs is desired to preserve $J_{sc}$ when illuminating the device with above gap wavelength meaning that the photogenerated carriers in the barrier are collected efficiently without capturing into the QDs. This is true for undoped and directly doped QDSCs. The valence band wells arising in the modulation doped cells promotes the accumulation of holes in the QDs reducing carrier escape towards the barrier and increasing the recombination through the QDs. While for the directly doped cells, thanks to the confinement of the doping in the QDs, the bands are not

affected significantly and holes remain delocalized across the barrier. This can be demonstrated by comparing the hole filling for the two doping method (as shown in figure 3.6).

### 3.3.3 Analysis at open circuit

Looking at the open circuit spatial distribution of recombination and capture rates in figure 3.9, in both doped and undoped QDSCs, the QDs are acting as effective capture centers ($R_{\mathrm{ESC}} - R_{\mathrm{CAP}} < 0$). In undoped QDSCs the recombination is dominated by radiative recombination through the GS, except for the QD layer next to the n-contact, wherein the peak of the electrical field maximizes the SRH bulk recombination. The displacement of the junction towards the n contact is due to the large asymmetry between QD electron and hole dynamics. Under forward bias condition large amount of electrons are captured by the QDs but holes have fast dynamics due to their closely spaced energy levels and are delocalized in the barrier. Thus, the barrier is rich of free holes and the junction is displaced towards the n-contact. In modulation doped cells, the recombination through the GS is suppressed while the bulk SRH recombination increased and became comparable with QD radiative recombination. Both mechanisms limit the open circuit voltage at the same extend. The 4 e/dot directly doped cell is shown in the figure for the sake of comparison. In order to achieve more visible change in spatial distribution of recombination in direct doped cells, higher doping density is required (maximum achieved for 18 e/dot).

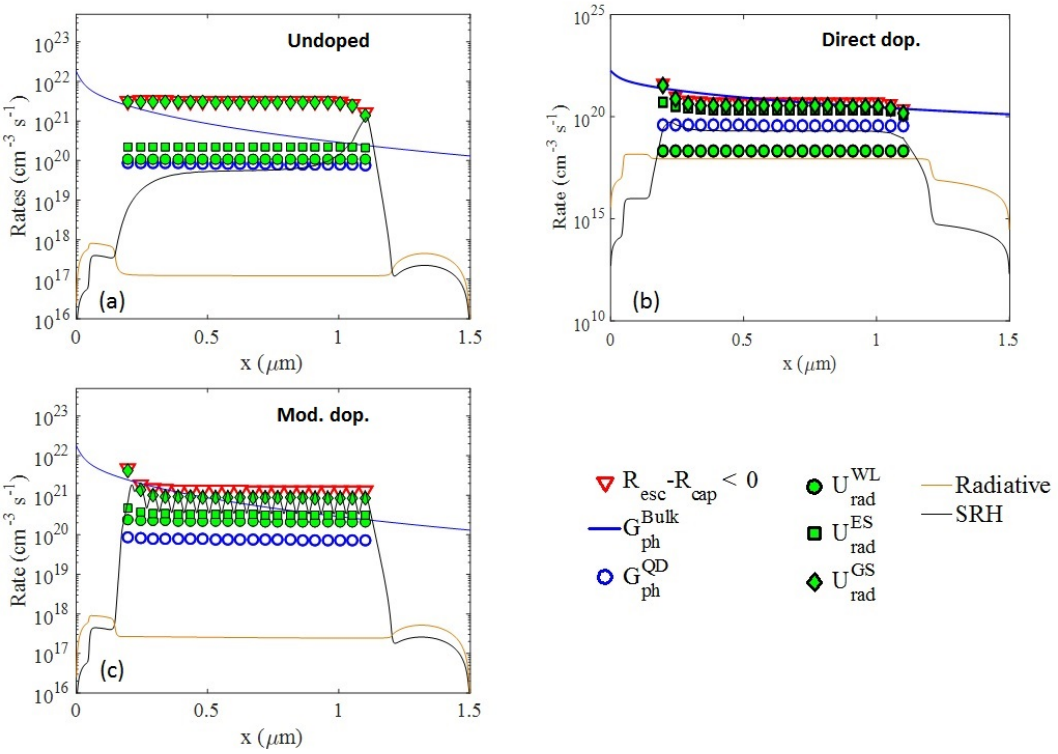


Fig. 3.9 Spatial distribution of photogeneration, net escape, and recombination rates at open circuit for the undoped cell(a) the 4 e/dot directly doped cell (b) and the 4 e/dot modulation doped cell (c). The equivalent volume rates for QD states are computed by normalizing the corresponding surface rates by the QD layer interspacing (47 nm).

Since near $V_{oc}$ cells operate close to the flat-band condition, the behavior of the integrated recombination rates provides a straightforward mean to assess the loss mechanisms of injected carriers. Integrating the recombination rates across the base and analyzing the evolution of recombination current with respect to voltage allows us to have better insight in the influence of doping on $V_{oc}$ recovery. Figure 3.10 shows QD radiative and SRH recombination currents with respect to voltage from maximum power point up to $V_{oc}$. Note that here the per dot doping for each doping method corresponds to the doping level that allows for maximum achievable efficiency that is 18 e/dot for direct doping and 4 e/dot for modulation doping.

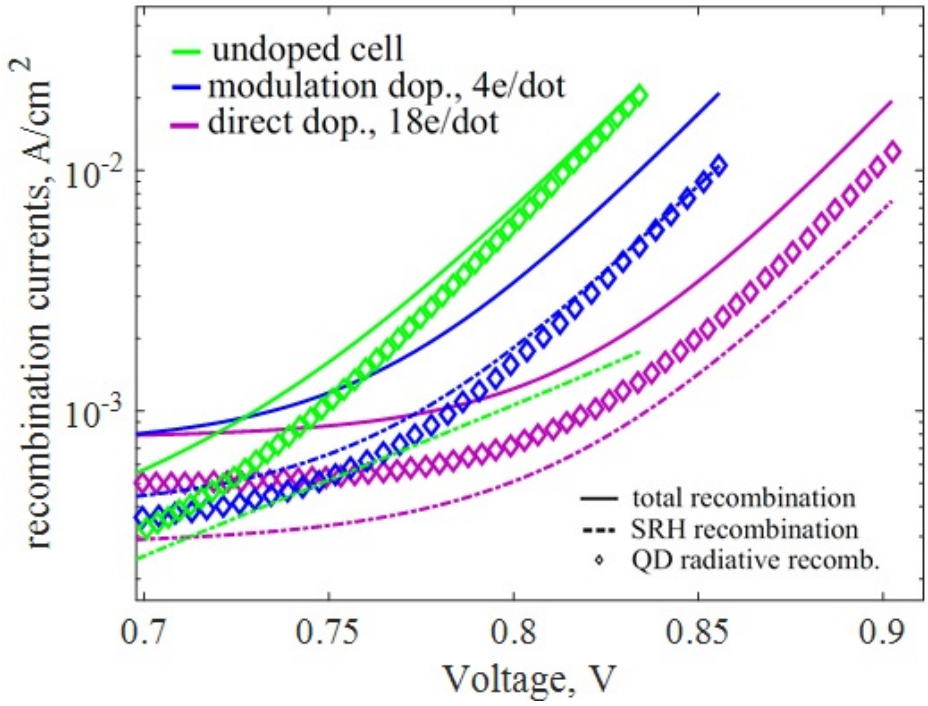


Fig. 3.10 Voltage dependence of the integrated recombination rates across the base region for the undoped, 4 e/dot modulation doped, and 18 e/dot directly doped cell: symbols are the recombination in the QD layers, $U_{\mathrm{rad}}$, QD, dashed lines indicate the SRH recombination in the barrier, $U_{\mathrm{SRH}}$, and solid lines the total recombination rate. The voltage sweeps up to the $V_{oc}$ of each cell, i.e. about 0.83 V, 0.85 V and 0.9 V for undoped, modulation doped and directly doped cell respectively.

In the undoped cell $V_{oc}$ is limited at around 0.83 V and at open circuit, the total recombination current is dominated by QD radiative recombination. The dominance of QD radiative recombination across the neutral part of the base shows up with an almost unitary ideality factor of the total recombination current, whereas the small SRH recombination contribution, being confined to the depleted region, is characterized by a larger ideality factor. At 0.83 V, the doped cells show lower QD radiative recombination which allow them to attain higher $V_{oc}$. The modulation doped cell shows suppressed QD recombination, thus a higher $V_{oc}$ is attained. The $V_{oc}$ achieves the value of 0.85 V and is limited by both SRH and QD radiative recombination. Due to the flat SRH profile across the base observed in figure 3.9, also the SRH equivalent recombination current increases with an almost unitary ideality factor. In the case of directly doped cell, 70 mV $V_{oc}$ recovery is calculated due to the higher doping density, at voltage values corresponding to the $V_{oc}$ of the undoped and modulation doped cells,

the directly doped cell shows greatly suppressed radiative and SRH recombination. Radiative recombination is blocked by the GS carrier filling, while SRH recombination is kept small because of the slight barrier potential profile modification. In the directly doped cell, $V_{oc}$ is limited by QD radiative recombination through the WL.

To complete the analysis, dark current voltage characteristics of the doped and undoped cells are presented in figure 3.11 along with the one of ideal bulk and ideal QDSC for the sake of comparison. The ideality factor extracted from the dark current-voltage characteristic is a signature to evaluate the dominant recombination mechanism of a cell. The ideality factors of ideal cell and defective cell at low bias range (V < 0.6 V) make evident the impact of SRH on the dark current characteristic. At low voltage the ideality factor of almost 2 can be extracted from the cells that suffer from SRH recombination. At higher voltages near $V_{oc}$, QDs act as effective traps and the recombination through the dots becomes dominant yielding ideality factor near 1 due to the dominance of radiative recombination over non radiative one. Moreover, the dark current of doped cells is lower with respect to the undoped since doping suppresses the radiative recombination through the confined states.

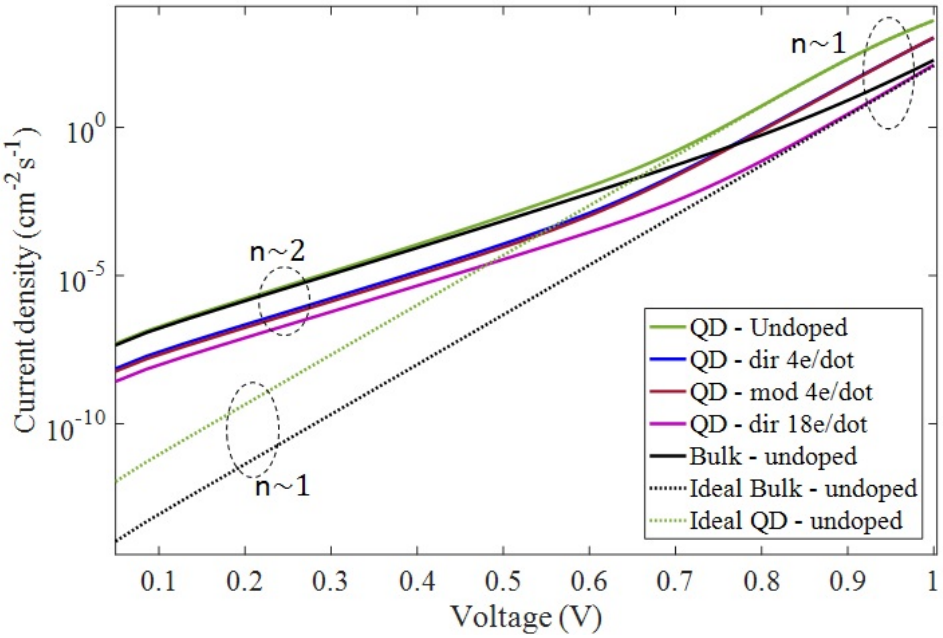


Fig. 3.11 Dark J-V characteristic of undoped Bulk and QDSCs considering both ideal and defective and doped QDSC with SRH lifetime of 50 ns.

Integrated PL is also calculated as a function of per-dot doping density for modulation and directly doped QDSCs considering three possible scenarios in terms of barrier material quality that is modeled by assuming SRH lifetimes of 500 ns, 10 ns and 1 ns. Besides the overall subband gap integrated PL intensity, the contribution of GS and ES (excluding WL) is also singled out. The trend of the results are similar for two doping method and the trends is shown to be dependent on SRH recombination lifetime since the introduction of doping not only changes the amount of radiative recombination but also changes the balance between SRH and radiative loss.

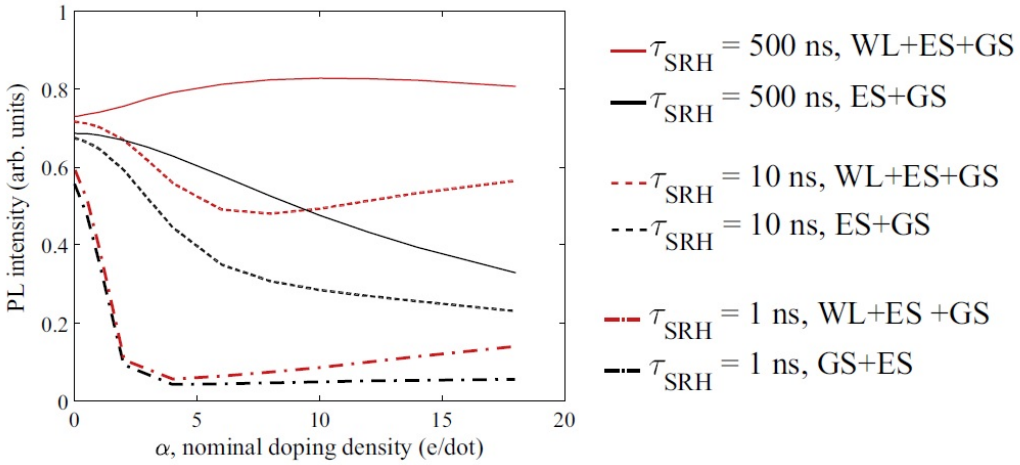


Fig. 3.12 Integrated PL intensity at open circuit condition as a function of the nominal per dot doping density for the direct doping strategy, considering various SRH lifetimes

For high quality material ($\tau_{SRH} = 500$ ns), the overall IPL intensity versus doping level reaches a maximum and then slightly decreases. The IPL of GS and ES is quenched as the doping level increases due to the blocking of electron capture in to these states. The maximum of overall IPL is therefore the result of significant radiative recombination through the WL state. In another words, for high quality bulk material the achievable photovoltage will be determined by carrier capture and recombination rate through the WL. For shorter bulk SRH lifetime ($\tau_{SRH}$ = 10 ns), the overall IPL with respect to doping density is quenched to a minimum value for $\alpha$ =8 e/dot and then increases owing to the onset of WL emission. PL quenching at intermediate doping level is the result of SRH recombination dominance over QDs capture and radiative processes and as the doping level increases the WL radiative recombination becomes the dominant process over the rest of the loss mechanism.

Thus, WL recombination might remain an important cause of $V_{oc}$ degradation even in cells with significant SRH recombination. Finally, in the case of highly defective material ($\tau_{SRH}$ = 1 ns), the IPL minimum is displaced at lower doping levels ($\alpha$ =2-3 e/ dot) and the intensity is attenuated of about one order of magnitude with respect to the undoped cells, indicating a strong prevalence of SRH recombination. These low values of alpha is correlated to an unintentional background doping of about $10^{16}$cm$^{-3}$ suggesting that the background doping of interdot layers must be carefully considered when interpreting the PL measurements since it may significantly impact the recombination mechanisms.
Summarizing, the impact of doping on open circuit voltage recovery in devices that suffer from non-radiative recombination can be addressed for three ranges of doping levels. for undoped cells, the $V_{oc}$ is limited by the radiative recombination through the GS, at intermediate doping levels SRH recombination loss dominates over QD radiative recombination and finally at high doping levels, radiative recombination loss through the WL state limits the $V_{oc}$.

The interplay between the SRH and QD radiative recombination causes significant non linear behavior of IPL with respect to excitation power density. In figure 3.13) (a) the behavior of IPL with respect to per-dot doping density is shown for a directly doped QDSC excited with different excitation power density, considering $\tau_{SRH}$ = 10 ns and $\tau_{SRH}$ = 1 ns. By decreasing the PL excitation from 1.1 Wcm$^{-2}$ down to 0.1 Wcm$^{-2}$, the IPL quenching at low doping levels becomes more pronounced and so is the subsequent increase of the IPL with doping due to the emission from the WL states. The suppression of GS and ES emission and the concomitant enhancement of WL emission as doping density increases is highlighted in the PL spectra in figure 3.13) (b)–(c). In the highly defective case ($\tau_{SRH}$ = 1 ns), the IPL minimum shifts at doping density as low as $\alpha$=1 e/dot and then the IPL increases of about nine times when $\alpha$=18 e/dot. The observed behavior is in agreement with the PL measurements reported in Ref. [50], assuming a non negligible background doping in the undoped cell, and provides theoretical support to the interpretation of the PL enhancement in the doped cells as the result of reduced capture and thermal decoupling between wetting layer and QD at high doping levels.

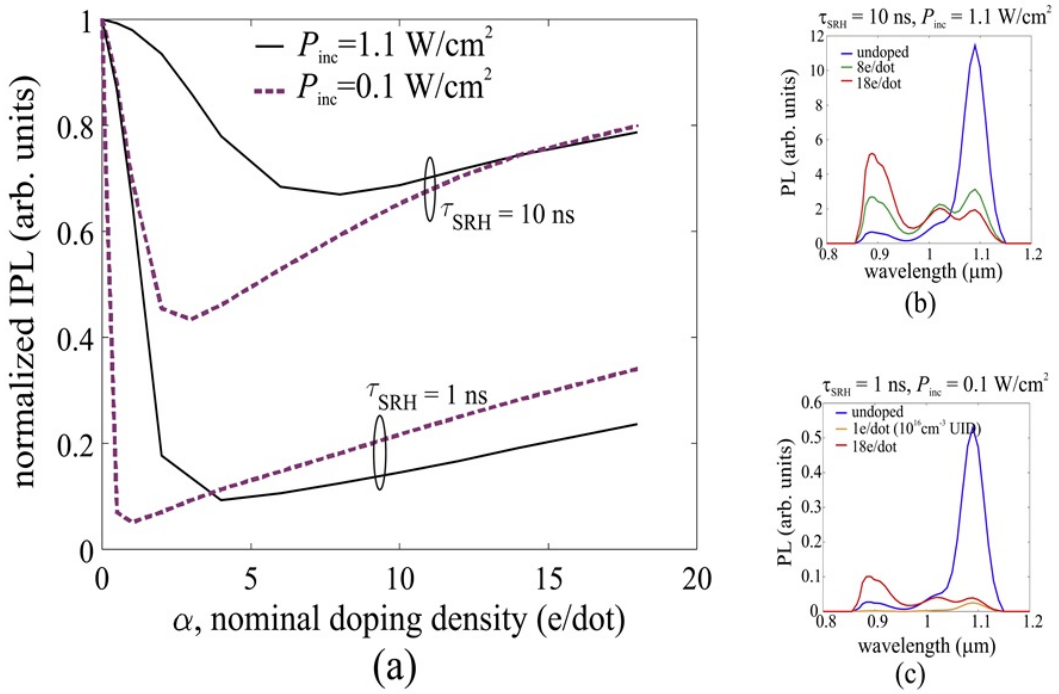


Fig. 3.13 (a) Normalized integrated PL intensity as a function of the nominal per-dot doping density for the directly doped cell with $\tau_{SRH}$ of 10 ns and 1 ns, under two different excitation intensities. (b) PL spectra at P = 1.1 W/cm for the undoped, 8 e/dot (corresponding to the minimum IPL), and 18 e/dot when $\tau_{\mathrm{SRH}}$= 10 ns. (c) PL spectra at P = 0.1 W/cm for the undoped, 1 e/dot (corresponding to the minimum IPL), and 18 e/dot when $\tau_{\mathrm{SRH}}$= 1 ns. As discussed in the main text, the 1 e/dot case may also be considered representative of a cell with background unintentional doping (UID) of about $10^{16}\mathrm{cm}^{-3}$.

The dependence of IPL intensity on excitation power density for the undoped ,1 e/dot and 18e/dot directly doped cells is reported in figure 3.14. For radiatively limited cells a linear behavior of the IPL intensity versus excitation and almost coincident IPL values, regardless of the doping level density can be obtained. In the defective bulk cases, the undoped and 18 e/dot cell, dominated by QD radiative recombination, show a linear behavior of the IPL with excitation intensity (i.e. unitary slope in both the log-log plots in figure 3.14). In contrast, the 1 e/dot cell, dominated by SRH recombination, shows a super linear behavior (i.e. a slope of about 1.8 in the log-log plot) across the whole range of excitation power when $\tau_{\mathrm{SRH}} = 1$ ns (figure 3.14 (b)), and a change of behavior, from slightly superlinear at low excitation (slope of about 1.2) to linear at higher excitation, when $\tau_{\mathrm{SRH}} = 10$ ns (figure 3.14 (a)). Similar results were reported for directly doped QDs in [52]. The change in excitation power dependence was explained by the effectiveness of QD doping in

inactivating non-radiative recombination. For modulation doped QDs with dot in a well structure superlinear excitation dependence of PL intensity was observed in undoped QDs, where as doped QDs showed an almost linear behavior in Ref. [64]. The change in excitation power dependence was attributed to a change in the dynamics of electrons and holes in QDs (from uncorrelated dynamics in the undoped QDs to correlated dynamics in the doped QDs) due to enhanced Coulomb attraction induced by the excess carriers in the dots. In Ref. [65], by studying undoped QDs confined in an AlAs/GaAs superlattice which inhibited transport of carriers in the barrier, it was already suggested that independent e-h dynamics is at the root of the onset of superlinear dependence on excitation power. It is worth noticing that our model indeed assumes independent e-h dynamics in the dots but, according to the results, the space charge and barrier transport are the factors that ultimately correlate the e-h pair dynamics. According to our simulations, the superlinearity is actually triggered by the presence of defects which affect the diffusion across the barrier [66], at least as long as barrier transport exists. Thus, the change from superlinear to linear dependence of the IPL intensity on excitation power density induced by selective doping can be interpreted as a signature of suppressed non-radiative recombination.

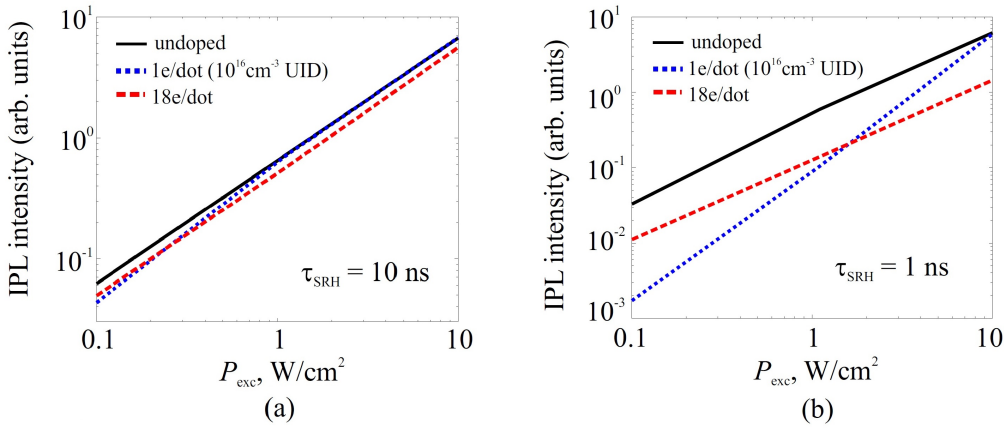


Fig. 3.14 Integrated PL intensity as a function of the excitation power density for undoped and directly doped cells with barrier SRH lifetime of 10 ns (a) and 1 ns (b).

## 3.4 Validation against experimental results

In this section we consider a real-case study and apply the analysis of the interplay between doping and recombination processes on QDSCs, providing experimental-

based validation to the previous section in order to show the valuable insight that can be achieved through device level simulation. The results of the study is published in [67]. In the simulation only thermal escape is considered since the optical escape is negligible in InAs/GaAs QDs [38] and under such an efficient thermal escape the field assisted mechanism also does not provide any significant change in terms of cell overall behavior.

The sample under investigation is InAs/GaAs QDSC that was grown by solid-source molecular beam epitaxy (MBE) on $n^+$ GaAs (100) substrate. The cell consists of a 200 nm GaAs buffer layer with Si doping density of $1 \times 10^{18}$ cm$^{-3}$, 30 nm $Al_{0.35}Ga_{0.65}As$ back surface field (BSF) with Si doping density of $1 \times 10^{18}$ cm$^{-3}$, 1000 nm GaAs base with Si doping density of $1 \times 10^{17}$ cm$^{-3}$, 250 nm GaAs emitter with Be doping density of $2 \times 10^{18}$ cm$^{-3}$, 100 nm GaAs emitter with Be doping density of $5 \times 10^{18}$ cm$^{-3}$, 30 nm $Al_{0.75}Ga_{0.25}As$ window layer with Be doping density of $2 \times 10^{18}$ cm$^{-3}$, and 50 nm GaAs contact layer with Be doping density of $1 \times 10^{19}$ cm$^{-3}$. The intrinsic region of the cells consists of 20 stacks of 2.1 monolayer (ML) InAs QDs. The Si-doped QDSC underwent direct Si doping with 14 e/dot doping density. The geometrical structure is shown in figure 3.15.

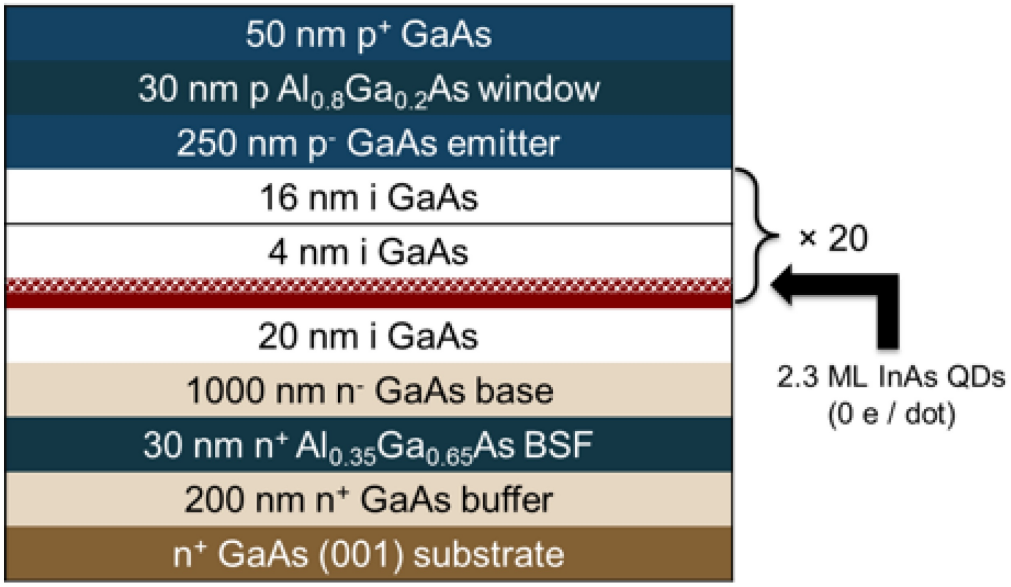


Fig. 3.15 Sketch of the epilayer of the 20 x QD solar cell.

At open circuit condition, as a first step, the predicted $V_{oc}$ penalty of the QDSC with respect to the bulk cell is analyzed by considering possible fluctuation of GS

energy level that was observed in measured PL spectra [67]. Figure 3.16 shows the $V_{oc}$ of the QDSC as a function of per dot doping density for different QD families with GS transition energy from 1.18 to 1.25 eV. The analysis show that the inherent $V_{oc}$ penalty due to the inclusion of the QDs is about 120 mV for the largest GS confinement in agreement with theoretical work [38] and experimental data of QDSC with the record $V_{oc}$ [14]. The penalty is fully due to radiative recombination through the QD states. The comparison with experimental data suggests that other loss mechanism is affecting the $V_{oc}$ leading to added penalty of 180 meV for the undoped cell. Very good agreement is obtained by introducing significant defectivity of the interdot layers. It is worth noticing that at short circuit, SRH recombination is more detrimental in doped regions that marginally affect carrier collection efficiency while at open circuit condition, the most detrimental loss comes from SRH recombination in the undoped region where the QDs are placed. The experimental data on a similar structure reported by Lam et al. [50] is also shown in the figure. The calculated trend of $V_{oc}$ as a function of doping density closely follows the measured one, suggesting that dopant atoms are well incorporated in the QDs and provide electrons per dot in line with the nominal doping value. Overall, the results highlight that doping is always beneficial in terms of $V_{oc}$, since it mitigates both QD radiative and non-radiative recombination. QD radiative recombination is in fact suppressed by QD state filling and SRH recombination is suppressed because doping shifts the electron quasi-Fermi level far away from the intrinsic Fermi level and reduces the capture/emission probability of electrons by the midgap defects.

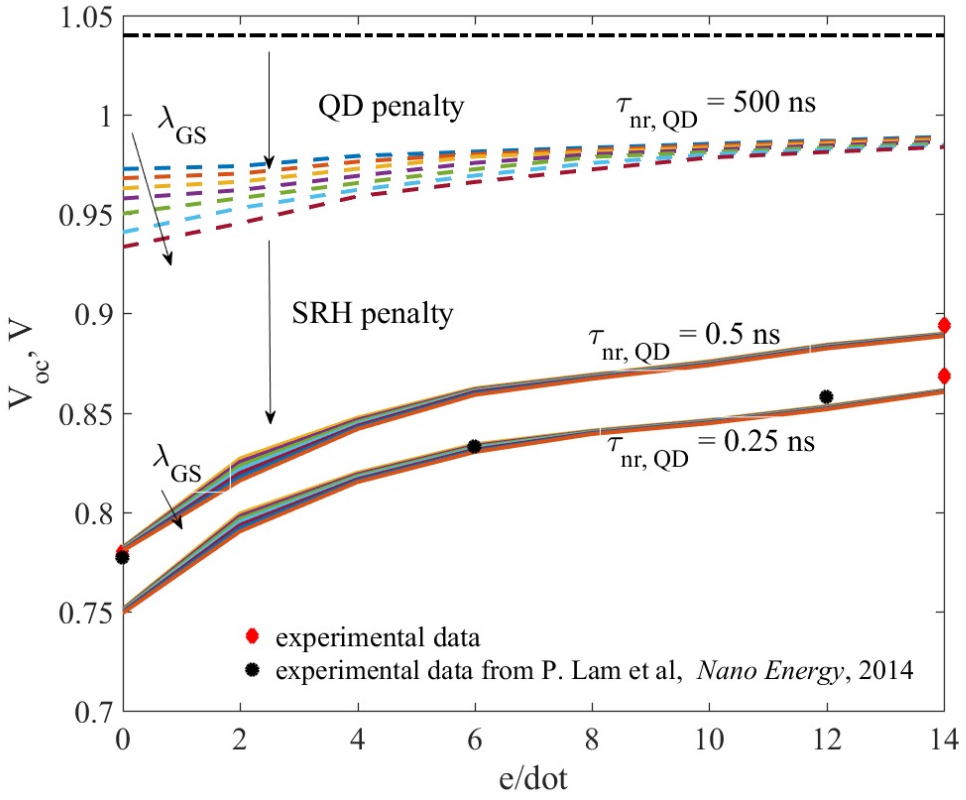


Fig. 3.16 Analysis of $V_{oc}$ penalty in QDSC as a function of the per dot doping density, for different GS energy confinement ($\lambda_{GS}$ ranges from 990 nm to 1050 nm) and different minority carrier lifetime in the interdot layers ($\tau_{nr,QD}$). The black dash-dot line indicates the $V_{oc}$ of the reference bulk GaAs cell.

## 3.5 Supplementary figures

Figures summarizing the results of the numerical simulation discussed in this chapter for bulk reference cell, undoped QDSC, directly doped QDSC and modulation doped QDSC. SRH lifetime is set to 10 ns. For each doping strategy, the doping levels are those corresponding to the maximum achievable cell efficiency.

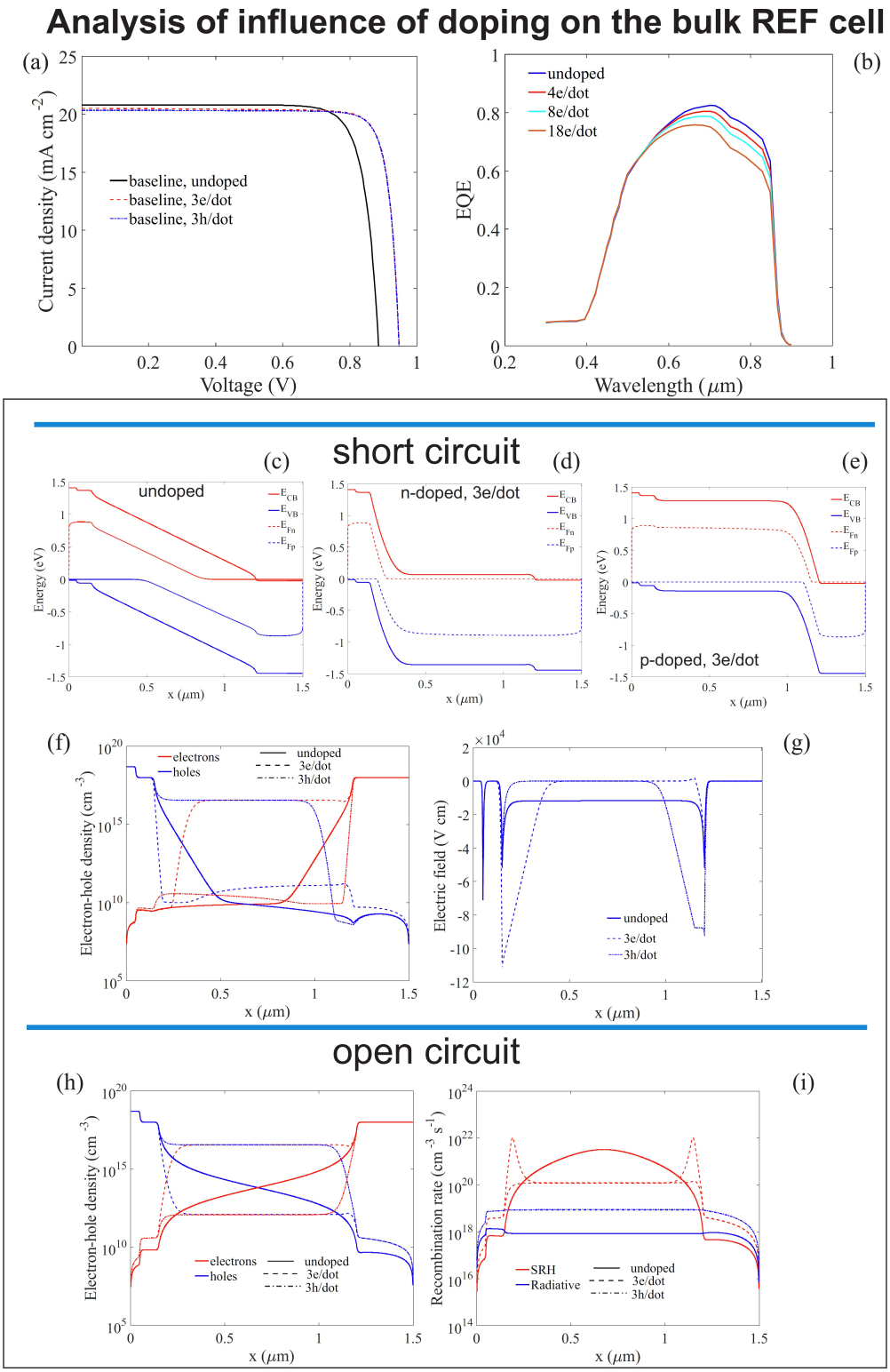


Fig. 3.17 (a) J-V for undoped, n-doped and p-doped base. The quoted 3 e(h)/dot doping density means a uniform doping level of $3.6 \times 10^{16}$cm$^{-3}$; (b) EQE for different levels of n-type doping. (c)-(e) Band diagram at short circuit for the undoped, n-doped and p-doped base. (f) Free carriers density and (g) electric field profile at short circuit. (h) Free carriers density and (i) recombination rates distribution at open circuit condition.

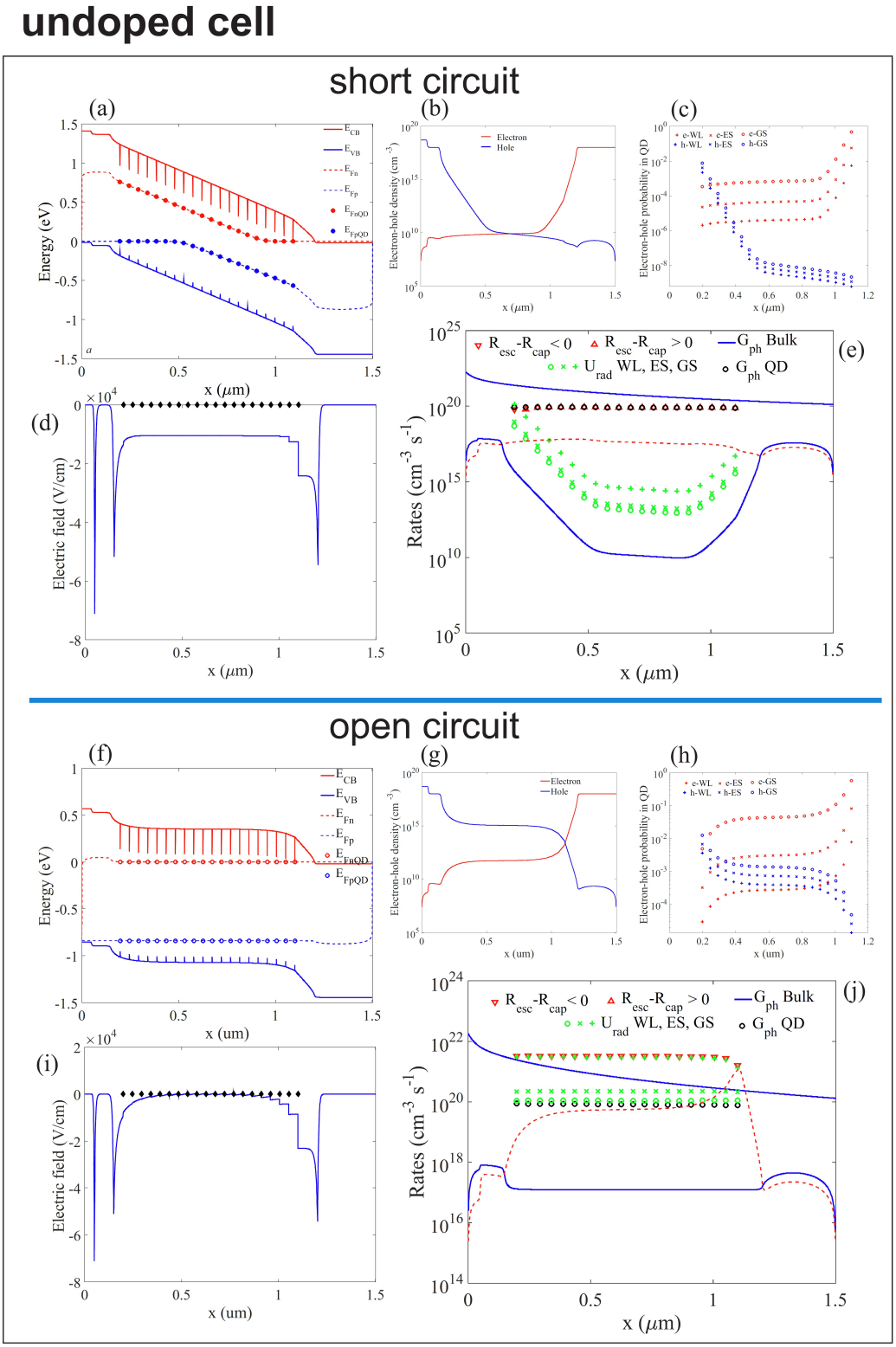


Fig. 3.18 Spatial distribution at short circuit condition of energy bands (a), free carriers density (b), QD occupation probability (c), electric field (d), recombination rates (e). Spatial distribution at open circuit condition of energy bands (f), free carriers density (g), QD occupation probability (h), electric field (i), recombination rates (j). Diamond symbols in the electric field figures (d) and (i) indicate the QD layers position.

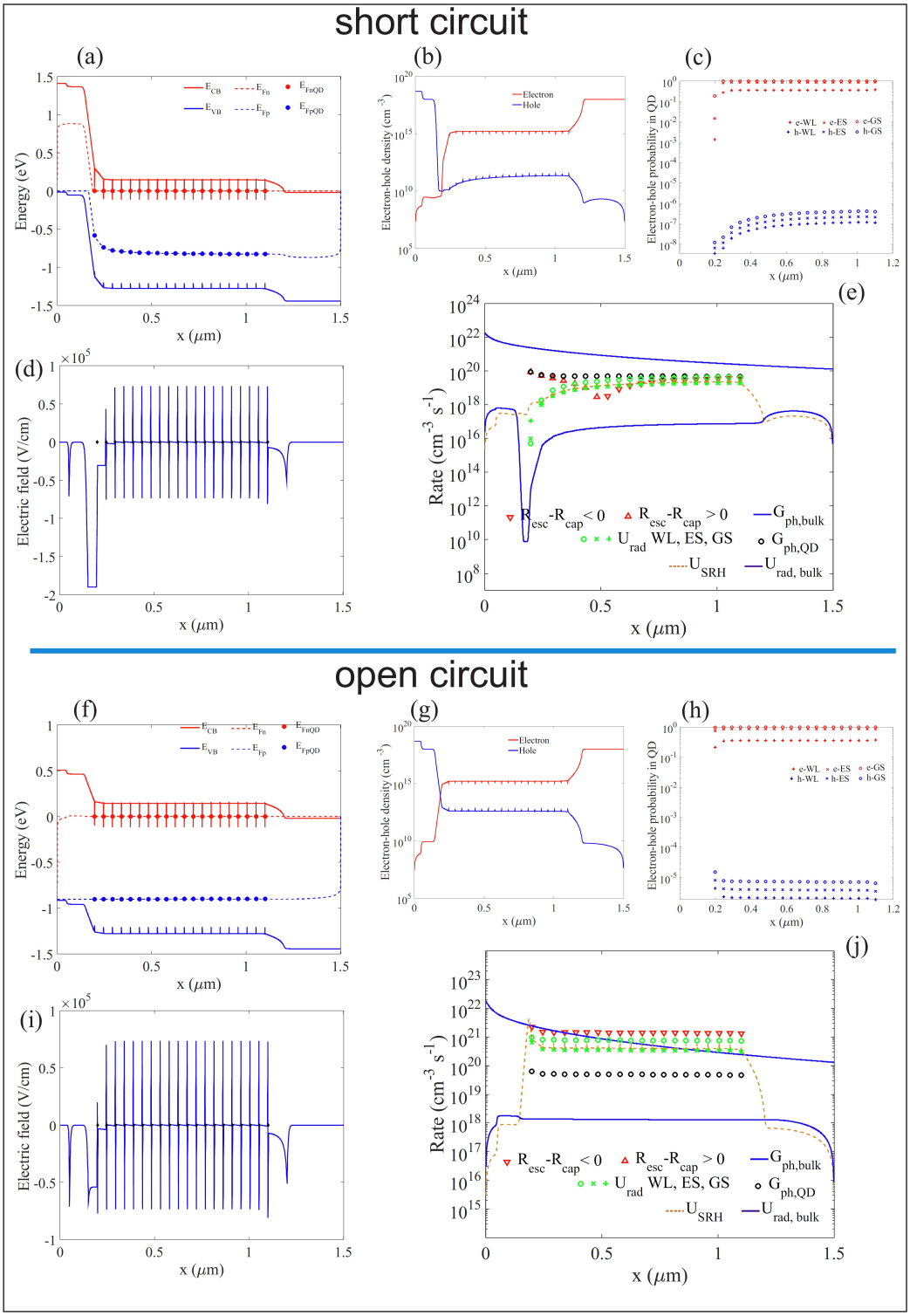


Fig. 3.19 Spatial distribution at short circuit condition of energy bands (a), free carriers density (b), QD occupation probability (c), electric field (d), recombination rates (e). Spatial distribution at open circuit condition of energy bands (f), free carriers density (g), QD occupation probability (h), electric field (i), recombination rates (j). Diamond symbols in the electric field figures (d) and (i) indicate the QD layers position.

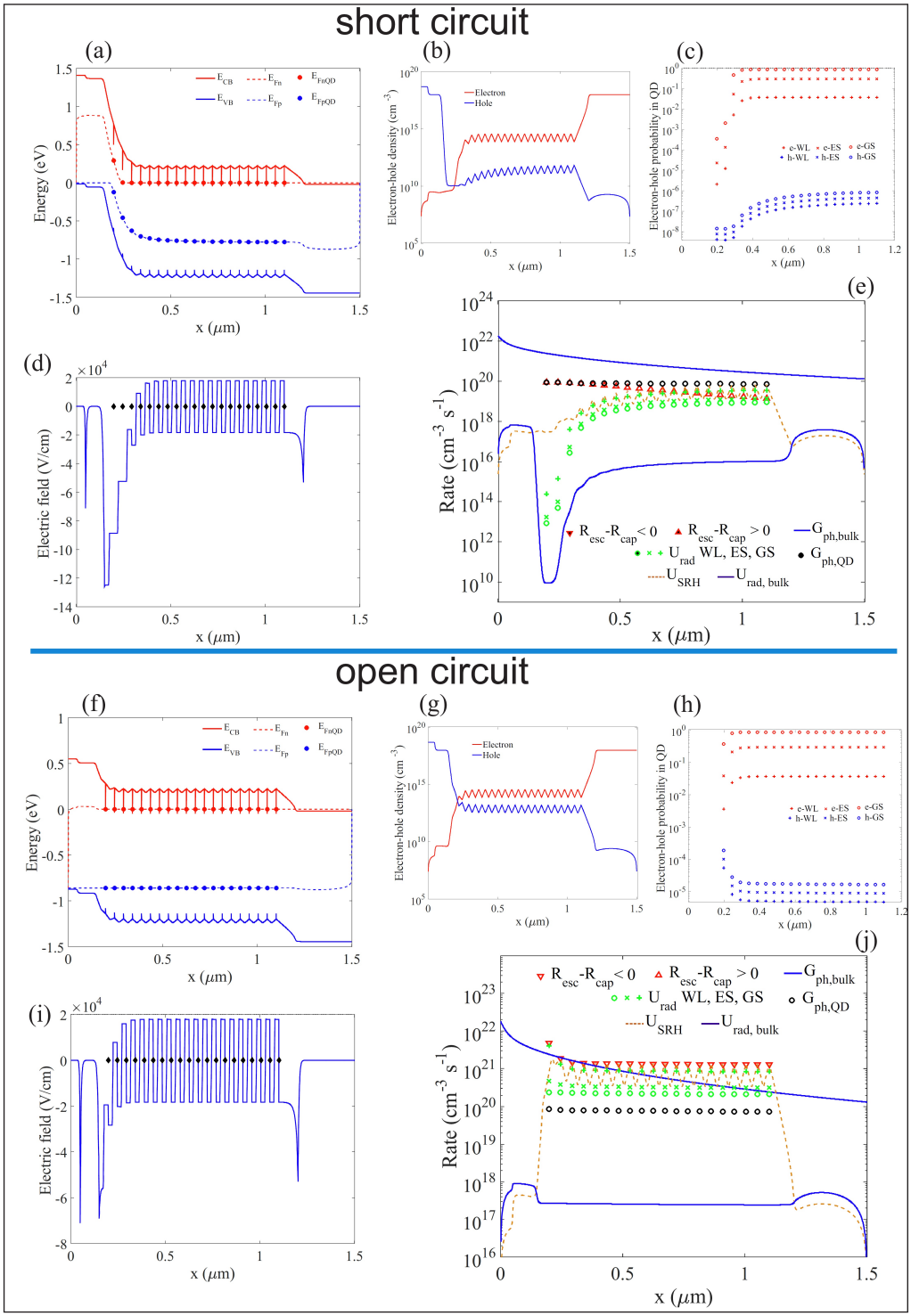


Fig. 3.20 Spatial distribution at short circuit condition of energy bands (a), free carriers density (b), QD occupation probability (c), electric field (d), recombination rates (e). Spatial distribution at open circuit condition of energy bands (f), free carriers density (g), QD occupation probability (h), electric field (i), recombination rates (j). Diamond symbols in the electric field figures (d) and (i) indicate the QD layers position.

# Chapter 4

# Impact of Wetting Layer

In the previous chapter we demonstrated that the impaired performance of quantum dot solar cells can be attributed to the carrier capture and recombination processes in the quantum dots and remarkable $V_{oc}$ recovery might be attained by doping owing to the strong suppression of QD radiative recombination through the confined states. However, the radiative recombination through WL states remains as the limiting factor of the achievable $V_{oc}$.

In this chapter my contribution is to investigate the influence of wetting layer states on the photovoltage loss of InAs/GaAs QDSCs based on provided quantum-mechanical calculation results. Moreover, a simple analytical model that highlights the competition between the barrier and the QD recombination mechanisms and correlates the effective capture rate to the achievable open circuit voltage is introduced.

Quantum-mechanical simulations are used to analyze how the quantum dot electronic states change by Al(Ga)As overgrowth. The change in electronic states are taken into account in device-level simulation in order to assess the influence on the achievable open circuit voltage. Almost full open circuit voltage recovery is predicted by combining doping and wetting layer reduction since, doping suppresses radiative recombination through quantum dot confined states and reduction of wetting layer allows for thermal decoupling between barrier and quantum dot confined states. The results provide theoretical support to several experimental results in the literature and suggest that doping and engineering of QD structure may hold further opportunities for high efficiency QDSCs.

## 4.1 Experimental results

Photoelectron capture from CB to the localized QD states via WL is proposed as the main cause of $V_{oc}$ reduction in InAs/GaAs QDSCs [68]. Because of the nature of self-assembled InAs/GaAs growth by Stranski-Krastanow epitaxy, the significant volume of WL geometrically overlaps with the QDs and becomes an efficient path for capturing the carriers from the barrier into the QDs [69]. Enlarging the energy difference between WL and the confined states was suggested as an effective way to reduce the influence of WL and eliminate carrier capture via WL state: This has been realized by capping the QDs with a wide bandgap material [70, 69, 68].
In Ref. [70], the influences of AlAs cap layer (CL) deposition over InAs quantum dots on performance of QDSCs were investigated. The growth of AlAs CL slightly reduced the $J_{sc}$ of the cell due to the elimination of WL absorption but led to an increase in $V_{oc}$ and enhanced the overall performance of the cell with respect to the one without AlAs CL. The absence of WL was confirmed by cross sectional TEM images and EQE measurement and explained by the substitution of In atoms in the WL by Al atoms due to lower mobility of Al atoms. In Ref. [69], a blue shift of WL state in QDs grown on $Al_xGa_{1-x}As$ and QDs embedded in $Al_xGa_{1-x}As$ barriers with respect to a conventional InAs/GaAs QDs is reported. According to the measured spectral response, the effect of WL state is completely reduced at $x = 0.1$ for QDs that are completely surrounded by $Al_xGa_{1-x}As$. Moreover, in reduced WL (RWL) QDSCs, photoelectron capture and recombination losses via QDs has shown to be suppressed. In another study improved efficiency (0.8%) of charged QDSC with reduced WL is reported [68]. The RWL QD devices were obtained by covering QD layers with $Al_{0.2}Ga_{0.8}As$ and the reduction of WL is confirmed by TEM images and PL measurement at room temperature. The RWL QD device is shown to suppress photoelectron capture and completely recover $V_{oc}$ with respect to the reference cell while having slightly larger $J_{sc}$.

## 4.2 Simulation of InAs/GaAs quantum dot electronic structure

Lens shaped InAs QDs embedded in $Al_xGa_{1-x}As$ layers is modeled with x ranging from 0.05 to 0.2. The following configurations are analyzed whose cross-section is sketched in figure 4.1.

- C1: InAs QD without WL grown on GaAs
- C2: InAs QD with 0.5 nm thick WL grown on GaAs
- C3: InAs QD without WL grown on 1.3 nm thick layer of $Al_xGa_{1-x}As$
- C4: InAs QD with 0.5 nm thick InAs WL grown on a 1.3 nm thick layer of $Al_xGa_{1-x}As$
- C5: InAs QD without WL grown grown on a 1.3 nm thick $Al_xGa_{1-x}As$ and capped with a 1.3 nm layer of $Al_xGa_{1-x}As$
- C6: InAs QD with 0.5 nm thick WL grown on a 1.3 nm thick $Al_xGa_{1-x}As$ and capped with a 1.3 nm layer of $Al_xGa_{1-x}As$

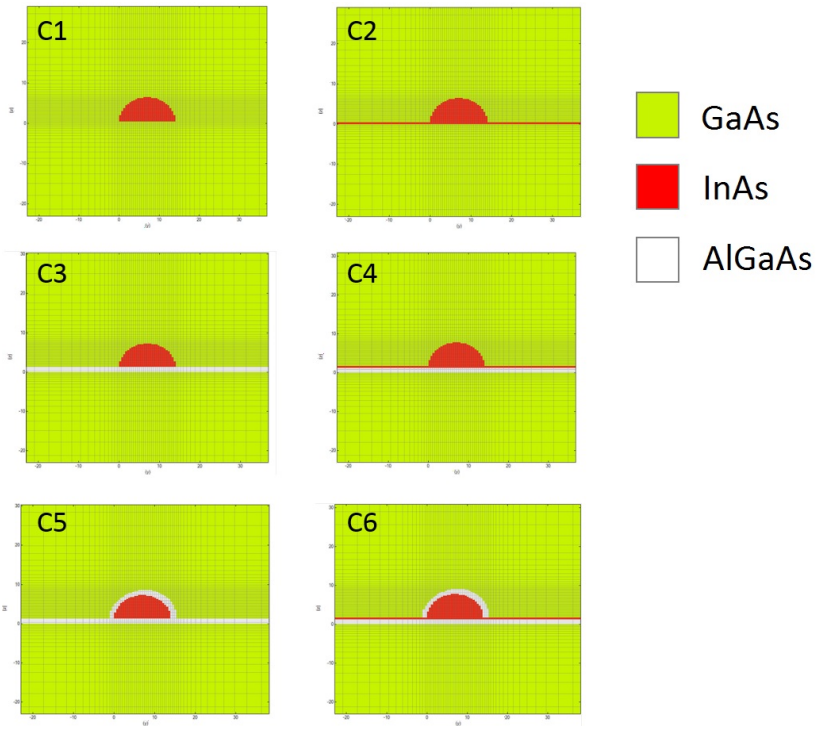


Fig. 4.1 Sketch of the simulated QD configurations.

Configurations C3/C4 and C5/C6 differ for the presence of the InAs WL. Their comparative analysis is intended to assess the influence of physical WL reduction due to the impact of $Al_xGa_{1-x}As$ barriers on the QD electronic states. Following [69], both the cases of QD lens with circular and elliptical base are considered with the following dimensions:

- Circular base: $radius = 14$ nm, $Height = 6$ nm
- Elliptic base: x semi major axis= 24 nm, y semi major axis= 12 nm, Height= 4 nm

Since the qualitative behavior of circular and elliptical case are comparable, in the following we discuss in detail the circular base case study.
Simulations were done by Nextnano software [71]. In Nextnano the calculation is done in two steps. First, the strain distribution is determined using continuum elastic theory and minimizing the free energy within the crystal, and energy bands are calculated taking into account the potential induced by the strain deformation. Then, the QD energy levels are calculated by solving the 3D Schrodinger equation in the

effective mass approximation or exploiting the 6- band or 8-band k·p method. The following results have been obtained by employing the effective mass approximation and could be later refined within a k·p framework.

GaAs barrier thickness is assumed to be 25 nm therefore strain relaxation is calculated within a GaAs volume of 50 nm $\times$ 50 nm $\times$ 50 nm, imposing periodic boundary conditions at the box edges. According to the GaAs zincblende structure, x-axis, y-axis, z-axes are associated to the crystal orientation axes [100], [010],[001], respectively, with z corresponding to the QD growth direction. The calculated strain distribution for the various QD configurations is reported in figure 4.2. The configurations without 0.5 nm WL have similar energy bands and almost identical potential barrier heights as the ones with WL since the strain relaxation along such thin WL is negligible as already reported in [72]. The corresponding energy band diagrams are presented in figure 4.3. It can be noted that the anisotropy between energy barriers along the growth direction and in the QD plane is somewhat reduced from the presence of AlGaAs barriers.

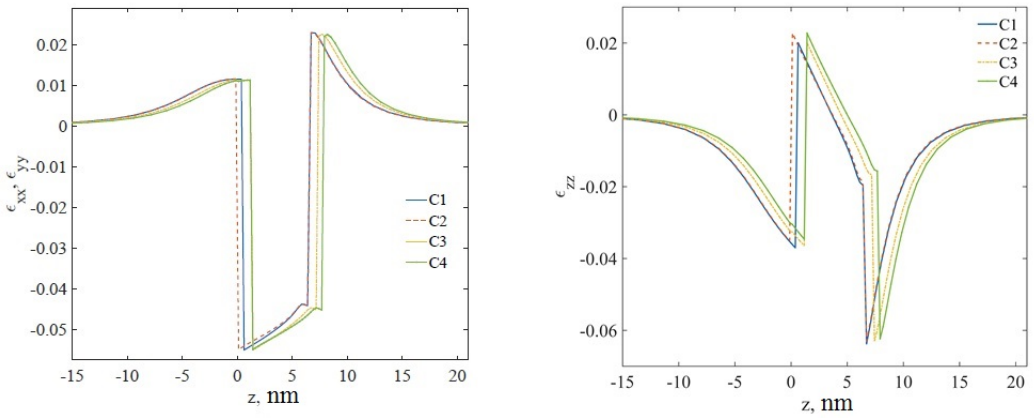


Fig. 4.2 Calculated strain tensor in different quantum dots: without InAs wetting layer (C1), with InAs wetting layer (C2), with bottom $Al_{0.2}Ga_{0.8}As$ layer (C3), with bottom $Al_{0.2}Ga_{0.8}As$ layer and InAs wetting layer (C4). Strain distribution of QDs capped with $Al_{0.2}Ga_{0.8}As$ layer - i.e. configurations C5 and C6 - does not appreciably change with respect to the corresponding uncapped configurations - i.e. C3 and C4 respectively - and thus it is omitted.

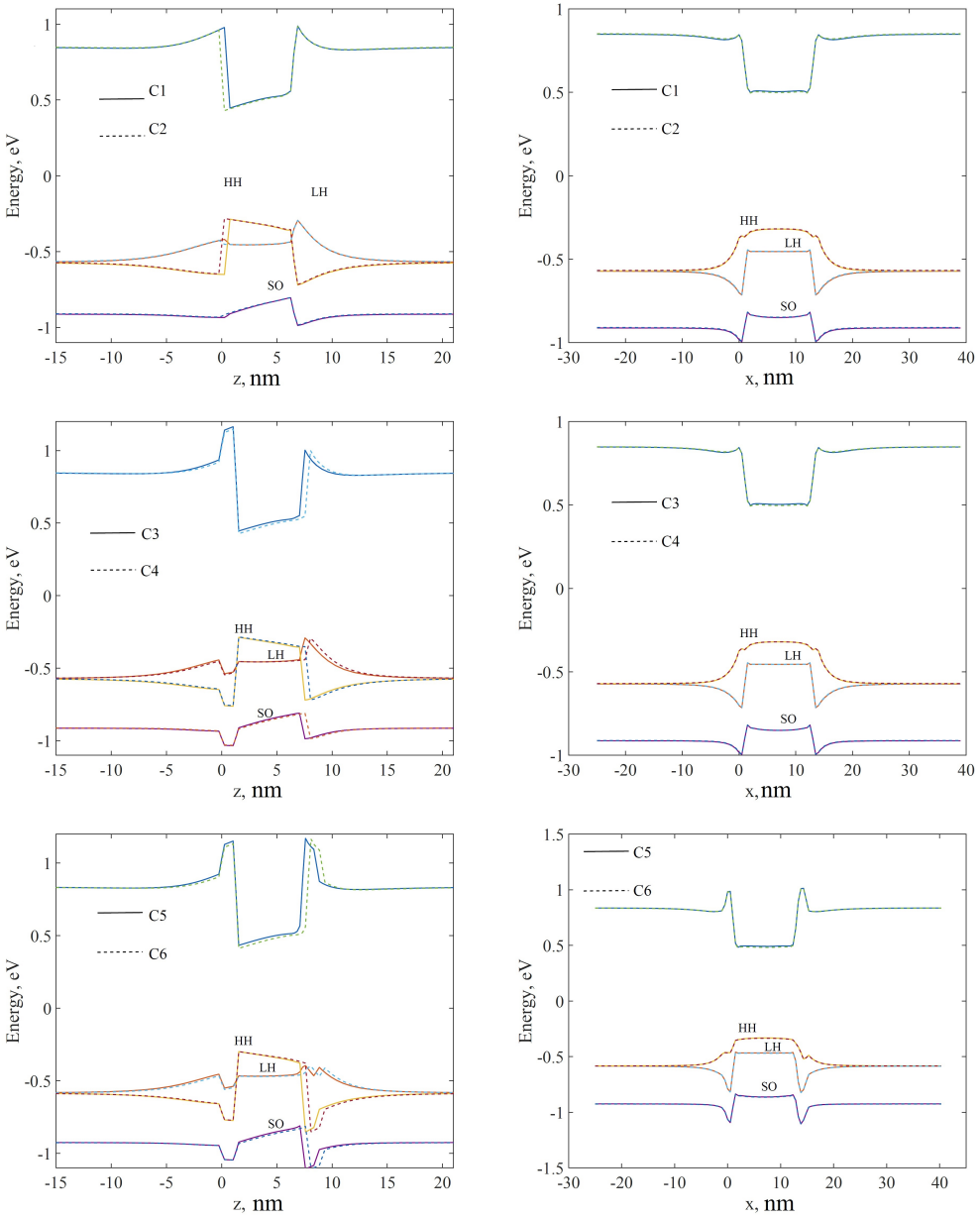


Fig. 4.3 Energy band structure for the various structures in figure 4.1 calculated accounting for the strain distribution. Left: cutline along growth direction (z-axis), at QD base center. Right: cutline along x-axis, at QD center

Figure 4.4 shows the calculated first five energy levels of C2 type QDs. In the following we refer to the highest calculated energy level as WL level or WL state, without implying any correlation with the existence or not of the physical InAs wetting layer. For C2 configuration, the energy difference between electron states

is about 230 meV for the WL-GS transition and 110 meV for the ES-GS transition; hole states are much closer, with energy difference on the order of 10 meV. The associated interband transition energies for GS and WL state are 1.02 eV and 1.27 eV, respectively.

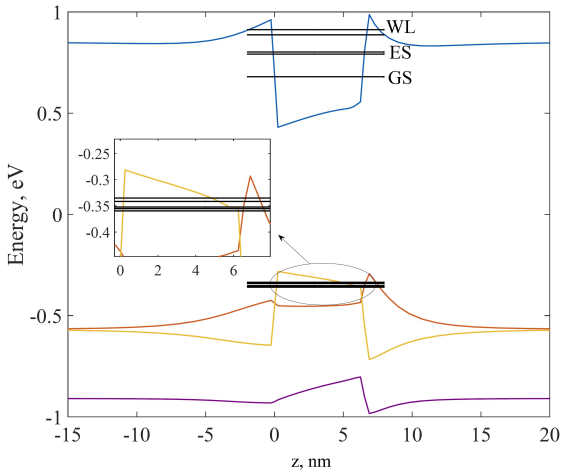


Fig. 4.4 QD levels for C2 configuration.

## 4.3 Impact of AlGaAs barriers and InAs wetting layer on transition energies of quantum dot states

Based on the results in the previous section, we can analyze how wetting layer and AlGaAs barriers affect the calculated QD states. Figure 4.5 shows a comparison of the conventional C2 configuration with those including $Al_{0.2}Ga_{0.8}As$ barrier and addresses the impact of the presence of the InAs wetting layer.

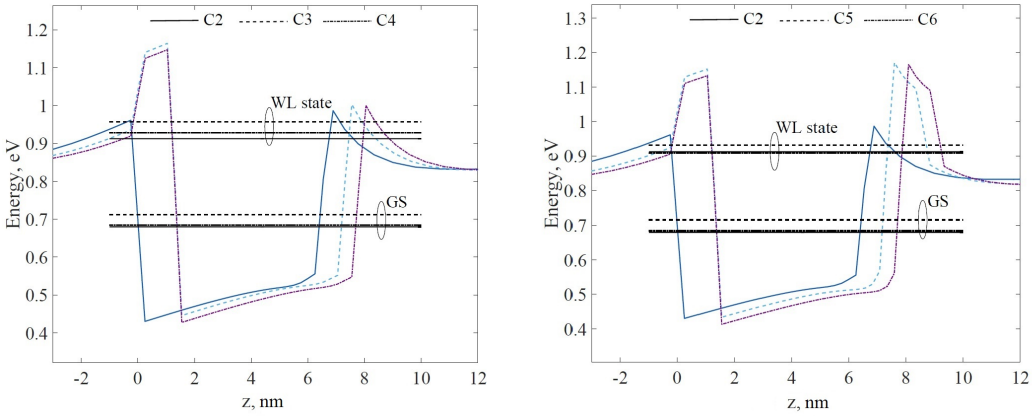


Fig. 4.5 Electron GS and WL states for various structures. Left: uncapped QDs grown on $Al_{0.2}Ga_{0.8}As$ without (C3) and with (C4) InAs wetting layer and reference (C2) QD. Right: QDs surrounded by $Al_{0.2}Ga_{0.8}As$ without (C5) and with (C6) InAs wetting layer and reference (C2) QD.

The comparison points out that the configurations including the InAs wetting layer present deeper states with respect to the configuration without InAs wetting layer owing to the larger effective height of the QD with InAs wetting layer. The structures with AlGaAs layers but without InAs wetting layer present an energy shift of the WL and GS state with respect to the C2 configuration. A similar behavior is observed for hole states. As shown in figure 4.6, this turns into a larger change of interband transition energies with respect to Al fraction in the configurations without the WL. Figure 4.6 also highlights the larger dependence of transition energies on Al fraction in configurations with capped QDs, owing to the dominant influence of the top AlGaAs barrier.

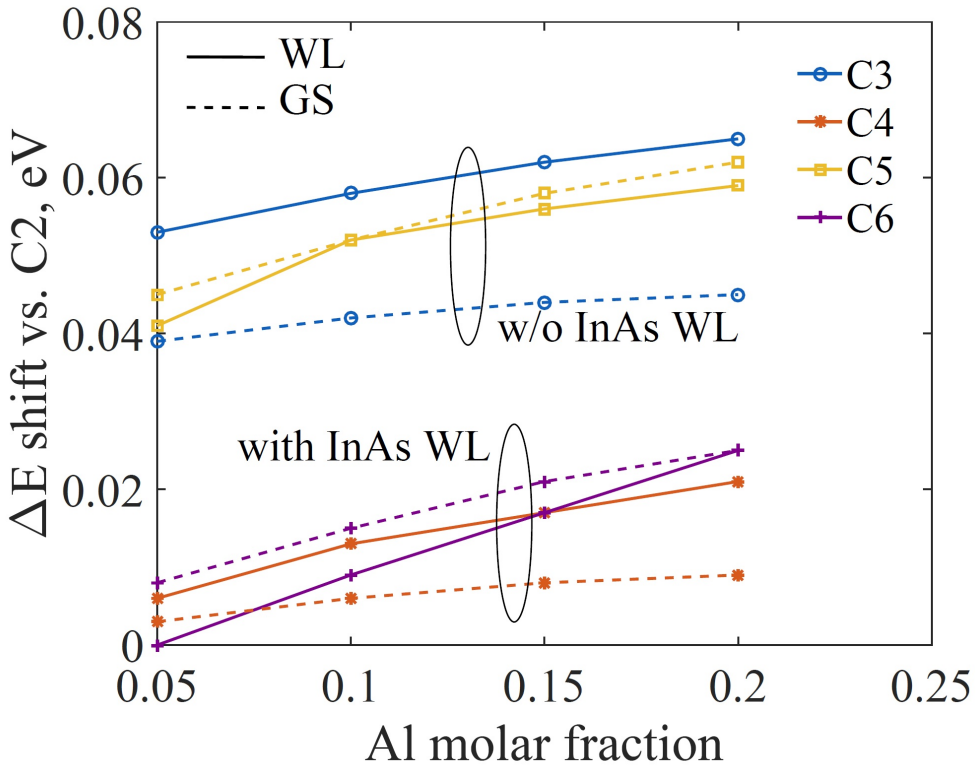


Fig. 4.6 Change of the WL and GS transition energy with respect to the reference (C2) as a function of Al molar fraction for the various configurations including $Al_xGa_{1-x}As$ barriers.

In order to correlate such results with the experimental ones, we analyse in figure 4.6 the shift of GS and WL interband transition energy with respect to the transition energy of the reference configuration C2 (i.e. the simple QD with InAs wetting layer). From this comparison it turns out that configuration C4, i.e. QD grown on AlGaAs and including the InAs wetting layer, provides a change of about 20 meV for Al molar fraction going from $x = 0$ to $x = 0.2$, comparable to the one observed experimentally in [69]. On the other hand, for surrounded QDs, configuration C5 (i.e. QD embedded in AlGaAs barriers and without InAs wetting layer) shows a larger energy shift, ranging from about 40 meV to 60 meV as the Al fraction changes from $x = 0.05$ to $x = 0.2$, that could explain the large blueshift observed in [69] that is about 30 meV for Al molar fraction of 0.05 and the disappearance of the WL photoresponse peak at larger Al molar fractions.

As already mentioned, the presented results have been obtained within the effective mass approximation. A preliminary check of the robustness of the results is carried out by repeating the analysis with the 8-band k·p method for configurations C2 and

C5. As shown in figure 4.7, the calculated shift in transition energy for the GS and WL states of C5 configuration - with Al fraction of 0.2 - with respect to the C2 one, are approximately 50 meV and 80 meV, respectively, in reasonable agreement with those estimated with the effective mass approximation. Clearly, the error increases as the state number increases, and thus is larger for the WL state, since the error introduced by the constant effective mass approximation becomes larger for higher energy states. It is worth noticing that also the dependence of energy shift on Al fraction predicted by the k·p method is comparable with the one obtained with the effective mass approximation.

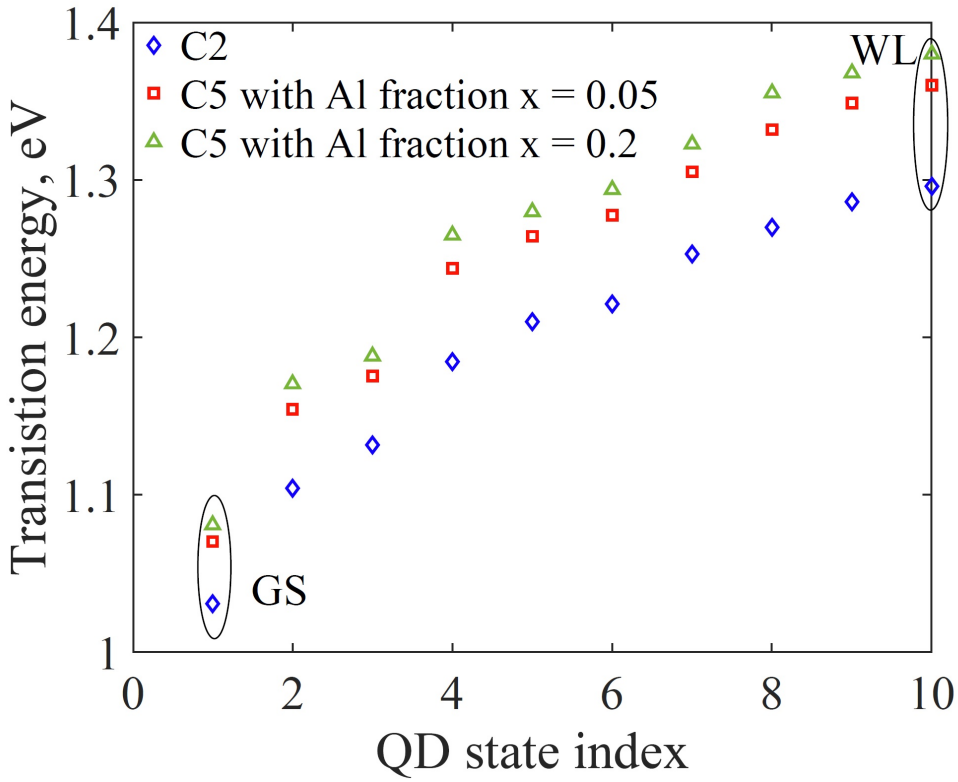


Fig. 4.7 Transition energies of the first 10 QD states with configuration C2 and C5, calculated by the 8-band $k\dot{p}$ model.

## 4.4 Effect of WL States on photovoltage

Correlation between QD media and solar cell performance is studied considering the simple structure mentioned in the previous chapter that is a simple GaAs-only solar

cell without widegap window and back surface field layers, whose intrinsic region is made by a stack of 20 QD layers separated by GaAs spacer layers of about 50 nm thickness. In previous chapter we studied the cell to assess the effect of selective doping on photovoltaic behavior and photoluminescence. The reported QD media is taken as reference: these QDs are characterized by WL, ES, and GS energy states at about 1.29, 1.22 and 1.13 eV with inter-level spacing and capture and relaxation time constants specified in Table 4.1.

Table 4.1 QD Parameters

| | |
|---|---|
| QD plane density [$cm^{-2}$] | $6 \times 10^{10}$ |
| ES and GS degeneracy | 4, 2 |
| WL density of states [$cm^{-2}$] | $2.4 \times 10^{12}$ |
| $\Delta^e_{\text{B-WL}}$, $\Delta^e_{\text{WL-ES}}$, $\Delta^e_{\text{ES-GS}}$ [meV] | 140 62 70 |
| $\Delta^h_{\text{B-WL}}$, $\Delta^h_{\text{WL-ES}}$, $\Delta^h_{\text{ES-GS}}$ [meV] | 4 4 16 |
| $\tau^e_{\text{CAP,B-WL}}$, $\tau^e_{\text{CAP,WL-ES}}$, $\tau^e_{\text{CAP,ES-GS}}$ [ps] | 0.3, 1, 1 |
| $\tau^h_{\text{CAP,B-WL}}$, $\tau^h_{\text{CAP,WL-ES}}$, $\tau^h_{\text{CAP,ES-GS}}$ [ps] | 0.1, 0.1, 0.1 |
| $\tau_r^{\text{WL}}$, $\tau_r^{\text{ES}}$, $\tau_r^{\text{GS}}$ [ns] | 1, 1, 1 |
| QD thickness ($t_{\text{QD}}$) [nm] | 4 |

The influence of $Al_xGa_{1-x}As$ barriers embedding the QDs is studied in terms of shift of the WL energy state in the conduction band with respect to the reference QD media. We focus on electron states only, since hole states are found to be shallower and with a small energy separation, providing a very efficient thermal coupling to the barrier, for all the studied QD configurations. For the sake of simplicity we neglect the simultaneous GS and ES levels shift, since at high doping levels the photovoltage is not influenced by these levels and therefore the hypothesis does not affect the amount of photovoltage recovery. On the other hand, for the undoped or low doping case, the hypothesis provides a worst-case prediction of achievable $V_{oc}$. As stated in previous chapter, comparable voltage recovery may be expected regardless of the specific doping technique for QDs therefore, in the following we restrict the analysis to directly-doped cells, where direct doping is modeled by placing a 5 nm thick $\delta$-doping layer at each QD layer. The sheet density of dopants is set to a multiple ($\alpha$) of the QD density so as to nominally provide $\alpha$ carriers per dot. Simulations, carried out at ambient temperature (T = 300 K) include barrier radiative recombination,

with radiative coefficient set to $2.0 \times 10^{-10}\text{cm}^3\text{s}^{-1}$, and defect induced non-radiative recombination with Shockley Read Hall (SRH) carrier lifetime of 500 ns, corresponding to a high quality barrier, working close to the radiative limit. Radiative lifetime in QD states is set to 1 ns.

Figure 4.8 shows the External Quantum Efficiency (EQE) of undoped cells with QD media with WL confinement energy ($\Delta E^{e}_{\text{B-WL}}$) reduced from 140 meV (reference QD) to 60 meV. Besides WL shift and consequent reduction of the harvested light spectral range, a slight decrease of ES and GS states is observed due to the decreased thermal coupling between these states and the WL one. The penalty is however negligible in terms of total QD photogeneration and will be even smaller if concomitant upward shift of GS and ES is accounted for.

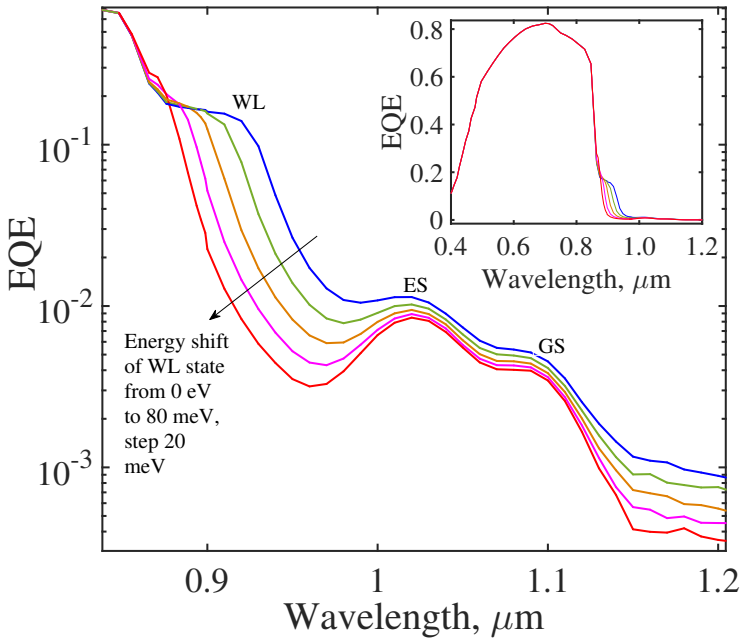


Fig. 4.8 Calculated external quantum efficiency for WL confinement, $\Delta^{E}_{\text{B-WL}}$, ranging between 140 meV and 60 meV. The inset shows the EQE in the whole spectral range.

Figure 4.9 analyses the combined effect of WL shift and selective doping on the achievable open circuit voltage. For the sake of reference, a baseline GaAs cell with the same geometry reaches a $V_{oc}$ of 0.953 eV. The undoped cell is insensitive to the WL position, since the photovoltage loss is dominated by the radiative recombination through the confined states. As doping is introduced, carrier capture in these states

is reduced by strengthening the thermal escape from the QDs (i.e. moving the WL state closer to the barrier) and remarkable loss mitigation is possible, by blocking via doping the further relaxation in the GS and ES, that would otherwise behave as very efficient recombination centers. For the larger WL confinement, selective doping allows for a $V_{oc}$ recovery of about 80 mV, that increases to about 110 mV for the reduced WL cell, attaining almost full $V_{oc}$ recovery ($V_{oc}$ = 0.950 V). The results compare very well with the literature data of similar structures, where the maximum demonstrated $V_{oc}$ recovery ranges between 105 mV in the direct-doped cells [50] to 120 mV in modulation-doped cells [49].

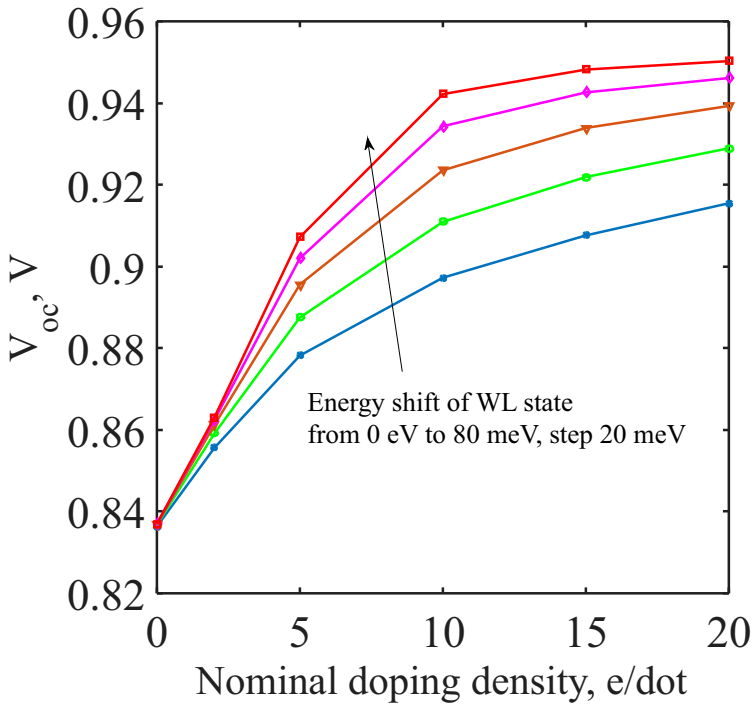


Fig. 4.9 Open circuit voltage as a function of the nominal per dot density and WL confinement. Simulations were done under 1 sun AM1.5 G illumination.

The raise of photovoltage with doping density becomes larger as WL state is less confined owing to the reduced thermal coupling via WL states between barrier and QD confined states. As shown in figure 4.10, this leads to a more efficient filling of ES and GS states through doping. Thus, reduction of the WL somewhat relaxes the amount of doping level required for attaining large $V_{oc}$ recovery. As a matter of fact, high density doping could even deteriorate the material quality inducing further nonradiative recombination centers [53, 73]. Moreover, doping obviously causes

some penalty in the achievable QD photogeneration. Thus, engineering QD shape and size combined with doping could provide a better trade-off in terms of power conversion efficiency. In the present case study, the cell with deeper WL reaches a maximum efficiency of 16.6% at 15 e/dot, while the cell with shallower WL reaches an optimum efficiency of 17.24% (slightly lower than the reference cell optimum efficiency of 17.28%) at 10 e/dot doping level. These results are very encouraging, considering that the model completely neglects any mechanism that could mitigate thermalization losses, such as two-photon absorption [11] or carrier escape through scattering with hot electrons [74, 75]. Furthermore, even in such situation, enhancing QD photogeneration, e.g. through light-trapping approaches, could make the QD cell to overcome its bulk counterpart [48].

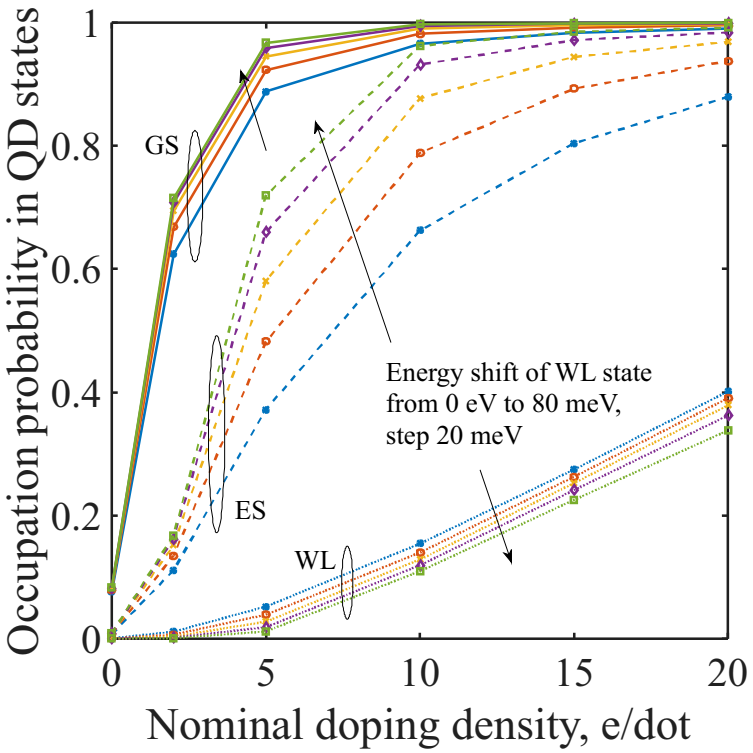


Fig. 4.10 Occupation probability in the QD states (at open circuit condition) as a function of the nominal per dot density and WL confinement.

In conclusion, once capture and recombination through GS and ES have been suppressed, WL states remain as the ultimate recombination channel loss induced by QDs. The reduction of WL confinement and the enhanced thermal coupling between WL and barrier weakens the effective capture rate in WL, as evidenced

by the decrease of WL states occupation probability as WL energy shifts towards the barrier. This turns into a decreased photoluminescence at room temperature in capped QDs as experimentally observed in [68], and yields the full recovery of $V_{oc}$ observed in figure 4.9.

## 4.5 Correlation between $V_{oc}$ penalty and effective quantum dot capture time

The competition between barrier and QD recombination channels and their influence on the cell photovoltage may be clearly appraised by analyzing the free charge balance across the cell at open circuit. Under DC condition, by using first-order lifetime approximations for the net barrier recombination terms and the net QD capture rate, the continuity can be recast as:

$$\frac{1}{q}\frac{\partial J_n}{\partial x} - \frac{n}{\tau_{\text{eff}}^{\text{B}}} - \frac{n}{\tau_{\text{eff}}^{\text{QD}}} + G_{\text{ph}}^{\text{B}} = 0 \tag{4.1}$$

where the lifetimes $\tau_{\text{eff}}^{\text{B}}, \tau_{\text{eff}}^{\text{QD}}$ represent the equivalent effective lifetime for recombination mechanisms involving barrier states [76] and the effective QD capture (and subsequent recombination) time through QD states, respectively. At open circuit the cell operates close to flat-band condition, thus $\frac{\partial J_n}{\partial x} = 0$. Using the junction law $n \approx n_0 \exp(V/V_T)$, $n_0$ being the thermal equilibrium electron density), eq.4.1 yields an approximate compact expression for the open circuit voltage, from which we can estimate the penalty, $\Delta V_{oc}$, induced by the QDs:

$$\Delta V_{oc} \approx V_T \ln\left(1 + \frac{\tau_{\text{eff}}^{\text{B}}}{\tau_{\text{eff}}^{\text{QD}}}\right) \tag{4.2}$$

Clearly, when $\tau_{\text{eff}}^{\text{B}} \gg \tau_{\text{eff}}^{\text{QD}}$ e.g. in the undoped cell, $\Delta V_{oc} \approx V_T \ln\left(\frac{\tau_{\text{eff}}^{\text{B}}}{\tau_{\text{eff}}^{\text{QD}}}\right)$ when $\tau_{\text{eff}}^{\text{B}} \ll \tau_{\text{eff}}^{\text{QD}}$, $\Delta V_{oc} \approx 0$. The effective QD capture time, estimated as the ratio between the average carrier density and the average net capture rate across the QD region, is analyzed in figure 4.11 as a function of doping density and barrier-WL energy

spacing. At low doping levels, $\tau_{\text{eff}}^{\text{QD}}$ is weakly dependent on WL state confinement and increases exponentially with the doping density in agreement with the theoretical predictions in [77] and experimental data in [78]. Namely, considering the thermally activated nature of the process, we find that $\tau_{\text{eff}}^{\text{QD}}$ grows as $\exp(K_\alpha \alpha / k_{\text{BT}})$, with $K_\alpha = 15 - 20$ meV/(e/dot) depending on the doping density. At larger doping levels, the increase of $\tau_{\text{eff}}^{\text{QD}}$ with doping is slower, due to the large density of states available in the WL. However, the reduced WL confinement causes a marked reduction of carriers capture in QDs, owing to the decreased WL occupation probability seen in figure 4.10.

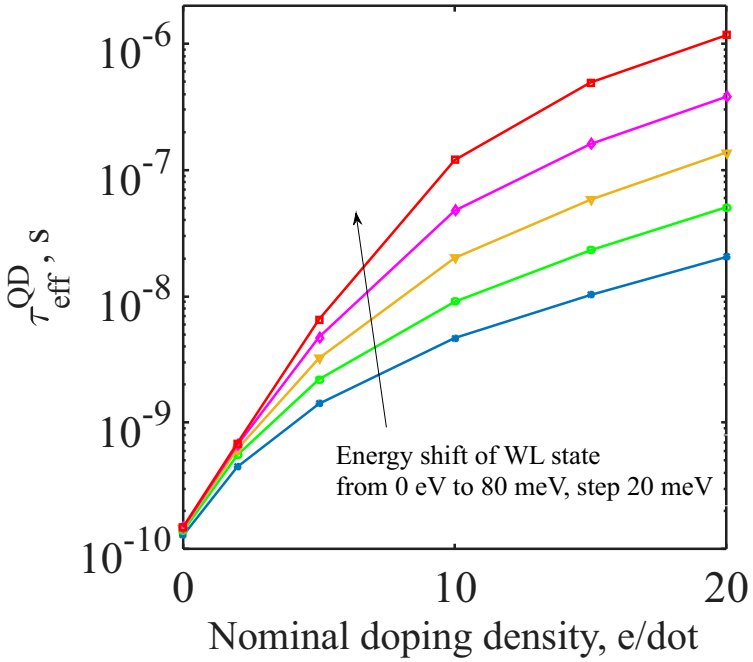


Fig. 4.11 Effective QD capture time estimated from the numerical simulations at open circuit condition.

Finally, figure 4.12 maps the open circuit voltage penalty of QD cells, $\Delta V_{oc}$, as a function of the effective QD capture time for the different doping levels and WL energies. Numerical data show a good correlation with the analytical expression in eq.4.2. The deviation from a pure exponential dependence can be understood taking into account that doping influences, besides QD dynamics, the potential profile and non radiative recombination in the barrier. For increasing doping levels, the equivalent barrier lifetime in eq.4.2 must be increased from 10 ns to 100 ns to follow

the trend shown by the numerical data, pointing out the complex interplay between QD and barrier recombination mechanisms. Nonetheless eq.4.2 provides a simple expression to derive an indicative estimation of QD capture rate from the measured $V_{oc}$ loss.

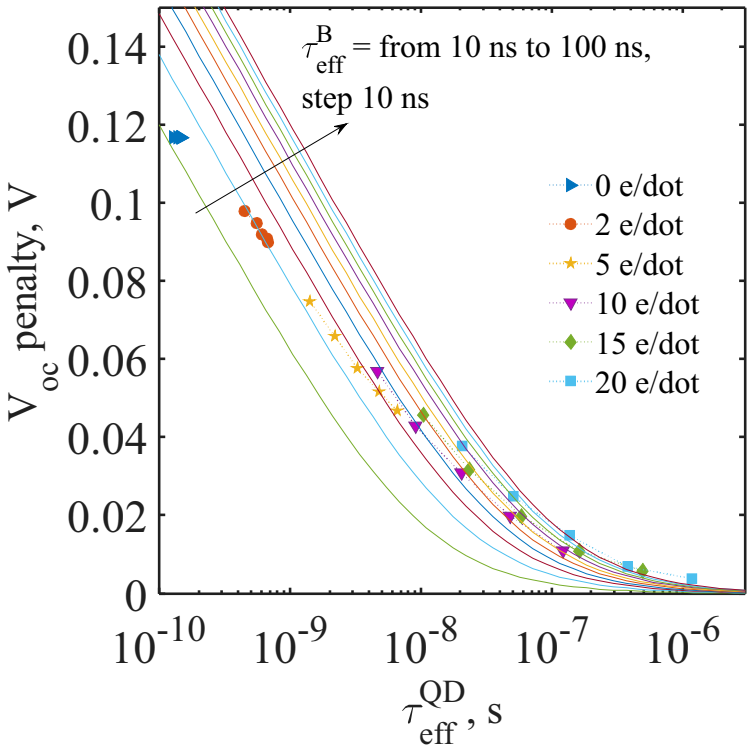


Fig. 4.12 Correlation between the $V_{oc}$ penalty and effective QD capture time in figure 4.11. Symbols are the results of numerical simulations, grouped by doping level and for WL confinement changing from 140 to 60 meV. Solid lines represent the $V_{oc}$ penalty calculated according to eq.4.2.

Results show that wetting layer reduction is effective only in charged QDs, because the reduction of thermal coupling between barrier and QD states must occur together with a reduction of QD radiative recombination which can be achieved by filling the QD confined states through doping. Nevertheless, wetting layer reduction is shown to reduce, at least to some extent, the doping density required for $V_{oc}$ recovery. In this context it is worth noticing that the full recovery achieved in [68] is the result of reduction of wetting layer confinement, low interdot (1 e/dot) modulation doping and substantial uniform doping (n-type, $2 \times 10^{17}\text{cm}^{-3}$) of the QD region.

# Chapter 5

# Future studies: QD systems with Type-II band alignment

The chapter provides a brief description of type-II band alignment based on GaSb/GaAs material system and presents a preliminary study of the competition between thermal and optical escape processes in GaSb/GaAs quantum dot solar cells. In fact, the GaSb/GaAs system presents interband and intraband dynamics which are more promising than those of the InAs/GaAs system in view of attaining the IB operating regime [18]. To this aim, the model described in Chapter 2 includes now intersubband optical processes.

## 5.1 GaSb/GaAs type-II quantum dot solar cells

GaSb quantum dots with staggered band alignment (type-II) are grown on GaAs surface upon 1.2 nm deposition of GaSb [79]. Like InAs quantum dots, the GaSb quantum dot growth is a self-organized Stranski-Krastanov process. In GaSb/GaAs material system, the holes are confined deeply within GaSb valence band. Such a deep confinement in a direct gap material provides photon absorption and detection in mid (3-5 $\mu$m) wavelength infrared (MWIR) window. Formation of GaSb QDs, results in new PL peak in addition to the WL. This peak is due to the radiative recombination between 0D holes and the electrons in the quantum shell around GaSb [79].

Suzuki et al. [80] investigated the excitation power dependence of the PL peak

energies for the GaSb/GaAs QDs. The study shows that the QD peak shifts towards higher energies with increasing excitation power density which is an indication for type-II band alignment. The shift of the QDs peak was observed to be 6.5 times larger than that of the WL (See figure 5.1).

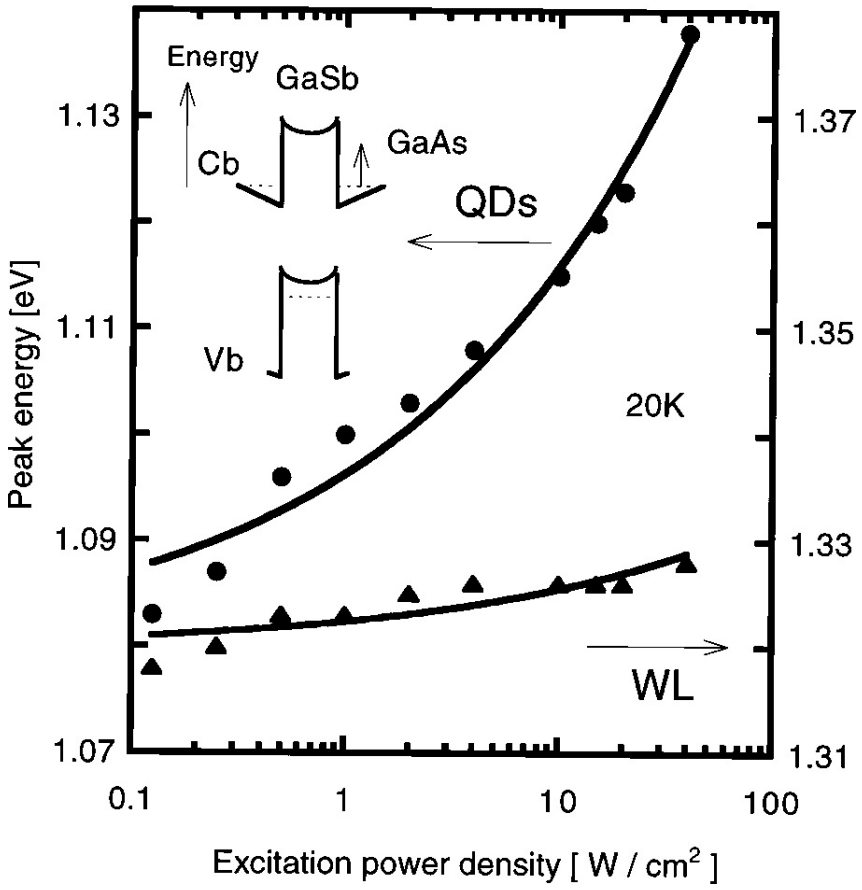


Fig. 5.1 Taken from [80]. The excitation power dependence of the PL peak energies for the GaSb/GaAs QDs. The inset shows a schematic diagram of the conduction and valence bands for type-II band alignment with a band bending effect due to spatially separated charge.

Regarding the temperature behavior of the PL, WL thermal quenching of GaSb/GaAs is observed in experimental studies [79, 80] (See figures 5.2 and 5.3). In [79] at temperature higher than 100 K, the PL is dominated by lower QD energy state and the peaks follow the temperature dependency of GaAs bandgap. The study suggests that this dominance is due to the thermally evaporated holes from the WL and their subsequent capture by the QDs. Other explanations are given in [80]: (i) With increasing temperature, PL quenching of WL is dominated by recombination

through interface defects. (ii) The observed thermal quenching of the PL is due to dissociation of excitons into electron-hole pairs which can then escape from WL via thermionic emission.

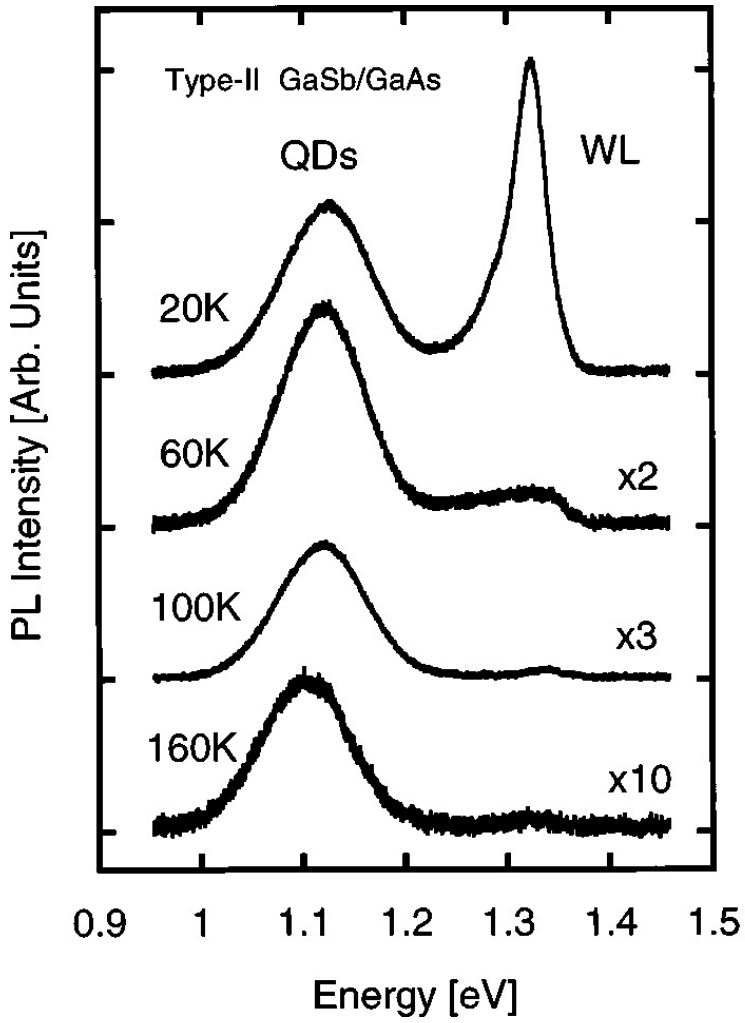


Fig. 5.2 Taken from [80]. Temperature dependence of PL spectra for the GaSb QDs. With increasing temperature.

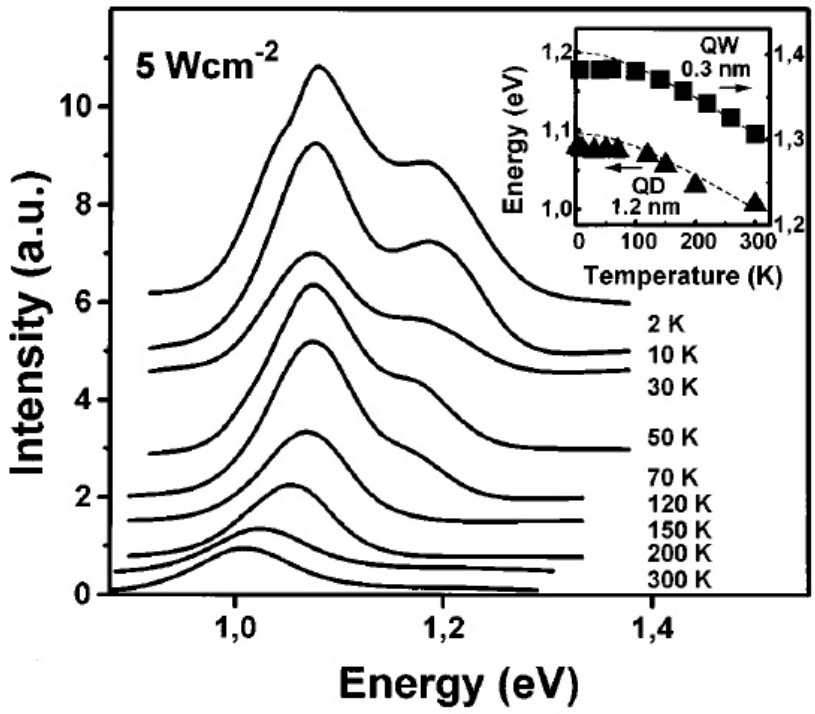


Fig. 5.3 Taken from [79]. Temperature dependence of the PL spectra in a sample with GaSb quantum dot. The inset show the shift of the PL peak with respect to the temperature. The behavior of GaAs bandgap with respect to temperature (shifted in energy scale) is also shown for comparison as a dashed line.

Thermal emission in type-II QD systems have two competing mechanism: (1) Suppression of thermal emission due to large confinement potential and enhanced energy quantization. (2) Large effective mass in valence band which reduces energy quantization and enhances thermal emission [18]. Hwang et al. [18] investigated the competition between thermal escape and optical generation for type-II GaSb/GaAs QD system. The study shows that thermal emission in type-II GaSb/GaAs QDs is lower than the one of type-I InAs/GaAs QDs. Moreover, in type-II GaSb/GaAs QDs, optical emission becomes dominant at high solar concentration (1000x and higher).

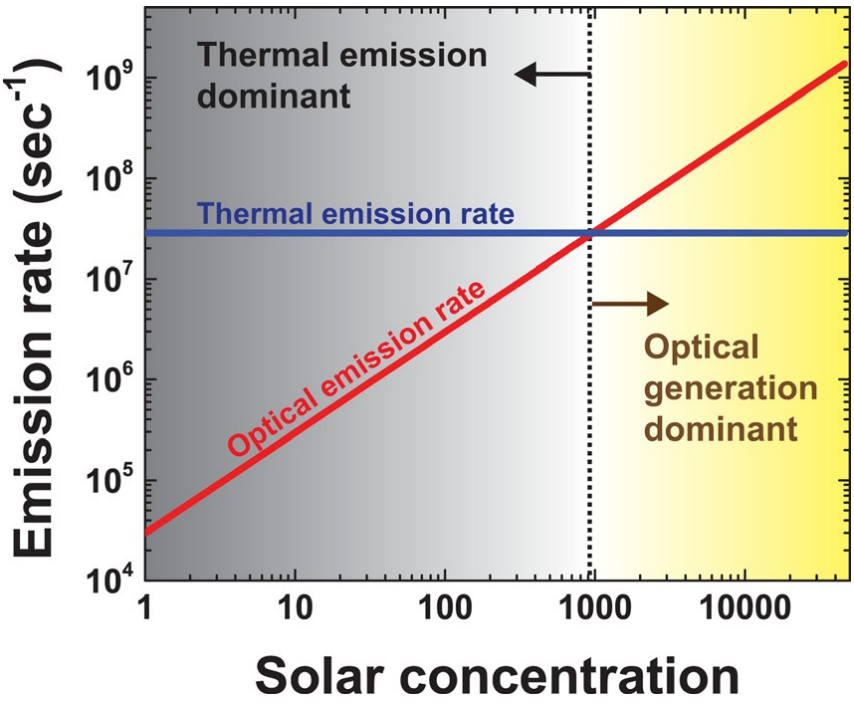


Fig. 5.4 Taken from [18]. Optical and thermal emission of holes in GaSb/GaAs QDs under different solar concentration

## 5.2 Preliminary study of GaSb/GaAs quantum dot solar cells

Two quantum dot models are considered in our study as representative of InAs/GaAs type-I and GaSb/GaAs type-II QDs within an identical bulk structure: a p-i-n configuration illuminated from the p-side. The p-emitter consists of 50 nm $p^+$- and 100 nm p-GaAs with doping density of $5 \times 10^{18}$ and $1 \times 10^{18}$ $cm^{-3}$ respectively. 100 nm intrinsic region contains 5 stacks of QDs with QD plane density of $1 \times 10^{10}$ $cm^{-2}$ for each QD layer. The intrinsic region is grown with 50 nm intrinsic GaAs buffer layer on top of 50 nm $n^+$ GaAs with doping density of $1 \times 10^{18}$ $cm^{-3}$. The two QD configurations are shown in figure 5.5.


Fig. 5.5 Case studies band alignment: (a) representative of InAs/GaAs QDs. (b) representative GaSb/GaAs QDs

For InAs/GaAs type-I QDs, the parameters are taken from the previous study mentioned in chapter 3. Regarding GaSb/GaAs type-II QDs, one confined energy state is considered with confinement energy level of 350-400 meV. Furthermore, the WL is eliminated due to the observed thermal quenching of WL peak at room temperature PL measurements [79, 81] (see figure 5.3).
The radiative recombination lifetime is obtained based on time resolved PL (TRPL) measurements in [82, 83]. According to these studies the radiative recombination lifetime in the staggered band-aligned of GaSb QDs is longer than that one of the type-I QDs due to lower spatial overlap between electron and hole wavefunctions. Liang et al. [82] reported a decay time of $\tau = 11.5$ ns. Sun et al. [83] extracted two components for the decay time: An initial intensity-dependent fast component with $\tau_1 = 7.5$ ns and an intensity-independent slow tail component with $\tau_2 = 23$ ns. The study suggested that the overlap between electrons and holes depends on the hole population in the confined state. Therefore, as the hole population decreases, the band bending near the QDs and consequently the overlap between electron and hole wavefunctions decreases. Since our model accounts for constant radiative lifetime for QD states, a radiative lifetime of 10 ns is assumed for the simulation of GaSb/GaAs QDs which is an order of magnitude larger than the one of InAs/GaAs type-I.
The capture time is assumed to be 5 ps as identified by Komolibus et al. [84].
Due to lack of enough experimental data on absorption coefficient in GaSb/GaAs QDs and to have a reasonable comparison between the two QD models, the absorption profiles for both type-I and type-II QDs are assumed to be constant over the corresponding QD states energy transition range. Respecting Van Roosbroeck-Shockley relation [26], the first transition absorption coefficient (confined state→CB)

in type-II QDs is assumed to be an order of magnitude weaker than of that of the type-I since the radiative recombination lifetime in type-II QDs is assumed to be an order of magnitude larger than of the type-I QDs. Regarding the second transition (i.e. confined state→VB), the absorption coefficient is assumed to be equal to the type-I first transition. Luque et al. [85] also assumed $\alpha_{CI} << \alpha_{IV}$ due to delocalized electron wavefunction in the CB. The employed absorption coefficients are presented in figures 5.6 and 5.7 for type-I InAs/GaAs and type-II GaSb/GaAs QDs respectively.

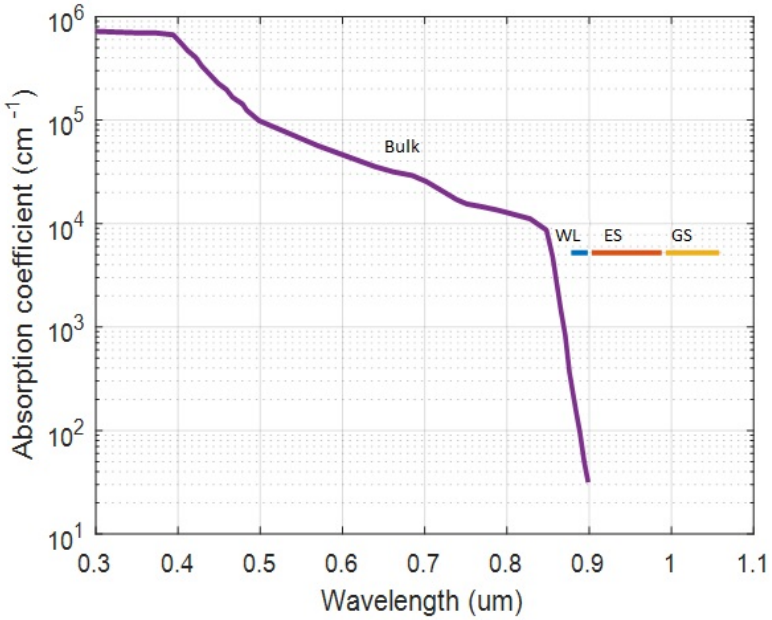


Fig. 5.6 Absorption coefficient of type-I InAs/GaAs QDs along with bulk GaAs absorption..

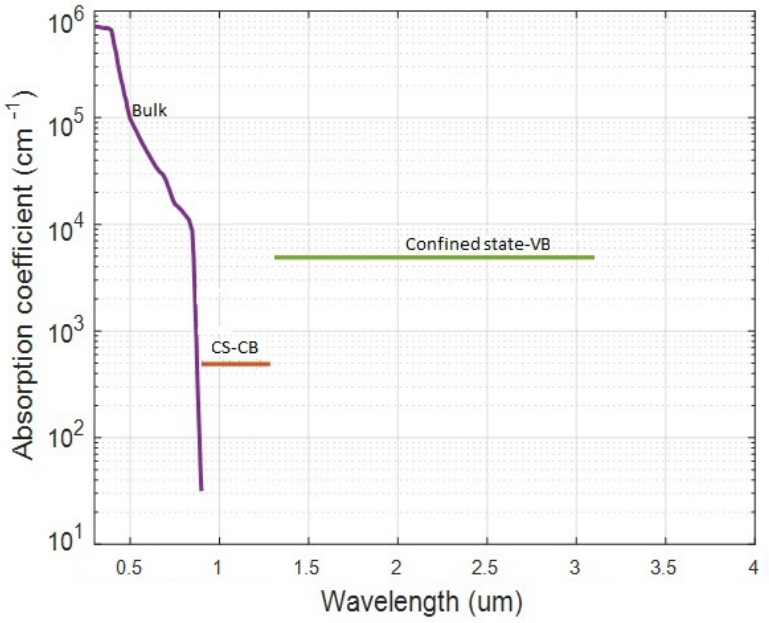


Fig. 5.7 Absorption coefficient of type-II GaSb/GaAs QDs along with bulk GaAs absorption..

A summary of quantum dot parameters for type-I and type-II are presented in tables 5.1 and 5.2 respectively.

Table 5.1 Type-I InAs/GaAs QD parameters

| | |
|---|---|
| QD plane density [cm$^{-2}$] | $1 \times 10^{10}$ |
| WL, ES, GS degeneracy | 40, 4, 2 |
| $\Delta^{e}_{\text{B-WL}}$, $\Delta^{e}_{\text{WL-ES}}$, $\Delta^{e}_{\text{ES-GS}}$ [meV] | 140 62 70 |
| $\Delta^{h}_{\text{B-WL}}$, $\Delta^{h}_{\text{WL-ES}}$, $\Delta^{h}_{\text{ES-GS}}$ [meV] | 4 4 16 |
| $\tau^{e}_{\text{CAP,B-WL}}$, $\tau^{e}_{\text{CAP,WL-ES}}$, $\tau^{e}_{\text{CAP,ES-GS}}$ [ps] | 0.3, 1, 1 |
| $\tau^{h}_{\text{CAP,B-WL}}$, $\tau^{h}_{\text{CAP,WL-ES}}$, $\tau^{h}_{\text{CAP,ES-GS}}$ [ps] | 0.1, 0.1, 0.1 |
| $\tau_r^{\text{WL}}$, $\tau_r^{\text{ES}}$, $\tau_r^{\text{GS}}$ [ns] | 1, 1, 1 |
| $\alpha^{\text{WL}}$, $\alpha^{\text{ES}}$, $\alpha^{\text{GS}}$ [cm$^{-1}$] | 5000, 5000, 5000 |

Table 5.2 Type-II GaSb/GaAs QD parameters

| | |
|---|---|
| QD plane density [$cm^{-2}$] | $1 \times 10^{10}$ |
| Confined state degeneracy | 6 |
| $\Delta^{h}_{\text{B-confined state}}$ [meV] | 350-400 |
| $\tau^{h}_{\text{CAP,B-confined state}}$ [ps] | 5 |
| $\tau_{r}^{\text{confined state}}$ [ns] | 10 |
| $\alpha$ [$cm^{-1}$] | 500 |

In order to obtain the sub-bandgap response of GaSb/GaAs QDSC, the photocurrent is simulated at short circuit with two monochromatic light sources, each with intensity equal to 1 mW $cm^{-2}$. The secondary light source illuminates photons with energy equal to the first energy transition (i.e. QD state→CB). This light source (also known as photo-filling light source) is necessary to maximize the hole density in the confined state of undoped QDSCs to complete the second transition [86]. The primary light source is then swept over the wavelength. Figure 5.8 presents the short circuit spectral response (at ambient temperature) of the type-II GaSb/GaAs QD device. The peak at 3.5 $\mu$m is due to the large valence band discontinuity.

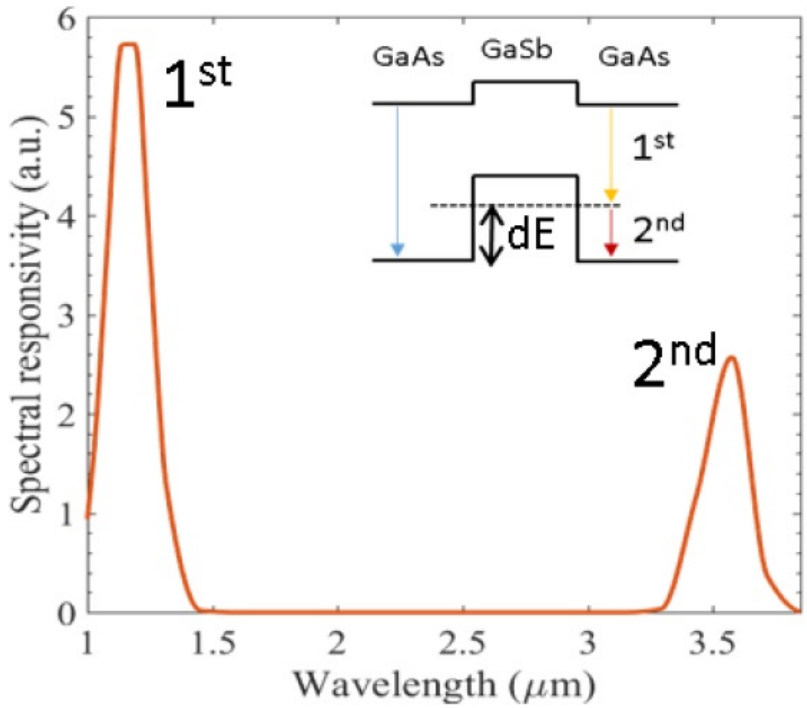


Fig. 5.8 Spectral responsivity of GaSb/GaAs QD device

The behavior of photocurrent at 3.5 $\mu$m with respect to bias intensity (secondary light source) is shown in figure 5.9. In the figure dE denotes the energy confinement of the QDs. The simulation results show that photocurrent tends to saturate at high intensity for the confinement energy of 400 meV which is due to suppression of thermal escape from the QDs while for the case of 350 meV the linear behavior suggests that the escape mechanism is still dominated by thermal emission at room temperature. The contribution of second optical transition (QD state$\rightarrow$VB) is single out in figure 5.10 showing a larger contribution with stronger quadratic dependence of 2nd photon transition for the case of 400 meV.

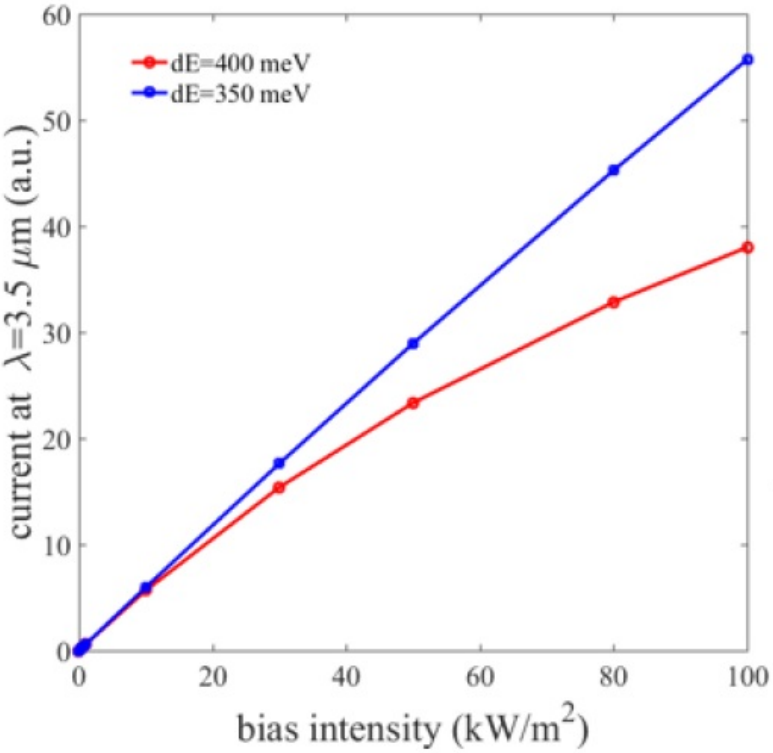


Fig. 5.9 Photocurrent at $\lambda = 3.5\mu$m as a function of intensity of the bias illumination at the first transition wavelength (CB $\rightarrow$ QD state)

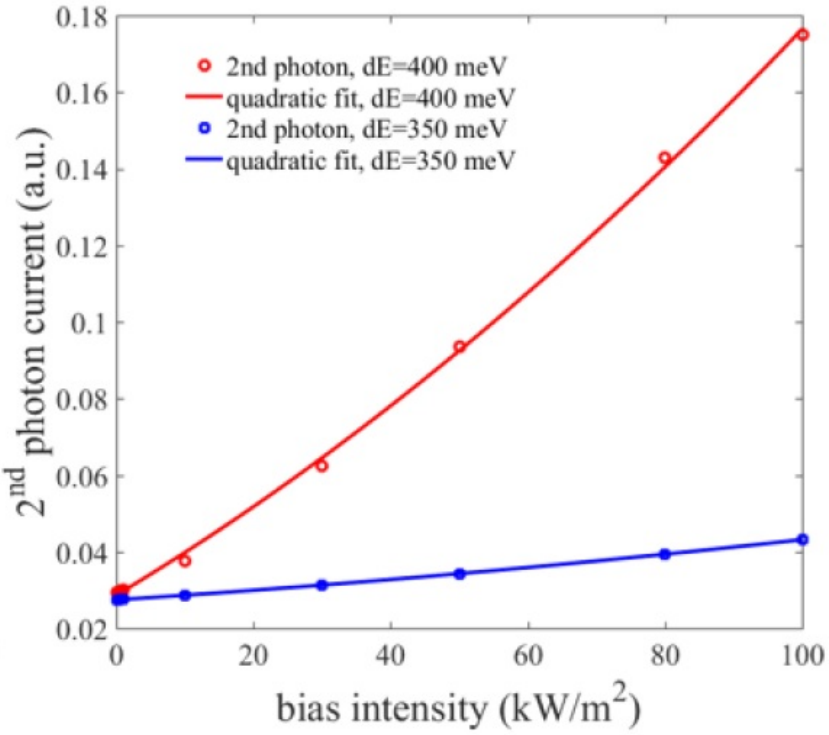


Fig. 5.10 Contribution of the 2nd photon current (QD state → VB) under bias illumination of the 1st transition wavelength

### 5.2.1 Thermal and optical escape competition in quantum dot solar cells

Figure 5.11 presents the spatial average of optical and thermal escape rates in undoped QDSC at short circuit with type-I and type-II QDs. The figure highlights the crossing point where the optical escape due to second photon transition dominates over the thermal one in type-II QDSC, while, in type-I InAs/GaAs QDs thermal escape remains the dominant process up to the maximum sun concentration. Moreover, the crossing point in type-II QDs presents a dependence on the confinement energy level (denoted by dE in the figure). The crossing point at 1000 sun concentration obtained for confinement energy level of 350 meV is in good agreement with the one reported by Hwang et al. [18].

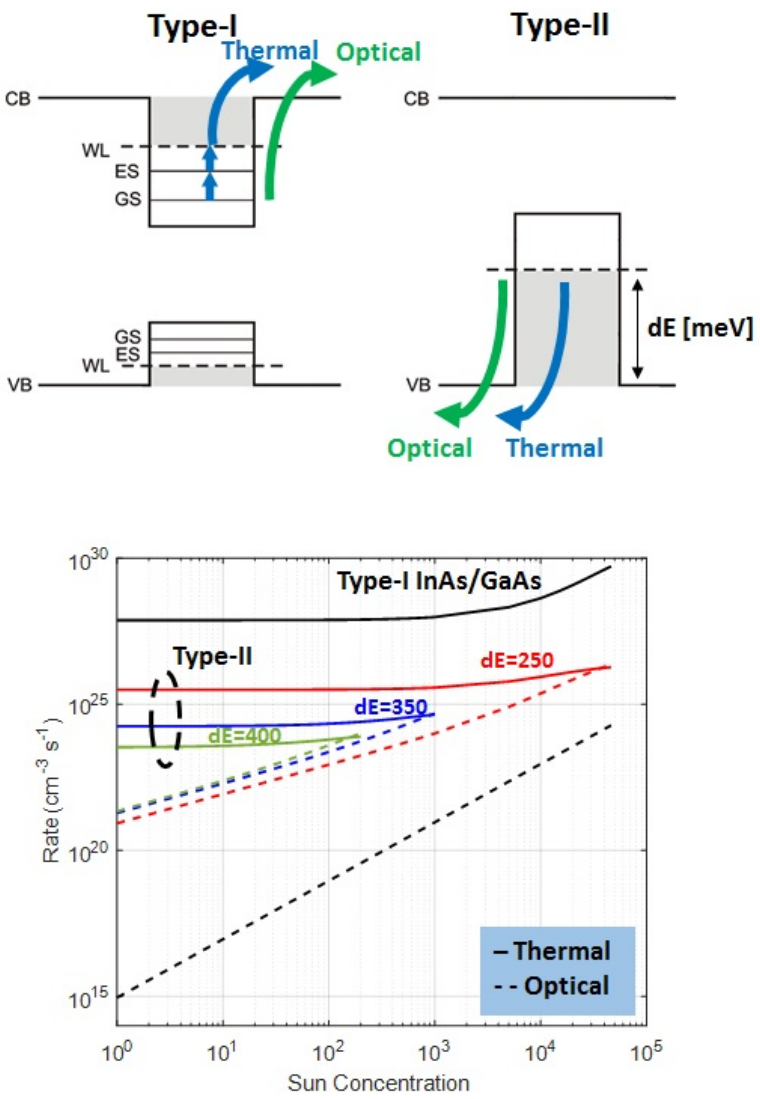


Fig. 5.11 Competition between thermal and optical escape mechanism in two case studies at short circuit for undoped QDSCs

Figures 5.12 and 5.13 illustrate the spatial distribution of the two escape mechanisms of type-II QDSCs at short circuit for two confinement level values of 350 and 400 meV, respectively, and under three different sun concentrations.

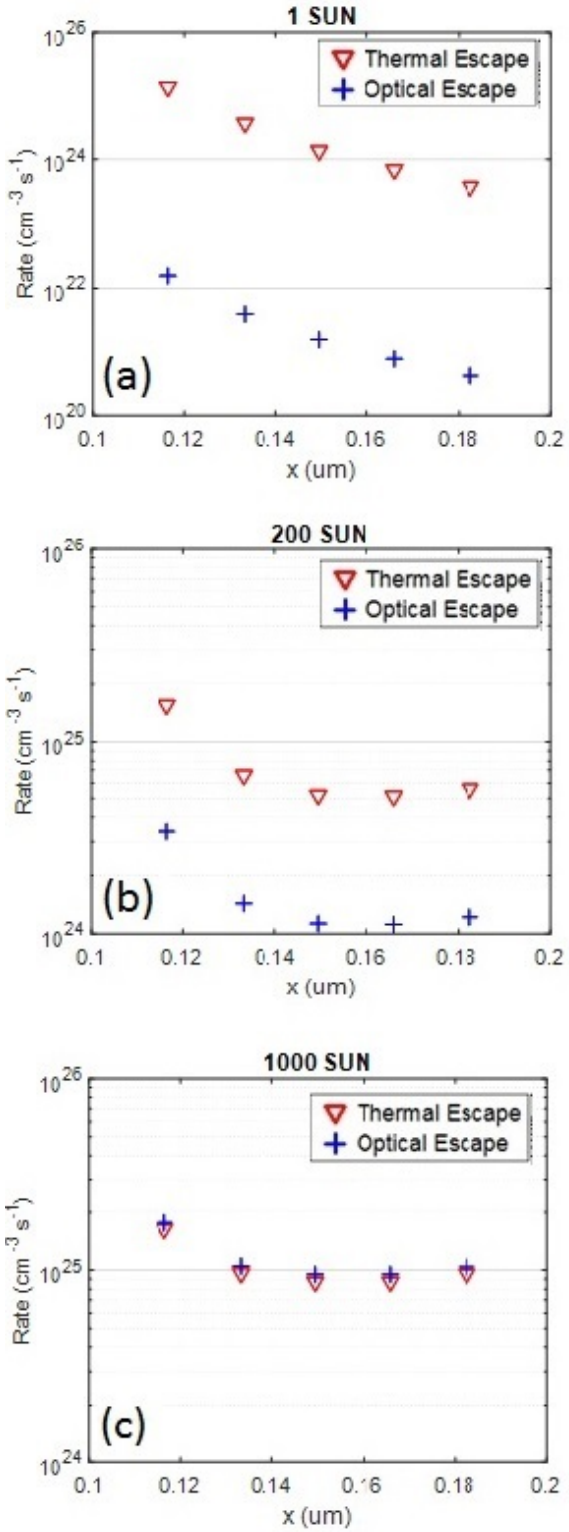


Fig. 5.12 Spatial distribution of thermal and optical escape rate for type-II GaSb/GaAs undoped QDSC with confinement energy of 350 meV at short circuit illuminated with (a) 1 Sun (b) 200 Sun and (c) 1000 Sun

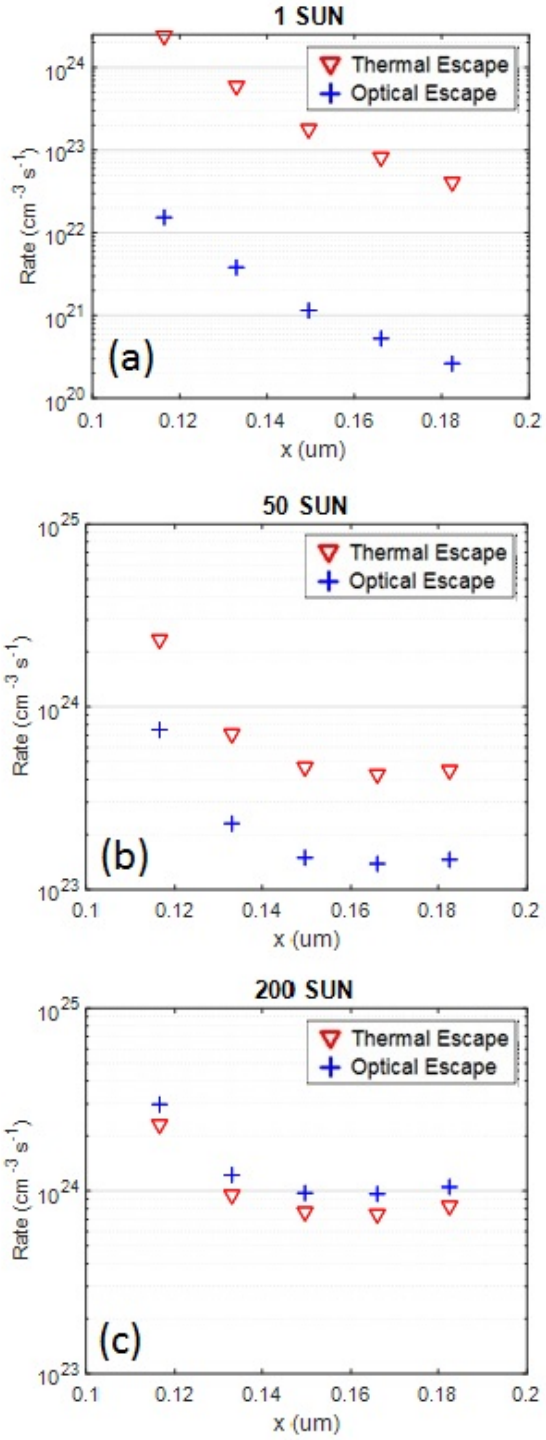


Fig. 5.13 Spatial distribution of thermal and optical escape rate for type-II GaSb/GaAs undoped QDSC with confinement energy of 400 meV at short circuit illuminated with (a) 1 Sun (b) 50 Sun and (c) 200 Sun

### 5.2.2 Light-trapping enhanced quantum dot solar cells

Light management schemes that can be implemented in thin-film solar cells is a promising way to improve effectively QD photogeneration. Since QDSCs suffer from limited light harvesting of the QDs, light-trapping technique can be exploited in order to enhance the QD absorption length [87]. In particular, periodic nanophotonic gratings can be implemented within a thin-film configuration (i.e. removing the substrate, e.g. through wafer epitaxial lift-off [88]) to achieve effective light-trapping. Figure 5.14 illustrates the propagation of a light ray in three different structures: (a) normal bulk cell without back reflector (b) thin-film with a rear planar reflector, and (c) thin-film with rear textured reflector.

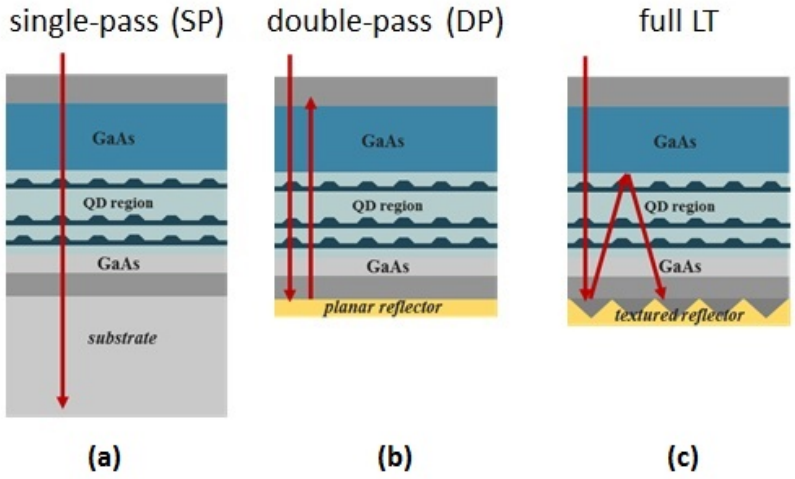


Fig. 5.14 Propagation of a light ray in three different structures: (a) normal bulk cell without back reflector (b) thin-film with a rear planar reflector, and (c) thin-film with rear textured reflector..

Light-trapping in the textured thin-film cells is modeled by assuming multiple incoherent reflections between the front and rear surfaces characterized by the reflectance $R_f$ and $R_b$, respectively. A schematic illustration of the model is shown in the figure 5.15.

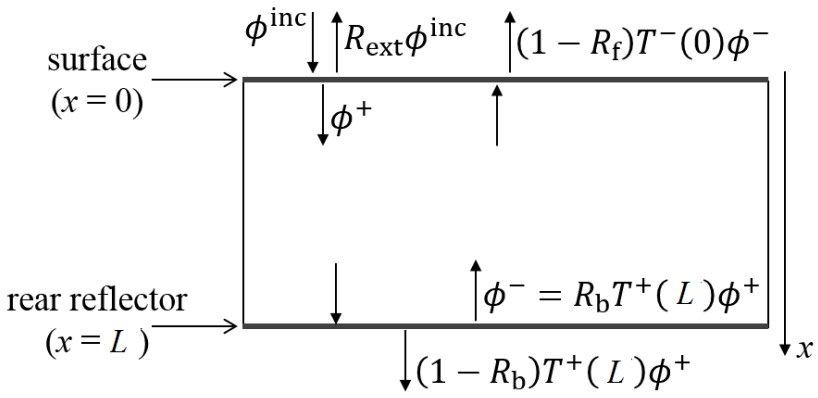


Fig. 5.15 Schematic of optical modeling of a textured thin film cell.

In the figure $R_b$, $R_f$, and $R_{ext}$ are the effective reflectance of the cell rear surface, the top internal reflectance, and the reflectance at the illuminated surface respectively. Under the assumption of Lambertian light trapping [89, 90], $R_b$ is assumed to be angular independent and the top internal reflectance $R_f$ is given as

$$R_f = 1 - \frac{1 - R_{ext}}{n^2} \tag{5.1}$$

Where $n$ is the semiconductor refractive index. The total optical energy flux (W/cm$^2$) in the cell can be written as the combination of downward and upward propagation fluxes:

$$\phi(x) = \phi^{inc}(1 - R_{ext})\frac{T^+(x) + R_bT^+(L)T^-(x)}{1 - R_bR_fT^+(L)T^-(0)} \tag{5.2}$$

Where $\phi^{inc}$ is the incident solar flux and $T^+$ and $T^-$ are the downward and upward transmittance, respectively. Assuming perpendicular propagation, $T^+ = T^- = \exp(-\alpha L)$ which yields the maximum absorbance of $2n^2$ in the weak absorption limit ($\alpha L \to 0$). Considering the oblique rays and averaging them over the angle of propagation, the well-known Lambertian limit [91] can be achieved. This limit can be derived from equation 5.3 by comparing the absorbance of a textured cell $\alpha(\lambda)$ and that of a planar cell in the weak absorption limit ($\alpha L \to 0$).

$$a(\lambda) = \frac{4n^2\alpha \mathrm{L}}{4n^2\alpha \mathrm{L} + 1} \tag{5.3}$$

Where $n$ is the refractive index, $\alpha$ is the absorption coefficient (cm$^{-1}$), and L is the optical length (cm).

In the simulation we considered normal incident and the optical power inside the cell is computed according to the equation 5.2. Figure 5.16 shows the competition between thermal and optical escape mechanisms of a doped (6h/dot) QDSC with GaSb/GaAs type-II QDs with rear planar and textured reflector (denoted in the figure by DP and LT, respectively). The figure highlights the dominance of optical escape at lower sun concentration in the structure with textured reflector.

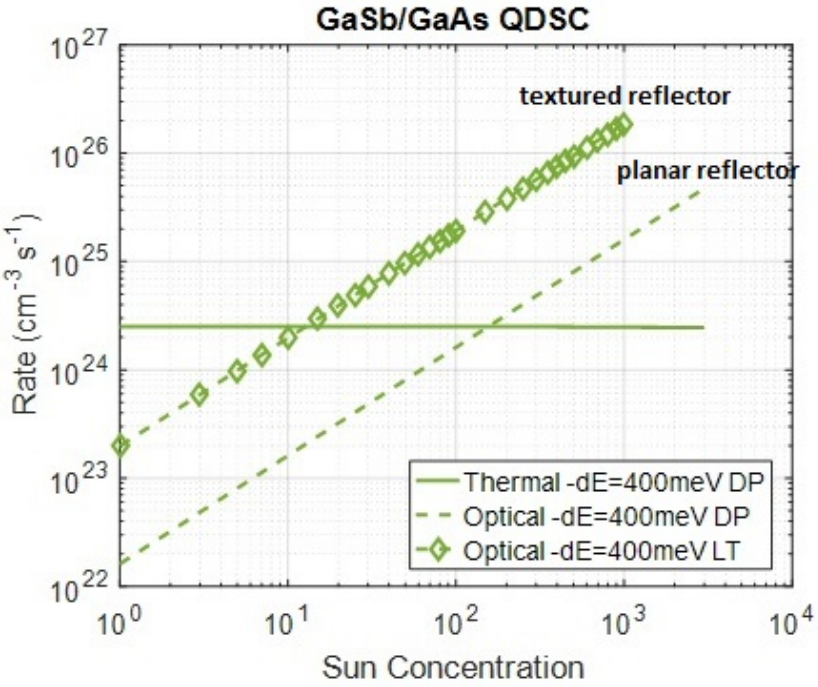


Fig. 5.16 Competition between thermal and optical escape mechanism for doped QDSCs at short circuit. The influence of light trapping is also presented

### 5.2.3 Behavior of $V_{oc}$ with respect to sun concentration

Theoretically, for a conventional solar cell the short circuit current increases linearly with respect to sun concentration while $V_{oc}$ increases logarithmically. For IBSC on the other hand, due to the consequence of IB carrier dynamics (photo-filling and second photon transition) the short circuit increases with larger rate, giving rise to a superlinear behavior of $V_{oc}$ with respect to sun concentration in logarithmic scale [12].

Simple approximated equation can be found for $V_{oc}$ by setting the net current equal

to zero in solar cell equation.

$$V_{oc} \approx n\, V_T\ \log(J_{sc}) \tag{5.4}$$

Since the short circuit current is linearly proportional to sun concentration, this relation can be rewritten as

$$V_{oc} \approx n\, V_T\ \log(X_{sun}) \tag{5.5}$$

Figure 5.17 highlights the superlinear behavior of $V_{oc}$ in type-II QDSC, while the ideality factor of 1 in type-I QDSC is an the indication of thermally limited behavior.

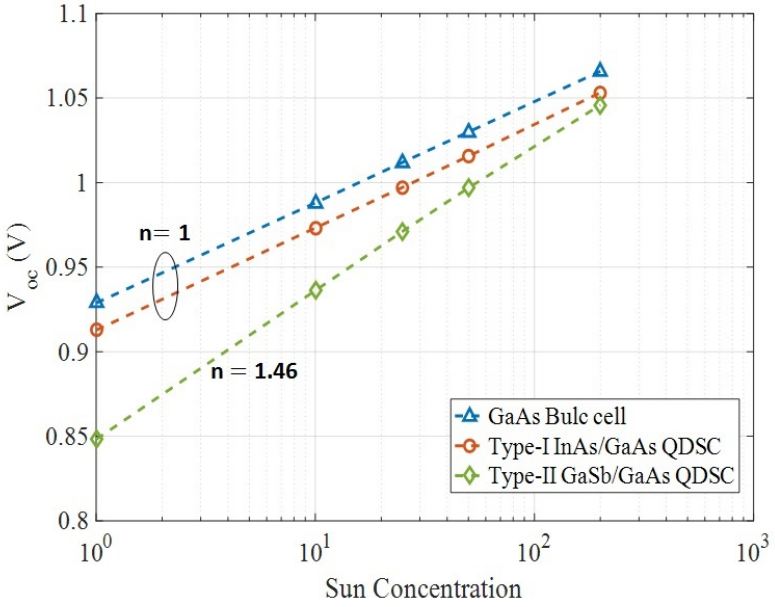


Fig. 5.17 Evolution of open circuit voltage with respect to sun concentration for conventional bulk cell, undoped type-I InAs/GaAs QDSC and undoped type-II GaSb/GaAs with confinement energy of 400 meV.

Although $V_{oc}$ is smaller in type-II QDSC, it increases with larger rate compared to the type-I. The superlinear behavior of $V_{oc}$ is due to the fact that at higher concentration larger voltage is required in order to compensate for the larger net carrier generation via IB [12].

In conclusion, going from thermally limited regime to optically dominated regime requires more confined energy states in quantum dot solar cells. GaSb/GaAs quantum

dot system is more promising in view of attaining the IB operating regime thanks to the larger energy confinement and also providing longer radiative recombination lifetime. Furthermore, the large confinement in VB makes this device more suitable for operating at higher temperature.

# References


[1] Weng W Chow and Frank Jahnke. On the physics of semiconductor quantum dots for applications in lasers and quantum optics. *Progress in Quantum Electronics*, 37(3):109–184, 2013.

[2] R Dingle and CH Henry. Quantum effects in heterostructure lasers. Technical report, 1976.

[3] DJ Eaglesham and M Cerullo. Dislocation-free stranski-krastanow growth of ge on si (100). *Physical review letters*, 64(16):1943, 1990.

[4] Nobuyuki Koguchi, Satoshi Takahashi, and Toyohiro Chikyow. New mbe growth method for insb quantum well boxes. *Journal of crystal growth*, 111 (1-4):688–692, 1991.

[5] D Leonard, M Krishnamurthy, CMv Reaves, Steven P DenBaars, and Pierre M Petroff. Direct formation of quantum-sized dots from uniform coherent islands of ingaas on gaas surfaces. *Applied Physics Letters*, 63(23):3203–3205, 1993.

[6] Mashiro Asada, Yasuyuki Miyamoto, and Yasuharu Suematsu. Gain and the threshold of three-dimensional quantum-box lasers. *IEEE Journal of quantum electronics*, 22(9):1915–1921, 1986.

[7] Jiang Wu, Siming Chen, Alwyn Seeds, and Huiyun Liu. Quantum dot optoelectronic devices: lasers, photodetectors and solar cells. *Journal of Physics D: Applied Physics*, 48(36):363001, 2015.

[8] Shiang-Feng Tang, Hui-Huang Hsieh, Hsing-Yuan Tu, Teng-Hua You, Shih-Yen Lin, Li-Chun Wang, and Cheng-Der Chiang. Investigations for inas/gaas multilayered quantum-dot structure treated by high energy proton irradiation. *Thin Solid Films*, 518(24):7425–7428, 2010.

[9] Victor Ryzhii. The theory of quantum-dot infrared phototransistors. *Semiconductor science and technology*, 11(5):759, 1996.

[10] Jong-Wook Kim, Jae-Eung Oh, Seong-Chul Hong, Chung-Hoon Park, and Tae-Kyung Yoo. Room temperature far infrared (8/spl sim/10 $\mu$m) photodetectors using self-assembled inas quantum dots with high detectivity. *IEEE Electron Device Letters*, 21(7):329–331, 2000.

[11] Antonio Luque and Antonio Martí. Increasing the efficiency of ideal solar cells by photon induced transitions at intermediate levels. *Physical Review Letters*, 78(26):5014, 1997.

[12] Tomah Sogabe, Yasushi Shoji, Mitsuyoshi Ohba, Katsuhisa Yoshida, Ryo Tamaki, Hwen-Fen Hong, Chih-Hung Wu, Cherng-Tsong Kuo, Stanko Tomić, and Yoshitaka Okada. Intermediate-band dynamics of quantum dots solar cell in concentrator photovoltaic modules. *Scientific reports*, 4:4792, 2014.

[13] Christopher G Bailey, David V Forbes, Stephen J Polly, Zachary S Bittner, Yushuai Dai, Chelsea Mackos, Ryne P Raffaelle, and Seth M Hubbard. Open-circuit voltage improvement of inas/gaas quantum-dot solar cells using reduced inas coverage. *IEEE Journal of Photovoltaics*, 2(3):269–275, 2012.

[14] Christopher G Bailey, David V Forbes, Ryne P Raffaelle, and Seth M Hubbard. Near 1 v open circuit voltage inas/gaas quantum dot solar cells. *Applied Physics Letters*, 98(16):163105, 2011.

[15] Kimberly A Sablon, John W Little, Vladimir Mitin, Andrei Sergeev, Nizami Vagidov, and Kitt Reinhardt. Strong enhancement of solar cell efficiency due to quantum dots with built-in charge. *Nano letters*, 11(6):2311–2317, 2011.

[16] A Martí, N López, E Antolin, E Cánovas, C Stanley, Cuadra Farmer, L Cuadra, and A Luque. Novel semiconductor solar cell structures: The quantum dot intermediate band solar cell. *Thin Solid Films*, 511:638–644, 2006.

[17] Yoshitaka Okada, Takayuki Morioka, Katsuhisa Yoshida, Ryuji Oshima, Yasushi Shoji, Tomoya Inoue, and Takashi Kita. Increase in photocurrent by optical transitions via intermediate quantum states in direct-doped inas/ganas strain-compensated quantum dot solar cell. *Journal of Applied Physics*, 109(2): 024301, 2011.

[18] Jinyoung Hwang, Andrew J Martin, Joanna M Millunchick, and Jamie D Phillips. Thermal emission in type-ii gasb/gaas quantum dots and prospects for intermediate band solar energy conversion. *Journal of Applied Physics*, 111(7): 074514, 2012.

[19] Martin Wolf. Limitations and possibilities for improvement of photovoltaic solar energy converters: Part i: Considerations for earth's surface operation. *Proceedings of the IRE*, 48(7):1246–1263, 1960.

[20] MJ Keevers and MA Green. Efficiency improvements of silicon solar cells by the impurity photovoltaic effect. *Journal of Applied Physics*, 75(8):4022–4031, 1994.

[21] Antonio Luque, Antonio Martí, Elisa Antolín, and César Tablero. Intermediate bands versus levels in non-radiative recombination. *Physica B: Condensed Matter*, 382(1-2):320–327, 2006.

[22] William Shockley and Hans J Queisser. Detailed balance limit of efficiency of p-n junction solar cells. *Journal of applied physics*, 32(3):510–519, 1961.

[23] Martin A Green, Keith Emery, Yoshihiro Hishikawa, Wilhelm Warta, and Ewan D Dunlop. Solar cell efficiency tables (version 45). *Progress in photovoltaics: research and applications*, 23(1):1–9, 2015.

[24] Y Okada, NJ Ekins-Daukes, T Kita, R Tamaki, M Yoshida, A Pusch, O Hess, CC Phillips, DJ Farrell, K Yoshida, et al. Intermediate band solar cells: Recent progress and future directions. *Applied physics reviews*, 2(2):021302, 2015.

[25] Katsuhisa Yoshida, Yoshitaka Okada, and Nobuyuki Sano. Device simulation of intermediate band solar cells: Effects of doping and concentration. *Journal of applied physics*, 112(8):084510, 2012.

[26] W Van Roosbroeck and W Shockley. Photon-radiative recombination of electrons and holes in germanium. *Physical Review*, 94(6):1558, 1954.

[27] Michael Y Levy and Christiana Honsberg. Solar cell with an intermediate band of finite width. *Physical Review B*, 78(16):165122, 2008.

[28] Lucas Cuadra, Antonio Martí, and Antonio Luque. Influence of the overlap between the absorption coefficients on the efficiency of the intermediate band solar cell. *IEEE Transactions on Electron Devices*, 51(6):1002–1007, 2004.

[29] Rune Strandberg and Turid Worren Reenaas. Drift-diffusion model for intermediate band solar cells including photofilling effects. *Progress in Photovoltaics: Research and Applications*, 19(1):21–32, 2011.

[30] I Tobías, Antonio Luque, and Antonio Martí. Numerical modeling of intermediate band solar cells. *Semiconductor Science and Technology*, 26(1):014031, 2010.

[31] Katsuhisa Yoshida, Yoshitaka Okada, and Nobuyuki Sano. Self-consistent simulation of intermediate band solar cells: Effect of occupation rates on device characteristics. *Applied physics letters*, 97(13):133503, 2010.

[32] Albert S Lin and Jamie D Phillips. Drift-diffusion modeling for impurity photovoltaic devices. *IEEE Transactions on Electron Devices*, 56(12):3168–3174, 2009.

[33] Antonio Martí, Lucas Cuadra, and Antonio Luque. Quasi-drift diffusion model for the quantum dot intermediate band solar cell. *IEEE Transactions on Electron Devices*, 49(9):1632–1639, 2002.

[34] Rune Strandberg and Turid Worren Reenaas. Photofilling of intermediate bands. *Journal of Applied Physics*, 105(12):124512, 2009.

[35] Mariangela Gioannini, Ariel P Cedola, Natale Di Santo, Francesco Bertazzi, and Federica Cappelluti. Simulation of quantum dot solar cells including carrier intersubband dynamics and transport. *IEEE Journal of Photovoltaics*, 3(4): 1271–1278, 2013.

[36] Seth M Hubbard, Adam Podell, Chelsea Mackos, Stephen Polly, Christopher G Bailey, and David V Forbes. Effect of vicinal substrates on the growth and device performance of quantum dot solar cells. *Solar Energy Materials and Solar Cells*, 108:256–262, 2013.

[37] Antonio Marti Vega, Elisa Antolín, Pablo G Linares, Iñigo Ramiro, Irene Artacho, Esther López, Estela Hernández, Manuel J Mendes, Alexander V Mellor, Ignacio Tobías, et al. Six not-so-easy pieces in intermediate band solar cell research. *Journal of Photonics for Energy*, 3(1):031299, 2013.

[38] Greg Jolley, Lan Fu, Hao Feng Lu, Hark Hoe Tan, and Chennupati Jagadish. The role of intersubband optical transitions on the electrical properties of ingaas/gaas quantum dot solar cells. *Progress in Photovoltaics: Research and Applications*, 21(4):736–746, 2013.

[39] Nir Tessler and G Eistenstein. On carrier injection and gain dynamics in quantum well lasers. *IEEE journal of quantum electronics*, 29(6):1586–1595, 1993.

[40] Francesco Bertazzi, Federica Cappelluti, S Donati Guerrieri, Fabrizio Bonani, and Giovanni Ghione. Self-consistent coupled carrier transport full-wave em analysis of semiconductor traveling-wave devices. *IEEE transactions on microwave theory and techniques*, 54(4):1611–1618, 2006.

[41] KA Bertness, Sarah R Kurtz, D17 J Friedman, AE Kibbler, C Kramer, and JM Olson. 29.5%-efficient gainp/gaas tandem solar cells. *Applied Physics Letters*, 65(8):989–991, 1994.

[42] Thomas Müller, FF Schrey, Gottfried Strasser, and Karl Unterrainer. Ultrafast intraband spectroscopy of electron capture and relaxation in inas/gaas quantum dots. *Applied physics letters*, 83(17):3572–3574, 2003.

[43] Mariangela Gioannini and Mattia Rossetti. Time-domain traveling wave model of quantum dot dfb lasers. *IEEE Journal of Selected Topics in Quantum Electronics*, 17(5):1318–1326, 2011.

[44] D. M. Caughey and R. E. Thomas. Carrier mobilities in silicon empirically related to doping and field. *Proceedings of the IEEE*, 55(12):2192–2193, 1967.

[45] We Shockley and WT Read Jr. Statistics of the recombinations of holes and electrons. *Physical review*, 87(5):835, 1952.

[46] Federica Cappelluti, Mariangela Gioannini, and Arastoo Khalili. Impact of doping on inas/gaas quantum-dot solar cells: a numerical study on photovoltaic and photoluminescence behavior. *Solar Energy Materials and Solar Cells*, 157: 209–220, 2016.

[47] Fedeirca Cappelluti, Arastoo Khalili, and Mariangela Gioannini. Selective doping in inas/gaas quantum dot solar cells: Effect on photoluminescence and photovoltaic performance. In *Compound Semiconductor Week (CSW)[Includes 28th International Conference on Indium Phosphide & Related Materials (IPRM) & 43rd International Symposium on Compound Semiconductors (ISCS), 2016*, pages 1–1. IEEE, 2016.

[48] Federica Cappelluti, Mariangela Gioannini, Giovanni Ghione, and Arastoo Khalili. Numerical study of thin-film quantum-dot solar cells combining selective doping and light-trapping approaches. In *Photovoltaic Specialists Conference (PVSC), 2016 IEEE 43rd*, pages 1282–1286. IEEE, 2016.

[49] Stephen J Polly, David V Forbes, Kristina Driscoll, Staffan Hellström, and Seth M Hubbard. Delta-doping effects on quantum-dot solar cells. *IEEE Journal of Photovoltaics*, 4(4):1079–1085, 2014.

[50] Phu Lam, Sabina Hatch, Jiang Wu, Mingchu Tang, Vitaliy G Dorogan, Yuriy I Mazur, Gregory J Salamo, Iñigo Ramiro, Alwyn Seeds, and Huiyun Liu. Voltage recovery in charged inas/gaas quantum dot solar cells. *Nano Energy*, 6: 159–166, 2014.

[51] Takayuki Morioka and Yoshitaka Okada. Dark current characteristics of inas/ganas strain-compensated quantum dot solar cells. *Physica E: Low-Dimensional Systems and Nanostructures*, 44(2):390–393, 2011.

[52] Takashi Kita, Ryuichi Hasagawa, and Tomoya Inoue. Suppression of non-radiative recombination process in directly si-doped inas/gaas quantum dots. *Journal of Applied Physics*, 110(10):103511, 2011.

[53] Xiaoguang Yang, Kefan Wang, Yongxian Gu, Haiqiao Ni, Xiaodong Wang, Tao Yang, and Zhanguo Wang. Improved efficiency of inas/gaas quantum dots solar cells by si-doping. *Solar Energy Materials and Solar Cells*, 113:144–147, 2013.

[54] Peter S Zory. *Quantum Well Lasers*. Academic Press, 1993.

[55] Torben Roland Nielsen, Paul Gartner, and Frank Jahnke. Many-body theory of carrier capture and relaxation in semiconductor quantum-dot lasers. *Physical Review B*, 69(23):235314, 2004.

[56] Gustavo A Narvaez, Gabriel Bester, and Alex Zunger. Carrier relaxation mechanisms in self-assembled (in, ga) as/ ga as quantum dots: Efficient p? s auger relaxation of electrons. *Physical Review B*, 74(7):075403, 2006.

[57] K Schuh, P Gartner, and F Jahnke. Combined influence of carrier-phonon and coulomb scattering on the quantum-dot population dynamics. *Physical Review B*, 87(3):035301, 2013.

[58] Stanko Tomić. Intermediate-band solar cells: Influence of band formation on dynamical processes in inas/gaas quantum dot arrays. *Physical Review B*, 82 (19):195321, 2010.

[59] Jörg Siegert, Saulius Marcinkevičius, and Qing Xiang Zhao. Carrier dynamics in modulation-doped in as/ ga as quantum dots. *Physical Review B*, 72(8): 085316, 2005.

[60] Mariangela Gioannini, Ariel P Cedola, and Federica Cappelluti. Impact of carrier dynamics on the photovoltaic performance of quantum dot solar cells. *IET Optoelectronics*, 9(2):69–74, 2015.

[61] Harold J Hovel. Semiconductors and semimetals. volume 11. solar cells. 1975.

[62] Peter Würfel, Uli Würfel, Albert Overhauser, Gene Dresselhaus, Lamberto Duo, Marco Finazzi, Franco Ciccacci, Andriy M Gusak, TV Zaporozhets, Yu O Lyashenko, et al. Physics of solar cells: From basic principles to advanced concepts.

[63] VV Mitin, VI Pipa, AV Sergeev, M Dutta, and M Stroscio. High-gain quantum-dot infrared photodetector. *Infrared physics & technology*, 42(3):467–472, 2001.

[64] YD Jang, J Park, D Lee, DJ Mowbray, MS Skolnick, HY Liu, M Hopkinson, and RA Hogg. Enhanced room-temperature quantum-dot effects in modulation-doped inas/gaas quantum dots. *Applied Physics Letters*, 95(17):171902, 2009.

[65] EC Le Ru, J Fack, and R Murray. Temperature and excitation density dependence of the photoluminescence from annealed inas/gaas quantum dots. *Physical Review B*, 67(24):245318, 2003.

[66] S Sanguinetti, D Colombo, M Guzzi, E Grilli, M Gurioli, L Seravalli, P Frigeri, and S Franchi. Carrier thermodynamics in inas/ in x ga 1- x as quantum dots. *Physical Review B*, 74(20):205302, 2006.

[67] AP Cédola, D Kim, A Tibaldi, M Tang, A Khalili, J Wu, H Liu, and F Cappelluti. Physics-based modeling and experimental study of si-doped inas/gaas quantum dot solar cells.

[68] A Varghese, M Yakimov, V Tokranov, V Mitin, K Sablon, A Sergeev, and S Oktyabrsky. Complete voltage recovery in quantum dot solar cells due to suppression of electron capture. *Nanoscale*, 8(13):7248–7256, 2016.

[69] KA Sablon, A Sergeev, JW Little, N Vagidov, and V Mitin. Nanoscale optimization of quantum dot media for effective photovoltaic conversion. In *SPIE Defense+ Security*, pages 908313–908313. International Society for Optics and Photonics, 2014.

[70] FK Tutu, P Lam, J Wu, N Miyashita, Y Okada, K-H Lee, NJ Ekins-Daukes, J Wilson, and H Liu. Inas/gaas quantum dot solar cell with an alas cap layer. *Applied Physics Letters*, 102(16):163907, 2013.

[71] Nextnano. http://www.nextnano.de/index.php.

[72] Seungwon Lee, Olga L Lazarenkova, Paul von Allmen, Fabiano Oyafuso, and Gerhard Klimeck. Effect of wetting layers on the strain and electronic structure of inas self-assembled quantum dots. *Physical Review B*, 70(12):125307, 2004.

[73] Dongyoung Kim, Mingchu Tang, Jiang Wu, Sabina Hatch, Yurii Maidaniuk, Vitaliy Dorogan, Yuriy I Mazur, Gregory J Salamo, and Huiyun Liu. Si-doped inas/gaas quantum-dot solar cell with alas cap layers. *IEEE Journal of Photovoltaics*, 6(4):906–911, 2016.

[74] Antonio Luque, Antonio Martí, and Lucas Cuadra. Thermodynamic consistency of sub-bandgap absorbing solar cell proposals. *IEEE Transactions on Electron Devices*, 48(9):2118–2124, 2001.

[75] Kimberly A Sablon, Andrei Sergeev, Nizami Vagidov, John W Little, and Vladimir Mitin. Effects of quantum dot charging on photoelectron processes and solar cell characteristics. *Solar Energy Materials and Solar Cells*, 117: 638–644, 2013.

[76] Andres Cuevas. The recombination parameter j0. *Energy Procedia*, 55:53–62, 2014.

[77] V Ryzhii, I Khmyrova, V Pipa, V Mitin, and M Willander. Device model for quantum dot infrared photodetectors and their dark-current characteristics. *Semiconductor science and technology*, 16(5):331, 2001.

[78] Kimberly Sablon, Andrei Sergeev, Nizami Vagidov, Andrei Antipov, John Little, and Vladimir Mitin. Effective harvesting, detection, and conversion of ir radiation due to quantum dots with built-in charge. *Nanoscale research letters*, 6(1):584, 2011.

[79] F Hatami, NN Ledentsov, M Grundmann, J Böhrer, F Heinrichsdorff, M Beer, D Bimberg, SS Ruvimov, P Werner, U Gösele, et al. Radiative recombination in type-ii gasb/gaas quantum dots. *Applied physics letters*, 67(5):656–658, 1995.

[80] K Suzuki, RA Hogg, and Y Arakawa. Structural and optical properties of type ii gasb/gaas self-assembled quantum dots grown by molecular beam epitaxy. *Journal of applied physics*, 85(12):8349–8352, 1999.

[81] L Müller-Kirsch, R Heitz, A Schliwa, O Stier, D Bimberg, H Kirmse, and W Neumann. Many-particle effects in type ii quantum dots. *Applied Physics Letters*, 78(10):1418–1420, 2001.

[82] Baolai Liang, Andrew Lin, Nicola Pavarelli, Charles Reyner, Jun Tatebayashi, Kalyan Nunna, Jun He, Tomasz J Ochalski, Guillaume Huyet, and Diana L Huffaker. Gasb/gaas type-ii quantum dots grown by droplet epitaxy. *Nanotechnology*, 20(45):455604, 2009.

[83] C-K Sun, G Wang, JE Bowers, B Brar, H-R Blank, H Kroemer, and MH Pilkuhn. Optical investigations of the dynamic behavior of gasb/gaas quantum dots. *Applied physics letters*, 68(11):1543–1545, 1996.

[84] K Komolibus, T Piwonski, CJ Reyner, B Liang, G Huyet, DL Huffaker, EA Viktorov, and J Houlihan. Absorption dynamics of type-ii gasb/gaas quantum dots. *Optical Materials Express*, 7(4):1424–1430, 2017.

[85] Antonio Luque, Antonio Martí, N López, E Antolin, E Canovas, C Stanley, C Farmer, and P Diaz. Operation of the intermediate band solar cell under nonideal space charge region conditions and half filling of the intermediate band. *Journal of Applied Physics*, 99(9):094503, 2006.

[86] MC Wagener, PJ Carrington, JR Botha, and A Krier. Evaluation of the two-photon absorption characteristics of gasb/gaas quantum rings. *Journal of Applied Physics*, 116(4):044304, 2014.

[87] A Mellor, A Luque, I Tobías, and A Martí. The feasibility of high-efficiency inas/gaas quantum dot intermediate band solar cells. *Solar Energy Materials and Solar Cells*, 130:225–233, 2014.

[88] Tomah Sogabe, Yasushi Shoji, Peter Mulder, John Schermer, Efrain Tamayo, and Yoshitaka Okada. Enhancement of current collection in epitaxial lift-off inas/gaas quantum dot thin film solar cell and concentrated photovoltaic study. *Applied Physics Letters*, 105(11):113904, 2014.

[89] James M Gee. The effect of parasitic absorption losses on light trapping in thin silicon solar cells. In *Photovoltaic Specialists Conference, 1988., Conference Record of the Twentieth IEEE*, pages 549–554. IEEE, 1988.

[90] Martin A Green. Lambertian light trapping in textured solar cells and light-emitting diodes: analytical solutions. *progress in Photovoltaics: Research and Applications*, 10(4):235–241, 2002.

[91] Eli Yablonovitch and George D Cody. Intensity enhancement in textured optical sheets for solar cells. *IEEE Transactions on Electron Devices*, 29(2):300–305, 1982.